

UNIVERSITY OF CALIFORNIA, SAN DIEGO

**The Role of Regulatory Light Chain Phosphorylation in Left
Ventricular Function**

A dissertation submitted in partial satisfaction of the
requirements for the degree
Doctor of Philosophy

in

Bioengineering

by

Stuart Gaylon Campbell

Committee in charge:

Professor Andrew D. McCulloch, Chair
Professor Jeffrey H. Omens, Co-Chair
Professor Ju Chen
Professor Richard L. Lieber
Professor Maryann Martone

2010

UMI Number: 3398511

All rights reserved

INFORMATION TO ALL USERS

The quality of this reproduction is dependent upon the quality of the copy submitted.

In the unlikely event that the author did not send a complete manuscript and there are missing pages, these will be noted. Also, if material had to be removed, a note will indicate the deletion.



UMI 3398511

Copyright 2010 by ProQuest LLC.

All rights reserved. This edition of the work is protected against unauthorized copying under Title 17, United States Code.



ProQuest LLC
789 East Eisenhower Parkway
P.O. Box 1346
Ann Arbor, MI 48106-1346

Copyright
Stuart Gaylon Campbell, 2010
All rights reserved.

The dissertation of Stuart Gaylon Campbell is approved,
and it is acceptable in quality and form for publication
on microfilm and electronically:

Co-Chair

Chair

University of California, San Diego

2010

DEDICATION

To my wife, Adrienne,
and our children, Hannah, Grant, and Claire.

EPIGRAPH

*You can't reason with your heart;
it has its own laws, and thumps about things
which the intellect scorns.*

—Mark Twain

TABLE OF CONTENTS

Signature Page		iii
Dedication		iv
Epigraph		v
Table of Contents		vi
List of Figures		xi
List of Tables		xiii
Acknowledgements		xv
Vita and Publications		xvii
Abstract of the Dissertation		xviii
Chapter 1	Introduction	1
	1.1 Cardiac Excitation-Contraction Coupling	1
	1.2 Heterogeneous distribution of EC-coupling properties in the heart	2
	1.3 Ca^{2+} buffering and cooperativity in cardiac myofilaments	3
	1.4 Summary	5
Chapter 2	Mechanisms of transmurally-varying myocyte electromechanics in an integrated computational model	9
	2.1 Introduction	10
	2.1.1 Transmural heterogeneity	10
	2.1.2 Models of myocyte electromechanics	12
	2.2 Methods	15
	2.2.1 Model of myocyte electromechanics	15
	2.2.2 Modification of published model parameters	15
	2.2.3 Modelling of the exogenous Ca^{2+} buffer fluo-3	16
	2.2.4 Simulation of shortening under clamped $[\text{Ca}^{2+}]$ and Ca^{2+} -flux conditions	17
	2.3 Results	18
	2.3.1 Model Validation	18
	2.3.2 Modelled transmural heterogeneity of myocyte elec- tromechanics	18
	2.3.3 AP-clamp simulations	20

	2.3.4	Influence of an exogenous buffer on Ca^{2+} transients and unloaded shortening	22
	2.3.5	Flux-clamp validation	24
	2.3.6	Shortening responses to realistic Ca^{2+} -transients .	24
	2.3.7	Testing hypothesized myofilament heterogeneities	27
2.4	Discussion	28
	2.4.1	Modulation of contractile dynamics by early repolarisation and I_{to1}	28
	2.4.2	Transmural heterogeneity of myofilament protein expression	30
	2.4.3	Insights from tight coupling between EP and myofilament models	31
	2.4.4	Limitations	32
	2.4.5	Conclusion	33
Chapter 3	A Model of Heterogeneous Ventricular Electromechanics	. . .	40
	3.1	Introduction	41
	3.1.1	Models of Ventricular Electromechanics	42
	3.2	Methods	43
	3.2.1	Model of myocyte excitation-contraction coupling	43
	3.2.2	Coupling of velocity-dependent contraction and finite-element biomechanics models	44
	3.2.3	Finite Element model of myocardial deformation .	45
	3.2.4	Finite Element model of electrical propagation . .	46
	3.2.5	Representation of heterogeneous cellular properties	47
	3.2.6	Lumped-parameter circulatory model	47
	3.2.7	Simulation protocol	48
	3.2.8	Experimentally-measured fibre strains	48
	3.3	Results	49
	3.3.1	Hemodynamics and electrical activation	50
	3.3.2	Transmural gradients of end-systolic strains . . .	51
	3.3.3	Time course of fibre strain during systole	52
	3.3.4	Sensitivity Analysis	52
	3.4	Discussion	55
	3.4.1	Transmural gradients of end-systolic fibre strains .	57
	3.4.2	Effects of cellular heterogeneity on the time course of systolic fibre strains	57
	3.4.3	Comparison with previous work	58
	3.4.4	Limitations and future work	59
	3.4.5	Conclusions	60

Chapter 4	A Markov Model of Cardiac Myofilament Activation	66
4.1	Introduction	67
4.2	Model Development	68
4.2.1	Assumptions of the Model	69
4.2.2	Representation of nearest-neighbor thin filament interactions	70
4.2.3	Selection of model parameters	73
4.2.4	Simulations of coupled thin filament regulatory units	73
4.2.5	Additional Methods	74
4.3	Results	76
4.3.1	Tm-Tm coupling alters Ca^{2+} binding properties of the thin filaments	76
4.3.2	Distinct roles of nearest-neighbor interactions in myofilament activation	76
4.3.3	Effects of NEM-S1 on force-pCa and k_{tr} -pCa relations	80
4.3.4	Effects of non-functional TnC on force-pCa relations and k_{tr}	80
4.3.5	Cooperative inhibition allows substantial Ca^{2+} binding to troponin C without activating force	82
4.3.6	XBs indirectly increase thin filament Ca^{2+} affinity	82
4.3.7	Thin filament cooperativity can account for effects of inorganic phosphate	84
4.3.8	Tm-Tm interactions potentiate the activating effects of XBs	84
4.3.9	Model responses to time-varying Ca^{2+} input	84
4.3.10	Tm-Tm coupling and XB-binding synergistically enhance systolic and diastolic twitch function	86
4.4	Discussion	86
4.4.1	Model limitations and additional forms of cooperativity	90
Chapter 5	Regulatory Light Chain Phosphorylation in the Intact Myocardium	95
5.1	Introduction	95
5.2	Methods	97
5.2.1	Generation of gene-targeted mouse lines	97
5.2.2	Measurement of Ca^{2+} -contraction dynamics in RV papillary muscles	97
5.2.3	Solutions	99
5.2.4	Markov model of myofilament force production	99
5.2.5	Model representation of RLC phosphorylation	100

	5.2.6	MRI protocol and methods	102
	5.2.7	Torsion Analysis	102
	5.2.8	Multi-scale model of left ventricular mechanics . .	102
5.3	Results		105
	5.3.1	Characterization of SM and DM mice	105
	5.3.2	Model-based hypothesis of RLC Phosphorylation effects on the myofilaments	107
	5.3.3	Ca ²⁺ -contraction dynamics at 25°C	110
	5.3.4	Ca ²⁺ -contraction dynamics at 37°C	112
	5.3.5	Mechanisms underlying altered Ca ²⁺ -contraction coupling in DM mice	112
	5.3.6	Measurements and modeled effects of RLC phosphorylation on ventricular torsion . . .	115
5.4	Discussion		119
	5.4.1	RLC phosphorylation appears to affect both disposition and kinetics of myosin	120
	5.4.2	RLC phosphorylation directly affects ventricular wall motion	121
	5.4.3	Limitations and future work	122
	5.4.4	Conclusions	122
Chapter 6	Conclusions		127
	6.1	Heterogeneous electromechanical properties affect patterns of transmural strain	127
	6.2	Left ventricular torsion defects precede myocardial remodeling in non-phosphorylatable MLC2v mice	128
	6.3	Defects in torsion and twitch dynamics are mechanistically linked to MLC2v mutations	129
Appendix A	Additional Details Relating to the Cellular Electromechanics Model		131
	A.1	Coupling of EP/Ca ²⁺ -handling and myofilament models .	131
	A.2	Representing Ca ²⁺ buffering by fluo-3	132
	A.3	Flux-clamp simulation protocol	133
	A.4	Model-based testing of hypothesized epicardial cell myofilament alterations	134
Appendix B	Additional Details Relating to the Ventricular Electromechanics Model		137
Appendix C	Detailed Markov Myofilament Model Development and Additional Results		141
	C.1	Introduction	141

C.2	Model of quasi-explicit (QE) near-neighbor interactions	141
C.2.1	TF state generation	142
C.2.2	QE model equations	143
C.2.3	Combining individual RU and TF models	144
C.2.4	Calculation of aggregate Tm state occupancy from the TF model	145
C.2.5	Assembly of the TF model coefficient matrix	145
C.2.6	Equations describing coupled individual RU and TF models	146
C.2.7	Computation of initial conditions and steady-state model solutions	146
C.2.8	Calculation of myofilament force and total per- missive binding sites	147
C.2.9	Simulation of rapid slack/re-stretch maneuver in the QE model	147
C.2.10	Alternative model: 3 Independent XBs per RU	148
C.2.11	Simulation of fluorescence polarization measure- ments	150
C.3	Monte Carlo (MC) simulations of interacting RUs	151
C.3.1	Simulation Protocol	151
C.3.2	Simulated action of NEM-S1	152
C.3.3	Simulated action of non-functional TnC	152
C.4	Supplemental Results	153
C.4.1	Effects of solution method, number of RUs, and boundary conditions on solutions	153
C.4.2	Expanded Sensitivity Analysis results	154
C.4.3	k_{tr} is roughly proportional to the fraction of total activation not depending on XBs	155
C.4.4	Additional results from xTnC simulations	155
C.4.5	Model responses to time-varying Ca^{2+} input	155

LIST OF FIGURES

Figure 1.1:	Diagram of Myofilament Ca^{2+} activation	4
Figure 2.1:	Diagram of generalised functional coupling and feedback mechanisms in models of myocyte electromechanics.	13
Figure 2.2:	Comparison of simulated and experimentally measured canine ventricular myocyte electromechanics.	19
Figure 2.3:	Influence of AP morphology on I_{CaL} , Ca^{2+} transient, and unloaded shortening.	21
Figure 2.4:	Effect of fluo-3 on the apparent Ca^{2+} transient and potential errors in the prediction of shortening.	23
Figure 2.5:	Simulated unloaded shortening for epi-, mid-, and endocardial cells in response to measured Ca^{2+} transients corrected via flux-clamp protocol.	26
Figure 2.6:	Testing of hypothesized mechanisms of altered Ca^{2+} -contraction coupling in epicardial myocytes.	28
Figure 3.1:	Depiction of finite element meshes and myocyte subtype distribution used in this study.	45
Figure 3.2:	Myocardial activation time as calculated in the BASELINE simulation.	50
Figure 3.3:	Comparison of measured and model-generated fibre (E_{ff}) and cross-fibre (E_{cc}) strains at end-systole.	51
Figure 3.4:	Comparison of time courses of fibre strain (E_{ff}) in models and experiments.	53
Figure 4.1:	Scheme depicting individual regulatory-unit model	70
Figure 4.2:	Nearest-neighbor coupling modifies thin filament Ca^{2+} binding	75
Figure 4.3:	Different effects of cooperative coefficients γ_B , γ_M , and μ_M on Ca^{2+} sensitivities of force and the rate of force redevelopment	77
Figure 4.4:	Model responses from spatially-explicit Monte Carlo simulations on full-length filaments containing 26 regulatory units	79
Figure 4.5:	Effect of crossbridges on Ca^{2+} -dependence of TnC conformation	81
Figure 4.6:	Effects of added Pi on Ca^{2+} dependencies of steady-state force, residual force following re-stretch (F_{resid}), and k_{tr} in skinned rat myocardial preparations	83
Figure 4.7:	Tropomyosin-tropomyosin interactions potentiate crossbridge-dependent activation	85
Figure 4.8:	Model predictions of Ca^{2+} -force dynamics in intact cardiac muscle and the effects of tropomyosin-tropomyosin interactions and crossbridges on twitch activation	87

Figure 5.1:	Diagram of simplified Markov myofilament activation model with 3-state crossbridge cycle.	101
Figure 5.2:	Scheme for modeling effects of RLC phosphorylation on left ventricular mechanics.	103
Figure 5.3:	Characterization of survival, cardiac morphology, and gene expression in SM and DM mice.	106
Figure 5.4:	Quantification of myofibrillar protein phosphorylation in WT and DM myocardium.	108
Figure 5.5:	Recapitulation of RLC phosphorylation effects on skinned cardiac preparations using the Markov myofilament model.	111
Figure 5.6:	Effects of genotype on Ca^{2+} -contraction dynamics at 25°C	113
Figure 5.7:	Effects of genotype on twitch dynamics at 37°C	114
Figure 5.8:	Model reproduction of the effects of pacing frequency and genotype on Ca^{2+} -contraction dynamics.	116
Figure 5.9:	Exploration of model parameter changes required to reproduce genotype and frequency dependence of twitch responses.	117
Figure 5.10:	Measured and simulated effects of RLC phosphorylation on LV torsion.	118
Figure B.1:	Default fiber angle distribution for ventricular models	138
Figure B.2:	Extremes in measured transmural fiber angle gradients	139
Figure B.3:	Experimentally-measured time courses of transmural fiber strain.	140
Figure C.1:	Individual regulatory-unit (RU) and thin filament (TF) models	157
Figure C.2:	Description of cooperative coefficients	158
Figure C.3:	Diagram showing implementation of multiple crossbridges per RU	159
Figure C.4:	Comparison of the quazi-explicit and Monte Carlo model solution methods	160
Figure C.5:	Expanded sensitivity analysis, showing different effects of cooperative coefficients γ_B , γ_M , and μ_M on Ca^{2+} sensitivities of force and k_{tr}	161
Figure C.6:	Expanded sensitivity analysis at higher baseline myofilament activation	162
Figure C.7:	The fraction of activation due to Ca^{2+} as a function of k_{tr}	163
Figure C.8:	Effects of non-functional TnC on maximally-activated steady-state force and k_{tr}	164
Figure C.9:	Steady-state model response fit to pharmacologically slowed twitches	165
Figure C.10:	Model simulation of isometric twitch kinetics	166
Figure C.11:	Ca^{2+} transients used to drive twitch force time courses	167

LIST OF TABLES

Table 3.1:	Three-element Windkessel Model Parameters	48
Table 3.2:	Sensitivity of model-generated haemodynamics, activation delay and transmural fibre strain to perturbation	56
Table 4.1:	Model parameter sets.	74
Table 5.1:	Default Markov myofilament model parameters, including those describing hypothesized effects of RLC phosphorylation.	109
Table 5.2:	Alterations to default Markov myofilament model parameters re- quired to reproduce measurements of isometric twitch tension at 25°C.	118
Table A.1:	Combined model of cellular electromechanics: parameters al- tered from originals	132
Table A.2:	Fluo-3 kinetic parameters, from Naraghi (1997)	133
Table A.3:	Myofilament model parameters used in flux-clamp simulations	136
Table C.1:	Results of thin filament state generation	168
Table C.2:	Summary of twitch response properties under varying extracel- lular calcium concentration	169
Table C.3:	Summary of effects of tropomyosin-tropomyosin (Tm-Tm) cou- pling and XB binding on twitch activation time course	170
Table C.4:	Sensitivity Analysis - Hill Coefficient of steady-state force (n_H), $r = 1.0$	171
Table C.5:	Sensitivity Analysis - Hill Coefficient of steady-state force less than half maximal (n_1), $r = 1.0$	172
Table C.6:	Sensitivity Analysis - Hill Coefficient of steady-state force greater than half maximal (n_2), $r = 1.0$	173
Table C.7:	Sensitivity Analysis - Change in lower vs. upper Hill Coefficient of steady-state force (Δn_{1-2}), $r = 1.0$	174
Table C.8:	Sensitivity Analysis - Minimum k_{tr} (s^{-1}), $r = 1.0$	175
Table C.9:	Sensitivity Analysis - pCa of minimum k_{tr} , $r = 1.0$	176
Table C.10:	Sensitivity Analysis - pCa of mid-range k_{tr} , $r = 1.0$	177
Table C.11:	Sensitivity Analysis - Difference in pCa_{50} of steady-state force and k_{tr} , $r = 1.0$	178
Table C.12:	Sensitivity Analysis - pCa of half-maximal steady-state force, $r = 1.0$	179
Table C.13:	Sensitivity Analysis - Maximum k_{tr} (s^{-1}), $r = 1.0$	180
Table C.14:	Sensitivity Analysis - Fitted values of K_B , $r = 1.0$	181
Table C.15:	Sensitivity Analysis - Fitted values of the crossbridge duty cycle (δ), $r = 1.0$	182
Table C.16:	Sensitivity Analysis - Fitted values of g (s^{-1}), $r = 1.0$	183

Table C.17: Sensitivity Analysis - Minimum k_{tr} (s^{-1}), $r = 0.0$	184
Table C.18: Sensitivity Analysis - pCa of minimum k_{tr} , $r = 0.0$	185
Table C.19: Sensitivity Analysis - pCa of mid-range k_{tr} , $r = 0.0$	186
Table C.20: Sensitivity Analysis - Difference in pCa_{50} of steady-state force and k_{tr} , $r = 0.0$	187
Table C.21: Sensitivity Analysis - Maximum k_{tr} (s^{-1}), $r = 0.0$	188
Table C.22: Sensitivity Analysis - Fitted values of K_B , $r = 0.0$	189
Table C.23: Sensitivity Analysis - Fitted values of the crossbridge duty cycle (δ), $r = 0.0$	190
Table C.24: Sensitivity Analysis - Fitted values of g (s^{-1}), $r = 0.0$	191

ACKNOWLEDGEMENTS

I wish to thank first and foremost my doctoral adviser, Andrew McCulloch, for years of patient input and guidance. I am indebted to him for his commitment to my scientific and professional development, which I relied on continuously throughout the completion of this work. I gratefully acknowledge funding support secured by Dr. McCulloch on my behalf as well as individual awards that included a Predoctoral Fellowship from the American Heart Association Western States Affiliate, a scholarship from the UCSD Cardiovascular Science Fund, and an award from the UCSD Gordon Center for Engineering Leadership.

I benefitted in innumerable ways from generous help and encouragement provided by colleagues in the Cardiac Mechanics Research Group. In particular, I would like to acknowledge programming and debugging assistance provided by Fred Lionetti at many stages of this work. His help was vital to the implementation of the fully-coupled electromechanics algorithm described in Chapter 3. William Auyeung, Jared Tangney, and Shawn Sunu worked closely with me for several months to build and test the apparatus used for functional measurements of mouse papillary muscle preparations. I'm grateful to them for their hard work and support in that endeavor. Others, including many outside our lab group, provided input and assistance as co-authors on the publications listed below.

Chapter 2, in full, is a reprint of the published article "Mechanisms of transmurally-varying myocyte electromechanics in an integrated computational model." Campbell S.G., Flaim S.N., Leem C.H., and McCulloch A.D. *Philosophical Transactions of the Royal Society A*, 366:3361-3380, 2008. The dissertation author was the primary investigator and author of this paper.

Chapter 3, in full, is a reprint of the published article "Effect of Transmurally Heterogeneous Myocyte Excitation-Contraction Coupling on Left Ventricular Electromechanics." Campbell S.G., Howard E.J., Aguado-Sierra J., Coppola B.A., Omens J.H., Mulligan L.J., McCulloch A.D., and Kerckhoffs, R.C.P. *Experimental Physiology*. 95:541-552, 2009. The dissertation author was the primary investigator and author of this paper.

Chapter 4, in full, is a reprint of the published article "Coupling of Adjacent

Tropomyosins Enhances Crossbridge Mediated Cooperative Activation in a Markov Model of the Cardiac Thin filament.” Campbell S.G., Lionetti F.V., Campbell K.S., and McCulloch A.D. *Biophysical Journal*. 98, 2010. The dissertation author was the primary investigator and author of this paper.

Chapter 5 contains the dissertation author’s contributions to a manuscript in preparation at the time of writing entitled “Ventricular Myosin Light Chain 2 Phosphorylation S14A/S15A Mutant Knock-in Mice Display Novel Defects in Myocardial Torsion and Dilated Cardiomyopathy.” Sheikh F., Ouyang K., Campbell S.G., Chuang J., McCulloch A.D., and Chen J.

VITA

2004	B. S. in Bioengineering <i>suma cum laude</i> , Washington State University, Pullman, Washington
2004-2005	Design Engineer, Decagon Devices, Inc. Pullman, Washington
2005-2010	Graduate Research Assistant, University of California, San Diego
2006-2008	Graduate Teaching Assistant, University of California, San Diego
2010	Ph. D. in Bioengineering, University of California, San Diego

PUBLICATIONS

Campbell K.B., Simpson A.M., Campbell S.G., Granzier H.L., and Slinker B.K., “Dynamic Left Ventricular Elastance: A Model for Integrating Cardiac Muscle Contraction into Ventricular Pressure-Volume Relationships”, *Journal of Applied Physiology*, 104, 2008.

Campbell S.G., Flaim S.N., Leem C.H., and McCulloch A.D., “Mechanisms of transmurally-varying myocyte electromechanics in an integrated computational model”, *Philosophical Transactions of the Royal Society A*, 366, 2008.

Campbell S.G., Howard E.J., Aguado-Sierra J., Coppola B.A., Omens J.H., Mulligan L.J., McCulloch A.D., and Kerckhoffs, R.C.P., “Effect of Transmurally Heterogeneous Myocyte Excitation-Contraction Coupling on Left Ventricular Electromechanics”, *Experimental Physiology*, 95, 2009.

Campbell S.G., Lionetti F.V., Campbell K.B., and McCulloch A.D., “Coupling of Adjacent Tropomyosins Enhances Crossbridge Mediated Cooperative Activation in a Markov Model of the Cardiac Thin filament”, *Biophysical Journal*, 98, 2010.

ABSTRACT OF THE DISSERTATION

**The Role of Regulatory Light Chain Phosphorylation in Left
Ventricular Function**

by

Stuart Gaylon Campbell

Doctor of Philosophy in Bioengineering

University of California, San Diego, 2010

Professor Andrew D. McCulloch, Chair
Professor Jeffrey H. Omens, Co-Chair

Myosin regulatory light chain associates with the the motor protein myosin and plays an important but poorly understood role in regulating behavior of cardiac muscle. Mutations to regulatory light chain, including those which affect its phosphorylation by myosin light chain kinase, have been linked to cardiomyopathies. This protein, as well as several others, are linked together by complex structural interactions to form the myofilament system of cardiac muscle. These interactions make it difficult to extend in-vitro results using isolated regulatory light chain to physiologically relevant conditions. The purpose of this work was to formulate and test predictions regarding the effects of light chain phosphorylation on the function of the mammalian left ventricle. An approach combining experiments and computational models was developed and implemented to describe effects of light chain phosphorylation on function of the intact heart.

Chapter 1

Introduction

Heart function depends on the coordinated contraction and relaxation of its pumping chambers. During each beat, the signal to contract reaches cardiac muscle cells in the form of an electrical impulse. At the level of the cell, this electrical excitation causes rapid release of Ca^{2+} ions into the cytosol from intracellular stores. The cellular proteins responsible for producing contraction are activated by elevated Ca^{2+} levels, converting chemical energy stored as ATP into the mechanical work needed to pump blood from the heart. This process, from electrical stimulation to force production is known as cardiac excitation contraction coupling, or simply EC-coupling [1].

1.1 Cardiac Excitation-Contraction Coupling

Several cellular structures and a host of related proteins are involved in EC-coupling in ventricular myocytes [1]. Ion channels and their accessory proteins at the cell membrane are responsible for detecting and propagating the transient changes in membrane voltage that initiate contraction. The sarcoplasmic reticulum (SR) and associated proteins release large amounts of Ca^{2+} into the cytosol in response to excitation events and then carry out its re-uptake to initiate the end of contraction. In myocytes, the proteins actin and myosin are arranged into highly ordered structures of overlapping filaments known as sarcomeres. Within the sarcomeres, actin-myosin interactions responsible for generating contractile

force are regulated by Ca^{2+} sensitive protein complexes on actin filaments [2].

Because of its fundamental role in cardiac function, alterations to EC-coupling of one kind or another are a common feature of heart failure [3–5]. Mutations to EC-coupling related genes, especially those encoding sarcomeric proteins, are major causes of sudden cardiac death and hypertrophic cardiomyopathy in humans [6, 7]. Understanding the role of EC-coupling in the occurrence of any given cardiac disease is challenging because it encompasses so many complex and interrelated cellular processes [8].

1.2 Heterogeneous distribution of EC-coupling properties in the heart

Further complexity is introduced by the fact that within a single heart the properties of EC-coupling exhibited by individual cells differ significantly according to myocardial region [9–11]. Regional patterns in the morphology and duration of myocyte action potentials was among the first of many heterogeneous properties that have been described in the past 3 decades [12]. Since then, differences in ion current density [13, 14], Ca^{2+} transients [10, 15, 16], myosin isoform expression [17–20], myofilament protein phosphorylation [21, 22], and unloaded cell shortening [10, 15] have been noted. In some cases, it has been possible to correlate variations at the molecular level to functional differences among myocytes isolated from the respective myocardial regions [11, 20, 23], however, much remains to be learned about the practical implications of observed heterogeneities, even at the level of individual cells.

The same may be said of the role these heterogeneities play in the function of the whole heart. For instance, it is a commonly observed trend that cells in the outer, epicardial region of the left ventricle have shorter action potentials and Ca^{2+} transients, and tend to contract more rapidly than those in the inner or endocardial region [10, 15]. It has been proposed that this type of heterogeneity coordinates contraction in the heart [10, 24]. The hypothesis is that faster contraction in epicardial cells would allow them to ‘catch up’ to endocardial cells, which

are activated earlier during the cardiac cycle. However, a computational model (described in Chapter 3) predicts that heterogeneities affect ventricular deformation throughout most of systole, not just in its opening moments. Another conclusion from that work was that models of cardiac EC-coupling must be improved before further understanding of the impacts of cellular heterogeneity is achieved. It is likely that one such improvement will involve better representation of myofilament activation by Ca^{2+} .

1.3 Ca^{2+} buffering and cooperativity in cardiac myofilaments

It could be argued that the entire process of force generation by the myofilaments forms part of EC-coupling. Traditionally, EC-coupling has been considered complete at the point Ca^{2+} binds to troponin C (TnC), but two observations suggest that this view neglects potentially important mechanisms in the behavior of cardiac muscle. The first is that the Ca^{2+} affinity of TnC is increased nearly 10 fold by myosin binding to actin [25] (Figure 1.1). This means that during a twitch the capacity of TnC as a buffer of cytosolic Ca^{2+} cannot be considered constant. Furthermore, this suggests alterations to myofilament proteins such as phosphorylation of RLC can exert an indirect effect on TnC Ca^{2+} affinity and ultimately EC-coupling. This myosin-based increase in Ca^{2+} affinity also provides a mechanism by which sudden changes to sarcomere length applied to activated muscle can cause release of Ca^{2+} from the myofilaments, a phenomenon measured in skinned ferret ventricular muscle by Allen & Kentish [26].

The other observation is that post-translational modification of myofilament proteins alters their responsiveness to Ca^{2+} , meaning that properties of contraction cannot be inferred by the Ca^{2+} input alone [27]. Hence, an understanding of the relationship between excitation and the force produced by contraction depends critically on the properties and behavior of the myofilaments.

A basic feature of striated muscle function is its cooperative activation by Ca^{2+} [28]. Cooperativity describes the steep, sigmoidal relation observed between

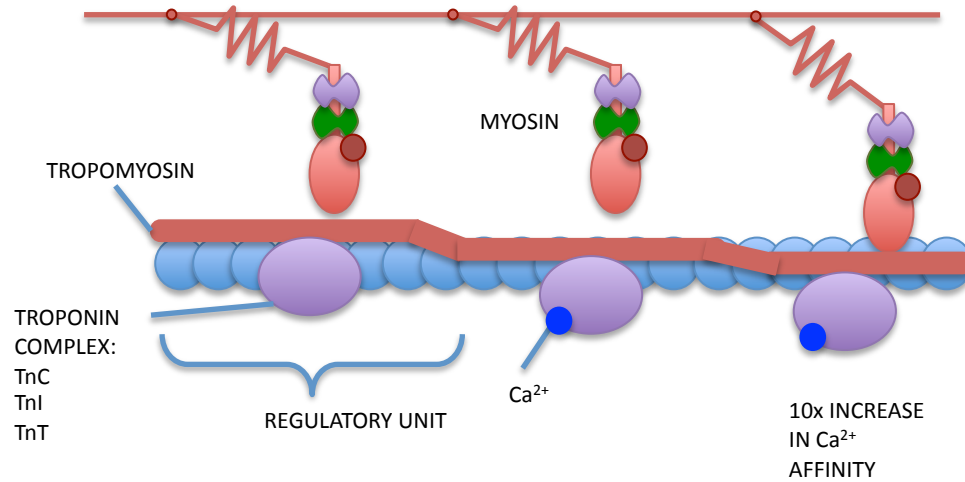


Figure 1.1: Diagram of Myofilament Ca^{2+} activation. This depiction is based on concepts reviewed in [2].

Ca^{2+} concentration and contractile force under steady-state conditions (*e.g.* in ref. [29]). Buffering of Ca^{2+} by the myofilaments shows this same cooperative pattern [30], and underscores the potential importance of myofilament cooperativity in an integrated view of EC-coupling.

The molecular origin of striated muscle cooperativity is widely believed to be end-to-end interactions arising between adjacent tropomyosin molecules on the actin thin filament [31, 32]. According to the steric blocking model of muscle regulation [2] (Figure 1.1), tropomyosin blocks myosin binding to actin under low Ca^{2+} conditions. Interactions among adjacent tropomyosins are thought to couple myosin binding sites such that they tend to be exposed in an ‘all-or-nothing’ fashion consistent with steeply cooperative behavior.

A number of theoretical and computational models have been developed to describe these and other putative mechanisms of myofilament cooperativity under steady-state conditions [33–38]. Others have been formulated for the purpose of predicting myofilament activation during the transient changes in $[\text{Ca}^{2+}]$ that occur in the beating heart [39–41]. Ideally, these models would be capable of translating biophysically detailed measurements of the kind only possible in skinned

muscle preparations into their true effects under physiologic conditions. In spite of the variety and number of published myofilament models, this exciting prospect remains largely unrealized.

1.4 Summary

The overarching objective of this dissertation was to develop, validate, and utilize computational tools to gain new insights into EC-coupling in the heart. Chapter 2 of this dissertation describes insights into cellular EC-coupling heterogeneity obtained with a computational model. In Chapter 3, the impacts of cellular heterogeneity on ventricular function were studied using a multi-scale model. Chapter 4 describes development of a mechanistic model of cardiac myofilament activation, which relates both constant and time-varying Ca^{2+} concentration to the force production. In Chapter 5, this model was used in conjunction with a series of experiments to elucidate the effects of myosin regulatory light chain (RLC) phosphorylation on left ventricular function.

References

- [1] Bers, D.M., 2002. Cardiac excitation-contraction coupling. *Nature*, 415:198–205.
- [2] Gordon, A.M., Homsher, E., and Regnier, M., 2000. Regulation of contraction in striated muscle. *Physiol Rev*, 80:853–924.
- [3] Lakatta, E.G., 1991. Excitation-contraction coupling in heart failure. *Hosp Pract (Off Ed)*, 26:85–8, 91–8.
- [4] Lakatta, E.G. and Sollott, S.J., 2002. The “heartbreak” of older age. *Mol Interv*, 2:431–46.
- [5] Wehrens, X.H., Lehnart, S.E., and Marks, A.R., 2005. Intracellular calcium release and cardiac disease. *Annu Rev Physiol*, 67:69–98.
- [6] George, A.L., 2009. Common genetic variants in sudden cardiac death. *Heart Rhythm*, 6:S3–9.

- [7] Tardiff, J.C., 2005. Sarcomeric proteins and familial hypertrophic cardiomyopathy: linking mutations in structural proteins to complex cardiovascular phenotypes. *Heart Failure Rev*, 10:237–48.
- [8] van Dijk, S.J., Hamdani, N., Stienen, G.J., and van der Velden, J., 2008. Myocardial adaptations in the failing heart: cause or consequence? *J Muscle Res Cell Motil*, 29:159–62.
- [9] Bryant, S.M., Shipsey, S.J., and Hart, G., 1999. Normal regional distribution of membrane current density in rat left ventricle is altered in catecholamine-induced hypertrophy. *Cardiovasc Res*, 42:391–401.
- [10] Cordeiro, J.M., Greene, L., Heilmann, C., Antzelevitch, D., and Antzelevitch, C., 2004. Transmural heterogeneity of calcium activity and mechanical function in the canine left ventricle. *Am J Physiol Heart Circ Physiol*, 286:H1471–9.
- [11] Wan, X., Bryant, S.M., and Hart, G., 2003. A topographical study of mechanical and electrical properties of single myocytes isolated from normal guinea-pig ventricular muscle. *J Anat*, 202:525–36.
- [12] Antzelevitch, C., Sicouri, S., Litovsky, S.H., Lukas, A., Krishnan, S.C., Diego, J.M.D., Gintant, G.A., and Liu, D.W., 1991. Heterogeneity within the ventricular wall. Electrophysiology and pharmacology of epicardial, endocardial, and M cells. *Circ Res*, 69:1427–49.
- [13] Rosati, B., Grau, F., Rodriguez, S., Li, H., Nerbonne, J.M., and McKinnon, D., 2003. Concordant expression of KChIP2 mRNA, protein and transient outward current throughout the canine ventricle. *J Physiol (Lond)*, 548:815–22.
- [14] Wang, H.S. and Cohen, I.S., 2003. Calcium channel heterogeneity in canine left ventricular myocytes. *J Physiol (Lond)*, 547:825–33.
- [15] Kondo, R., Dederko, D., Teutsch, C., Chrast, J., Catalucci, D., Chien, K., and Giles, W., 2006. Comparison of contraction and calcium handling between right and left ventricular myocytes from adult mouse heart: a role for repolarization waveform. *The Journal of Physiology*, 571:131.
- [16] Laurita, K.R., Katra, R., Wible, B., Wan, X., and Koo, M.H., 2003. Transmural heterogeneity of calcium handling in canine. *Circ Res*, 92:668–75.
- [17] Bouvagnet, P., Mairhofer, H., Leger, J.O., Puech, P., and Leger, J.J., 1989. Distribution pattern of alpha and beta myosin in normal and diseased human ventricular myocardium. *Basic Res Cardiol*, 84:91–102.

- [18] Carnes, C.A., Geisbuhler, T.P., and Reiser, P.J., 2004. Age-dependent changes in contraction and regional myocardial myosin heavy chain isoform expression in rats. *J Appl Physiol*, 97:446–53.
- [19] Dool, J.S., Mak, A.S., Friberg, P., Wahlander, H., Hawrylechko, A., and Adams, M.A., 1995. Regional myosin heavy chain expression in volume and pressure overload induced cardiac hypertrophy. *Acta Physiol Scand*, 155:396–404.
- [20] Stelzer, J.E., Norman, H.S., Chen, P.P., Patel, J.R., and Moss, R.L., 2008. Transmural variation in myosin heavy chain isoform expression modulates the timing of myocardial force generation in porcine left ventricle. *J Physiol (Lond)*, 586:5203–14.
- [21] Davis, J.S., Hassanzadeh, S., Winitsky, S., Lin, H., Satorius, C., Vemuri, R., Aletras, A.H., Wen, H., and Epstein, N.D., 2001. The overall pattern of cardiac contraction depends on a spatial gradient of myosin regulatory light chain phosphorylation. *Cell*, 107:631–41.
- [22] Hidalgo, C., Wu, Y., Peng, J., Siems, W.F., Campbell, K.B., and Granzier, H., 2006. Effect of diastolic pressure on MLC2v phosphorylation in the rat left ventricle. *Arch Biochem Biophys*, 456:216–23.
- [23] Flaim, S.N., Giles, W.R., and McCulloch, A.D., 2006. Contributions of sustained INa and IKv43 to transmural heterogeneity of early repolarization and arrhythmogenesis in canine left ventricular myocytes. *Am J Physiol Heart Circ Physiol*, 291:H2617–29.
- [24] Kerckhoffs, R.C.P., Bovendeerd, P.H.M., Kotte, J.C.S., Prinzen, F.W., Smits, K., and Arts, T., 2003. Homogeneity of cardiac contraction despite physiological asynchrony of depolarization: a model study. *Ann Biomed Eng*, 31:536–47.
- [25] Davis, J.P., Norman, C., Kobayashi, T., Solaro, R.J., Swartz, D.R., and Tikunova, S.B., 2007. Effects of thin and thick filament proteins on calcium binding and exchange with cardiac troponin C. *Biophys J*, 92:3195–206.
- [26] Allen, D.G. and Kentish, J.C., 1988. Calcium concentration in the myoplasm of skinned ferret ventricular muscle following changes in muscle length. *J Physiol (Lond)*, 407:489–503.
- [27] Kobayashi, T. and Solaro, R.J., 2005. Calcium, thin filaments, and the integrative biology of cardiac contractility. *Annu Rev Physiol*, 67:39–67.
- [28] Bremel, R.D. and Weber, A., 1972. Cooperation within actin filament in vertebrate skeletal muscle. *Nature New Biol*, 238:97–101.

- [29] Dobesh, D.P., Konhilas, J.P., and de Tombe, P.P., 2002. Cooperative activation in cardiac muscle: impact of sarcomere length. *Am J Physiol Heart Circ Physiol*, 282:H1055–62.
- [30] Hofmann, P.A. and Fuchs, F., 1987. Evidence for a force-dependent component of calcium binding to cardiac troponin C. *Am J Physiol*, 253:C541–6.
- [31] McLachlan, A.D. and Stewart, M., 1975. Tropomyosin coiled-coil interactions: evidence for an unstaggered structure. *J Mol Biol*, 98:293–304.
- [32] Pan, B.S., Gordon, A.M., and Luo, Z.X., 1989. Removal of tropomyosin overlap modifies cooperative binding of myosin S-1 to reconstituted thin filaments of rabbit striated muscle. *J Biol Chem*, 264:8495–8.
- [33] Dobrunz, L.E., Backx, P.H., and Yue, D.T., 1995. Steady-state $[Ca^{2+}]_i$ -force relationship in intact twitching cardiac muscle: direct evidence for modulation by isoproterenol and EMD 53998. *Biophys J*, 69:189–201.
- [34] McKillop, D.F. and Geeves, M.A., 1993. Regulation of the interaction between actin and myosin subfragment 1: evidence for three states of the thin filament. *Biophysical Journal*, 65:693–701.
- [35] Rice, J.J., Stolovitzky, G., TU, Y., and Tombe, P.P.D., 2003. Ising model of cardiac thin filament activation with nearest-neighbor cooperative interactions. *Biophys J*, 84:897–909.
- [36] Shiner, J.S. and Solaro, R.J., 1982. Activation of thin-filament-regulated muscle by calcium ion: considerations based on nearest-neighbor lattice statistics. *Proc Natl Acad Sci USA*, 79:4637–41.
- [37] Smith, D.A. and Geeves, M.A., 2003. Cooperative regulation of myosin-actin interactions by a continuous flexible chain II: actin-tropomyosin-troponin and regulation by calcium. *Biophys J*, 84:3168–80.
- [38] Zou, G. and Phillips, G.N., 1994. A cellular automaton model for the regulatory behavior of muscle thin filaments. *Biophys J*, 67:11–28.
- [39] Landesberg, A. and Sideman, S., 1994. Mechanical regulation of cardiac muscle by coupling calcium kinetics with cross-bridge cycling: a dynamic model. *Am J Physiol*, 267:H779–95.
- [40] Niederer, S.A., Hunter, P.J., and Smith, N.P., 2006. A quantitative analysis of cardiac myocyte relaxation: a simulation study. *Biophysical Journal*, 90:1697–722.
- [41] Rice, J.J., Winslow, R.L., and Hunter, W.C., 1999. Comparison of putative cooperative mechanisms in cardiac muscle: length dependence and dynamic responses. *Am J Physiol*, 276:H1734–54.

Chapter 2

Mechanisms of transmurally-varying myocyte electromechanics in an integrated computational model

Abstract

The mechanical properties of myocardium vary across the transmural aspect of the left ventricular wall. Some of these functional heterogeneities may be related to differences in excitation-contraction coupling characteristics that have been observed in cells isolated from the epicardial, midmyocardial, and endocardial regions of the left ventricle of many species, including canine. Integrative models of coupled myocyte electromechanics are reviewed and used here to investigate sources of heterogeneous electromechanical behaviour in these cells. The simulations 1) illustrate a previously unrecognised role of the transient outward potassium current in mechanical function and 2) suggest that there may also exist additional heterogeneities affecting crossbridge cycling rates in cells from different transmural regions.

2.1 Introduction

Although three-dimensional wall strains are highly inhomogeneous across the transmural aspect of the ventricular wall [1], several studies showed that fibre strain distributions are relatively uniform during contraction [2–4] owing to the effects of torsion and myofibre angle distribution [5]. However, more recent studies using higher resolution measurements have revealed significant spatial and temporal differences in myofibre strain in the left ventricular (LV) wall throughout the cardiac cycle [6, 7]. Heterogeneities of structure, function, and composition have been reported in myocardial tissue and in myocytes isolated from different regions in the LV wall. These heterogeneities are likely to contribute to complex transmural patterns of myofibre strain, though the precise nature of these relationships and their relevance to global heart function are not fully understood.

2.1.1 Transmural heterogeneity

Transmural heterogeneity of electrical activity and Ca^{2+} -handling observed in tissue preparations [8] can be explained largely by intrinsic differences in individual myocytes isolated from the endocardial, midmyocardial, and epicardial regions of the LV wall [9, 10]. Action potential (AP) morphology is different among the three ventricular cell subtypes, with epi- and midmyocardial cells showing a prominent phase 1 notch that is essentially absent in endocardial cells [9]. Magnitude of the notch is primarily determined by the transient outward K^+ current (I_{to1}), which is much smaller in endocardial cells [11] as a result of transmural gradients in the expression of K^+ channel interacting proteins (KChIPs) [12]. Action potential duration (APD) has a significant transmural variation, with midmyocardial cells exhibiting the longest APD [9]. A transmural gradient in L-type Ca^{2+} channel current (I_{CaL}) density was observed in one study, with endocardial cells showing higher values than epi- and midmyocardial cells [13]. This finding remains controversial, however, as several other studies showed no difference in I_{CaL} density among the three cell types [14–16]. Finally, expression of sarcoplasmic reticulum Ca^{2+} -ATPase (SERCA) is highest in epicardial cells and most likely explains

faster decay of the Ca^{2+} transient and increased sarcoplasmic reticulum (SR) load observed in these cells [10, 15].

Fewer studies have focused on transmural variations in passive and active mechanical properties of isolated myocytes, though some important differences have been documented. Transmural variation of passive myocyte stiffness has been observed in the rat heart and is associated with changes in overall titin expression levels [17]. The ratio of titin isoform expression is also thought to modulate passive myocyte stiffness [18], and transmural gradients in this ratio have been observed in the canine LV [19]. Cazorla and co-workers [20] identified distinct length-tension relations between epicardial and endocardial cells isolated from rat and ferret hearts. Epicardial myocytes have been shown to reach peak unloaded shortening more quickly than those from the endocardium in both guinea pig [21] and dog [15].

Cordeiro and co-workers [15] have conducted the only experimental study to date examining transmural heterogeneity of ionic currents, Ca^{2+} -handling, and mechanical function (electromechanics). They identified several key distinctions in the time course of unloaded shortening among canine LV epi-, mid-, and endocardial cells. Endocardial cells displayed a comparatively longer delay in the onset of shortening, while epicardial cells showed the fastest shortening kinetics among the cell subtypes. Significantly, this study did not show any differences in I_{CaL} density or excitation-contraction (EC) coupling gain among the three myocyte subtypes. Furthermore, amplitudes of the Ca^{2+} transient and the peak percentage of cell shortening were not seen to be significantly different among epi-, mid-, and endocardial cells. The authors concluded that some, but not all of the differences in shortening time course were related to AP morphology and Ca^{2+} -handling, leaving room for additional, as yet unidentified sources of mechanical heterogeneity.

Computational models of ventricular myocyte EC coupling have been useful for investigating the mechanisms of functional differences across the LV wall [22–25]. With the exception of the work by Solovyova *et al.* [23], none of these models include the myofilament interactions responsible for cell shortening. Several of the heterogeneities mentioned above were mechanistically integrated into a

recent model of canine EC coupling [26] by our group in the form of three different parameter sets, one for each myocyte subtype [25]. This model successfully reproduced several of the observations of Cordeiro *et al.* (2004), including differences in AP morphology and Ca^{2+} handling among cell subtypes.

2.1.2 Models of myocyte electromechanics

Most models of myocyte electromechanics are combinations of previously published models of EC coupling subsystems, coupled via state variables including Ca^{2+} , membrane potential, sarcomere length, pH, and ATP. Figure 2.1 summarises the mechanisms of coupling and feedback now represented in various systems models of ventricular myocytes. While no single published model includes all these mechanisms, this figure demonstrates the feasibility of an integrated model of this type.

Modelling of ionic currents giving rise to the cardiac AP is the most mature of those subsystems involved in cellular electromechanics (reviewed in detail by [27]). Recent developments in the modelling of myocyte electrophysiology (EP) include continuous-time Markov models allowing for more mechanistic representations of ion channel behaviour individually (e.g. [28]) and in the context of the whole cell [25, 29]. Detailed understanding of the events underlying Ca^{2+} -induced Ca^{2+} release (CICR) is relatively recent, and as such models of the same have developed more slowly than those of myocyte EP [30]. The most advanced local control models of CICR [31] are too computationally demanding to be used in multiscale cardiac modelling. More recent models have used timescale decomposition to capture important properties such as graded Ca^{2+} release while remaining computationally practical for integration into larger scale analyses [26, 32]. Models of myofilament activation and force production have also been slow to mature due to gaps that remain in the understanding of actin-myosin interactions and their role in thin filament activation [33]. Recent myofilament models have addressed these deficiencies to some degree, and reproduce many experimentally observed characteristics of cardiac muscle contraction [34–37].

Integrated models of myocyte electromechanics have been profitably used

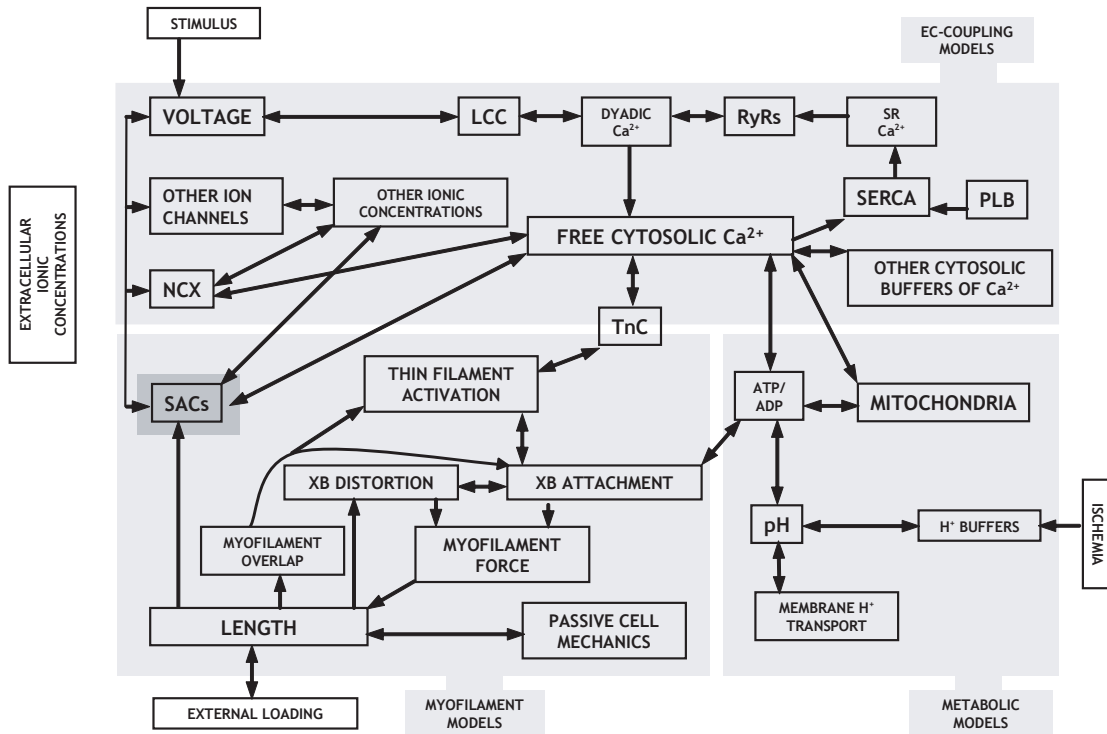


Figure 2.1: Diagram of generalised functional coupling and feedback mechanisms in models of myocyte electromechanics. Entities that broadly couple cell processes include voltage, Ca^{2+} , length, ATP/ADP, and pH. Single arrows represent one-way coupling; double-headed arrows indicate two-way interaction between components. Interactions not shown for clarity include effects of pH on XB attachment, TnC, NCX, RyRs, and SERCA; effects of length on RyRs; and effects of ATP on SERCA and NCX. Abbreviations: LCC (L-type Ca^{2+} channel), RyRs (ryanodine receptors), SERCA (sarcoplasmic reticulum Ca^{2+} -ATPase), PLB (phospholamban), NCX ($\text{Na}^+/\text{Ca}^{2+}$ exchanger), SACs (stretch-activated channels), TnC (troponin C), XB (crossbridge).

to investigate many whole-cell phenomena not within the grasp of smaller models. One of the first models to include several EC-coupling mechanisms in equal detail was that of Rice and co-workers [38], which was used to examine aspects of short-term interval-force relations in cardiac muscle. Other subsequent models have been used to examine the relationship between force production and pacing interval [39, 40]. Iribe *et al.* [40] used an integrated model of myocyte function to describe the role of Ca^{2+} /calmodulin-dependent kinase II in producing Ca^{2+} transient alternans during the decay of post-extrasystolic potentiation.

Models of myocyte electromechanics have also been extensively used to investigate the dynamic relationship that exists between length or tension of myocytes and their electrical activity. Acute alteration of the AP by changes in myocyte length (mechanoelectric feedback) has been modelled in a number of studies [41–44]. Others have used integrated models to evaluate proposed mechanisms underlying the slow force response to stretch [45, 46].

Other models have added components such as mitochondrial metabolism and Ca^{2+} uptake [47] and pH regulation [48] to fully-coupled myocyte models. These modifications enabled analysis of metabolic control in the heart under normal conditions [47] and of the mechanisms by which acidosis affects myocyte contractility during ischemia [48].

Here, we describe our use of a coupled computational model of electromechanics to investigate mechanisms underlying transmural variations in myocyte function in the canine LV. We coupled recent models of canine EC coupling [25] and myofilament force production [37] in order to test the hypothesis that known heterogeneities in AP morphology and Ca^{2+} transients are sufficient to explain experimentally observed differences in time courses of unloaded cell shortening. The analysis suggests an important role for transmural variations in I_{to1} in determining regional shortening and also indicates that variations in crossbridge function may be present.

2.2 Methods

2.2.1 Model of myocyte electromechanics

We started with the endocardial canine myocyte model formulated by Flaim, *et al.* [25] and coupled it to the recent model of myofilament force production and cell mechanics of Rice and co-workers [37]. Forward coupling between EP/Ca²⁺-handling and myofilaments was accomplished by driving the myofilament model with the variable representing $[Ca^{2+}]_i$. Reverse coupling was achieved by replacing the static Ca²⁺ buffering by TnC low-affinity regulatory sites used in the model of Flaim *et al.* [25] with dynamic flux of Ca²⁺ on and off the myofilaments described by the Rice model. The modified differential equation describing $[Ca^{2+}]_i$ as well as other details of model coupling can found in Appendix A.

The complete electromechanics model was programmed in MATLAB and run for >50 beats to achieve steady-state conditions for each parameter set used. A basic cycle length (BCL) of 2000 ms was used for all simulations to allow valid comparison with the experiments of Cordeiro *et al.* (2004).

AP clamp protocols were simulated by prescribing the membrane voltage with an appropriate time-varying function rather than allowing it to be determined by membrane currents. The epicardial and endocardial AP waveforms used in AP clamp simulations were digitised from representative traces reported by Cordeiro *et al.* (2004).

2.2.2 Modification of published model parameters

All adjustments to model parameters from those originally published are presented in Appendix A. These adjustments were intentionally kept to a minimum, and were only made to correct the largest differences between experimental data and model behaviour. EP/Ca²⁺-handling parameter sets for epi-, mid-, and endocardial cells set by Flaim, *et al.* [25] were retained, along with those described in the original canine EC coupling model of Greenstein *et al.* [26]. The lone exception was an increase in the number of Ca²⁺ release units (CaRU) from 50000 to 75000 to increase the amplitude of the Ca²⁺ transient at a BCL of 2000 ms to

more typically observed levels. This same parameter value has been used by others [46].

A few minor changes to the original myofilament model parameters [37] were made to increase the stability of unloaded shortening responses in the coupled electromechanics model. Alterations to parameters governing myofilament Ca^{2+} sensitivity and cooperativity were also made in order to give a time course and magnitude of shortening that agreed qualitatively with experiments [15]. These and other adjustments to myofilament model parameters described throughout the remainder of this paper are listed in detail in Appendix A.

2.2.3 Modelling of the exogenous Ca^{2+} buffer fluo-3

We represented the buffering of intracellular Ca^{2+} by fluo-3 dye using a standard differential equation for simple buffering (Equation REF!!!! S2 in Appendix A). Ca^{2+} transients measured experimentally reflect the time course of Ca^{2+} bound to the indicator molecule ($[\text{Ca}^{2+}]_{\text{fluo}}$) and are often calibrated to correspond to concentration of cytosolic Ca^{2+} . To mimic this measurement, the model reports the time course of $[Ca_{2+}]_{\text{fluo}}$ scaled to vary between the minimum and maximum values of $[\text{Ca}^{2+}]_i$. We have called this quantity $[\text{Ca}^{2+}]_{i/\text{app}}$, the apparent cytosolic Ca^{2+} concentration. This modification enables direct comparison of model output with experimental measurements.

In all simulations where fluo-3 was present, the concentration of this indicator in the cytosol was assumed to be $15 \mu\text{M}$, corresponding to the concentration of fluo-3 used in bathing solutions by Cordeiro *et al.* (2004). New steady-state conditions for the coupled model had to be found when fluo-3 was included, as the buffering action of this indicator was substantial enough to alter SR load and other model values. This was accomplished as before by running the model for >50 beats in the presence of $15 \mu\text{M}$ fluo-3.

2.2.4 Simulation of shortening under clamped $[Ca^{2+}]_i$ and Ca^{2+} -flux conditions

The myofilament model of Rice and co-workers [37] was used independently of the coupled electromechanics model to study Ca^{2+} -contraction dynamics under various conditions. Two Ca^{2+} input modes were used in these simulations. The first allows myocyte contraction and shortening to be driven with a prescribed Ca^{2+} transient, which automatically sources as much Ca^{2+} flux as needed to maintain the command $[Ca^{2+}]_i$ signal. This mode was used to study the shortening response to specific Ca^{2+} transients.

A second type of Ca^{2+} -clamp was created whereby a fixed Ca^{2+} flux, J_{clamp} , was used to drive shortening. This approach is similar to one originally used to estimate Ca^{2+} flux across the SR [49]. A differential equation describing the time course of $[Ca^{2+}]_i$ was added to the original myofilament model equations in which $d[Ca^{2+}]_i/dt$ is set equal to the sum of different Ca^{2+} fluxes:

$$\begin{aligned} \frac{d[Ca^{2+}]_i(t)}{dt} = & J_{clamp}(t) + J_{fluo}([Ca^{2+}]_i, t) \\ & + J_{TnC}([Ca^{2+}]_i, t) + J_{SERCA}([Ca^{2+}]_i, t) \end{aligned} \quad (2.1)$$

where J_{fluo} , J_{TnC} , and J_{SERCA} are $[Ca^{2+}]_i$ and time-dependent Ca^{2+} fluxes describing buffering by fluo-3, buffering by TnC, and uptake by SERCA, respectively. The fluxes representing buffering of Ca^{2+} by fluo-3 and TnC are calculated as described above and in the original work of Rice *et al.* [37], while uptake of SERCA is modelled as in the EP model with the assumption that SR content is fixed (see Appendix A for details). This flux-clamp mode allows the Ca^{2+} transient driving contraction to be flexibly determined under changing conditions such as the presence and absence of fluo-3.

2.3 Results

2.3.1 Model Validation

The fully-coupled electromechanical model with endocardial myocyte parameters produced a time course of EC-coupling events comparable to those reported experimentally (Figure 2.2, *a* and *b*). The model displayed unloaded cell shortening characteristics of latency to onset, time to peak, and peak percentage of shortening that agreed with mean experimental values to within the reported standard deviations [15]. The model showed qualitative agreement with other experimentally reported values. Model time from peak of unloaded shortening to 90% relaxation (RT90) was 222 ms, compared with a mean value of 265 ms [15]. Modelled Ca^{2+} transients (time course of Ca^{2+} bound to fluo-3 and scaled to peak free cytosolic Ca^{2+}) showed a latency to onset of 16 ms (vs. 17.4 ms experimental mean), time to peak of 161 ms (vs. 193 ms), RT90 of 489 ms (vs. 566 ms), and peak cytosolic Ca^{2+} concentration of 580 nM (vs. 663 nM). Action potential duration (APD) of the endocardial model was 326 ms, compared with a mean value of 266 reported in experiments at the same BCL of 2000 ms [15].

2.3.2 Modelled transmural heterogeneity of myocyte electromechanics

Parameter sets describing heterogeneous properties of membrane currents and Ca^{2+} handling for epicardial and midmyocardial cells were proposed by Flaim *et al.* [25]. We performed simulations of unloaded shortening using these parameter sets in the electromechanics model to evaluate the potential for these proposed differences to explain distinctions in mechanical function reported by Cordeiro *et al.* [15].

The transmural trend in APD achieved in the original model (Flaim *et al.* 2006) was retained in the electromechanics model and agrees with Cordeiro *et al.* [15] and other reports [9]. Trends in cell mechanical function between the three cell types agreed qualitatively with those reported experimentally, including

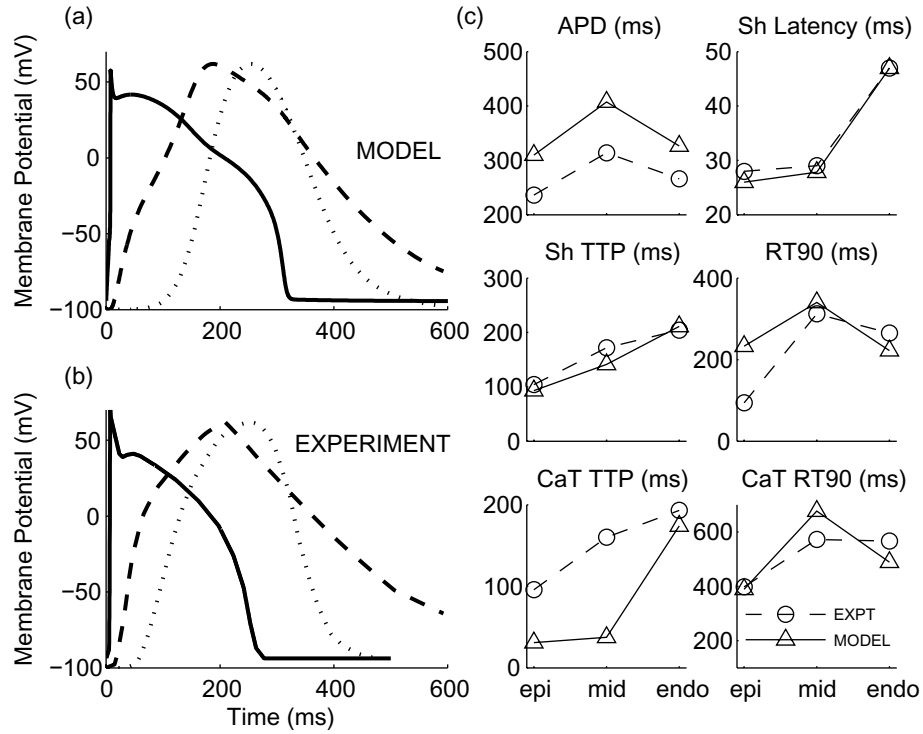


Figure 2.2: Comparison of simulated and experimentally measured canine ventricular myocyte electromechanics. (a) Simulated and (b) measured time courses of endocardial myocyte membrane potential (solid traces), $[Ca^{2+}]_{i/app}$ (dashed traces, see Methods for definition), and unloaded cell shortening (dotted traces). $[Ca^{2+}]_{i/app}$ and shortening traces have been scaled and are displayed in arbitrary units to facilitate comparison. (c) Comparison of model (triangles, solid lines) and experimentally reported (circles, dashed lines) transmural trends in EC coupling. Abbreviations: Sh (shortening), CaT (Ca^{2+} transient), TTP (time to peak); RT90 (time from peak to 90% relaxation). (All experimental traces and values taken from Cordeiro *et al.* [15].)

1) longer latency to the onset of contraction in endocardial cells, 2) shorter time to peak shortening in epicardial cells, and 3) longer RT90 in midmyocardial cells (Figure 2.2*c*). Peak percent cell shortening matched measurements to within the reported standard deviation for all three cell types (not shown), indicating a reasonable relation between peak systolic $[Ca^{2+}]_i$ and myofilament Ca^{2+} sensitivity.

Conversely, the model failed to reproduce the significantly reduced RT90 observed experimentally in epicardial cells compared with the other cell types (Figure 2.2*c*). The epicardial and midmyocardial parameter sets both yielded Ca^{2+} transients with a rapid time to peak that was not fully consistent with measured representative traces or mean values [15]. The midmyocardial cell model also produced a Ca^{2+} transient RT90 200 ms longer than that of the endocardial model, while this difference was not seen in experiments.

2.3.3 AP-clamp simulations

Since the model showed a strong dependence of SR Ca^{2+} release on the AP waveform in epicardial and midmyocardial cells, the influence of AP morphology on Ca^{2+} release and shortening was examined in the absence of other differences (such as SR load) using AP clamp conditions. Initial conditions for all model state variables were taken from the midmyocardial model run to steady-state, after which a single beat was elicited in response to a representative endocardial or epicardial AP digitised from the literature [15].

L-type Ca^{2+} channel currents (I_{CaL}), Ca^{2+} transients, and cell shortening in response to epicardial and endocardial AP waveforms showed large differences in amplitude and time course (Figure 2.3). The epicardial AP generated a peak current five times greater than that of the endocardial AP. In contrast, the endocardial AP produced a marked prolongation of the secondary phase of I_{CaL} , though the respective currents ultimately terminated at about the same time, around 230 ms.

Differences in I_{CaL} had a clear effect on downstream EC-coupling events. The peak of the Ca^{2+} transient under epicardial AP clamp arrived 120 ms faster and was 40% larger than that of the endocardial AP (Figure 2.3*b*), corresponding

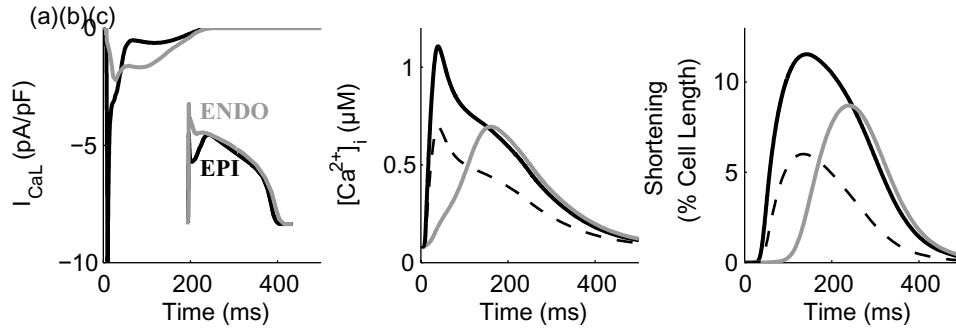


Figure 2.3: Influence of AP morphology on I_{CaL} , Ca^{2+} transient, and unloaded shortening. Results shown are simulated responses to typical epi- or endocardial APs (inset to panel (a), digitised from [15]) in the electromechanics model. Solid and shaded traces correspond to epi- and endocardial AP clamp, respectively. Dashed trace in (c) shows unloaded shortening by the model in response to a clamped Ca^{2+} transient shown in (b) as the dashed trace (see text for details).

to the greater amount of triggering Ca^{2+} in the initial phase of I_{CaL} . The endocardial AP-elicited Ca^{2+} transient reached a peak magnitude above 50% that of the other transient despite the five-fold smaller initial trigger current through a longer secondary phase of I_{CaL} (Figure 2.3a, shaded trace). Onset of unloaded shortening was plainly different between the two cases, with shortening in response to the endocardial AP starting 30 ms after that of the epicardial AP (Figure 2.3c). Peak unloaded cell shortening in response to the epicardial AP was reached 100 ms faster than that observed under endocardial AP, and was 30% greater in magnitude.

To understand better the relationship between Ca^{2+} transient time course and unloaded shortening dynamics, we simulated an unloaded shortening event under a specified or clamped Ca^{2+} transient corresponding to a scaled version of the epicardial AP-elicited transient (Figure 2.3a, dashed trace). The transient was scaled such that its peak corresponded in magnitude with that of the endocardial transient in an attempt to isolate effects of transient shape from those of absolute magnitude. Unloaded shortening during Ca^{2+} clamp (Figure 2.3c, dashed line) displayed shortening latency, time to peak, and time from peak to 90% relaxation all well within 10% of those same values in epicardial AP-driven shortening (Figure 2.3c, solid trace), showing that the time course of the Ca^{2+} transient was the

primary determinant of shortening dynamics on this scale. Surprisingly, the contraction driven by the scaled epicardial Ca^{2+} transient resulted in a 30% reduction in peak shortening compared with that from the endocardial AP clamp, in spite of sharing the same absolute magnitude of peak cytosolic Ca^{2+} .

2.3.4 Influence of an exogenous buffer on Ca^{2+} transients and unloaded shortening

Discrepancies between model-predicted and experimentally observed Ca^{2+} transients for midmyocardial and epicardial cells limited the ability of the electromechanics model to discern potential sources of transmural heterogeneity downstream of Ca^{2+} -handling. We therefore simulated unloaded shortening driven directly by representative Ca^{2+} transients measured experimentally in the three cell types.

Before doing this, we added a simple representation of fluo-3 buffering and kinetics to the electromechanics model (as described in Methods) to assess its effects on the Ca^{2+} transient and shortening. Concentration of fluo-3 was set to 15 μM , consistent with the concentration used in experiments [15], and the model was run to steady state. We then compared $[\text{Ca}^{2+}]_{i/app}$ with $[\text{Ca}^{2+}]_i$ from the model containing no fluo-3 (Figure 2.4a). Addition of the fluo-3 had negligible impact on the time to peak Ca^{2+} , but lowered the magnitude of the peak by 20% through buffering of free Ca^{2+} . Time from peak to 90% decay of $[\text{Ca}^{2+}]_{i/app}$ was increased by 40% over the same value calculated from $[\text{Ca}^{2+}]_i$. This prolongation of the Ca^{2+} transient is caused by competition for free Ca^{2+} between the high affinity indicator and the usual Ca^{2+} uptake pathways, but also possesses an apparent component that reflects the dissociation kinetics of the dye. Overall, this simulation suggests that the apparent Ca^{2+} transient as assessed by indicator fluorescence is blunted at its peak and decays more slowly in comparison with the actual transient in the absence of this exogenous buffer.

To assess the type and magnitude of errors that could be introduced by driving cell shortening directly with measured indicator fluorescence, $[\text{Ca}^{2+}]_{i/app}$ (Figure 2.4a, dashed trace) was used to drive shortening in the myofilament model

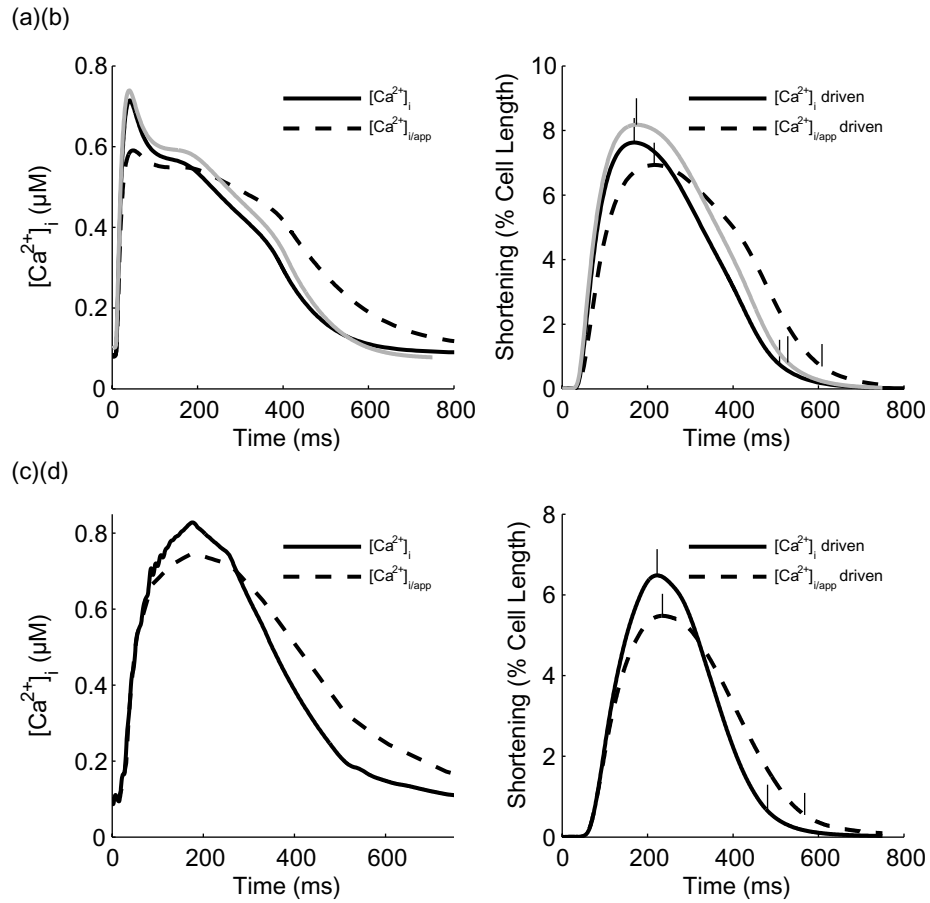


Figure 2.4: Effect of fluo-3 on the apparent Ca^{2+} transient and potential errors in the prediction of shortening in response. (a) $[\text{Ca}^{2+}]_i$ (solid trace) taken from the midmyocardial cell model with no fluo-3 present plotted with $[\text{Ca}^{2+}]_{i/app}$ from the same model in the presence of $15 \mu\text{M}$ fluo-3. (b) Simulated cell shortening in response to the respective Ca^{2+} signals shown in (a), e.g., solid trace is shortening in response to the solid trace in (a) and so on. Shaded traces in (a) and (b) correspond to flux-clamp validation as described in the text. (c) is similar to (a), but now compares a calibrated fluo-3 fluorescence signal (dashed trace, digitised from Cordeiro *et al.* [15] with $[\text{Ca}^{2+}]_i$ predicted via the flux-clamp protocol (solid trace). (d) Shortening in response to the respective Ca^{2+} inputs shown in (c). Tick marks in (b) and (d) indicate peak shortening and 90% relaxation.

(Figure 2.4*b*, dashed trace). Peak shortening was reduced by 10%, while the time to peak shortening and RT90 were increased by 32% and 15% over original values, respectively. These differences indicated the need for a method to estimate the true time course of intracellular Ca^{2+} from fluorescence measurements.

2.3.5 Flux-clamp validation

The electromechanics model was used to generate a test case for the predictive function of the flux-clamp input mode. An input flux, J_{clamp} , was determined from the electromechanics model run to steady-state in the presence of 15 μM fluo-3, and then used to drive the flux-clamped myofilament model in the absence of fluo-3. The resulting Ca^{2+} transient and unloaded shortening (Figure 2.4, *a* and *b*, shaded traces) were compared to traces from the base model. The predicted Ca^{2+} transient was close in magnitude and shape to that of the original simulation, and unloaded shortening time course showed only slight differences ($< 8\%$ change from baseline for magnitude of shortening, time to peak, and RT90).

2.3.6 Shortening responses to realistic Ca^{2+} -transients

We used the flux-clamp protocol to estimate the true Ca^{2+} transient from a representative time course of indicator fluorescence from a midmyocardial cell [15]. Differences similar to those seen in simulations using the fully coupled model (Figure 2.4*a*) can be observed between experimentally measured $[\text{Ca}^{2+}]_{i/app}$ and $[\text{Ca}^{2+}]_i$ estimated using flux-clamp (Figure 2.4*c*). These included increased magnitude and faster relaxation for the estimated transient. Estimated shortening in the absence of fluo-3 generated with the flux-clamped model (Figure 2.4*d*, solid trace) was compared with shortening driven directly with the fluorescence data (Figure 2.4*d*, dashed trace) using the same myofilament model parameters in both cases. The contraction driven by fluorescence displayed differences in magnitude of shortening (-15%), time to peak (+7.6%), and RT90 (+28.5%) compared with flux-clamped shortening.

The parameters of the myofilament model were adjusted until time to peak

shortening and shortening magnitude under midmyocardial cell flux-clamp were within the standard deviations of measured mean values Cordeiro:2004p231. The adjusted parameter set corresponded to a steady-state force- Ca^{2+} relation possessing a half-activation value (Ca_{50}) and Hill coefficient (nH) of $1.0 \mu\text{M}$ and 3.5 , respectively. Latency to onset of shortening using these parameters was 12 ms slower than the experimentally reported mean, however, this may be attributed to noise in the original fluorescent signal or error in digitising the trace as even small differences in the initial rising phase of the Ca^{2+} transient have a strong effect on shortening latency. Additionally, RT90 was 54 ms shorter than the experimentally reported mean of 312 ms . This is most likely due to a secondary, slower time constant of relaxation seen in the representative shortening traces for mid- and endocardial cells (c.f. Cordeiro *et al.* [15], Figure 2.2) which the model did not reproduce.

Retaining the myofilament model parameter set used to fit reported mid-myocardial cell shortening, the flux-clamp protocol was used to determine driving fluxes matching representative epicardial and endocardial fluorescence traces, and unloaded shortening in the absence of indicator was predicted as previously (Figure 2.5a). The myofilament model parameters adjusted to match the midmyocardial shortening response also resulted in good reproduction of reported values for endocardial cells (Figure 2.5b). Shortening RT90 for the mid- and endocardial cell responses showed the same systematic deviation from reported mean values and displayed the correct transmural trend (Figure 2.5b). Peak cell shortening under endocardial flux-clamp was within the experimentally reported variation for this value (not shown).

Shortening simulated using the base myofilament model parameter set in response to epicardial flux-clamp did not show good agreement with experimental values of time to peak and RT90 (Figure 2.5b). Time to peak shortening and RT90 were both slower than experimental means by 38 and 101 ms , respectively. These results were strongly suggestive of an underlying difference in myofilament properties between epicardial cells and the other two cell subtypes.

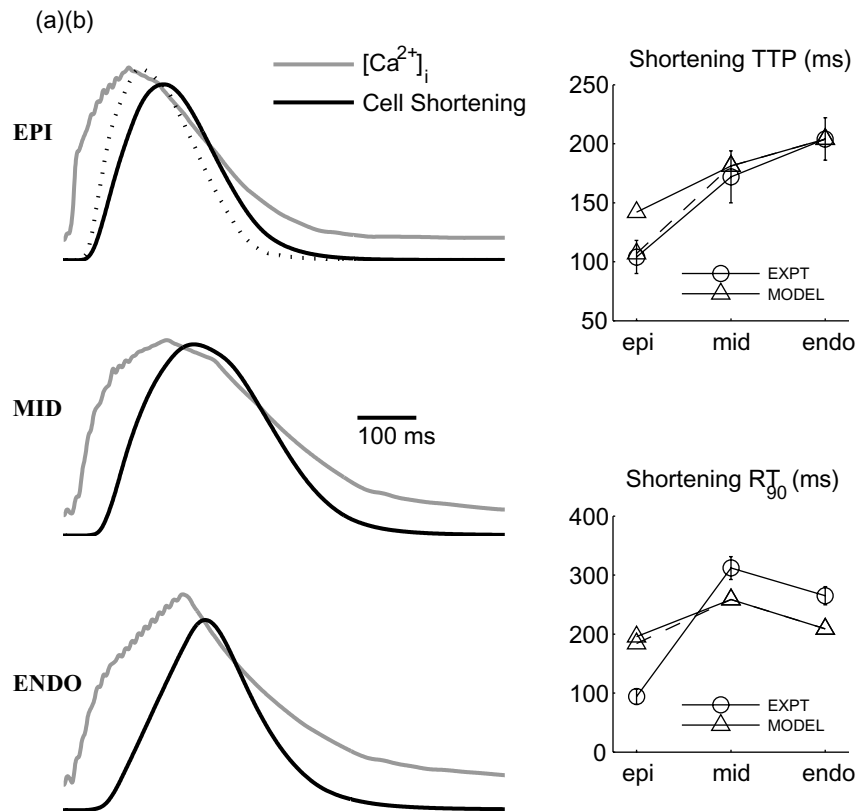


Figure 2.5: Simulated unloaded shortening for epi-, mid-, and endocardial cells in response to measured Ca^{2+} transients corrected via flux-clamp protocol. (a) Time course comparison of $[Ca^{2+}]_i$ (shaded traces) and resulting cell shortening (solid traces) in each of the three cell types. Dotted trace shows shortening after an increase in crossbridge cycling rate consistent with expression of the V1 myosin isoform (see text for details). (b) Comparison of simulated shortening TTP and RT_{90} (triangles) with mean values reported by Cordeiro *et al.* [15] (circles) for the three cell types. The dashed lines leading to triangles were determined from the dotted trace in (a) and once again represent the effect of increased crossbridge cycling rates.

2.3.7 Testing hypothesized myofilament heterogeneities

We considered and quantitatively tested several different hypotheses regarding changes to the myofilaments that might reconcile the discrepancies in Ca^{2+} -contraction dynamics between the model and experimental measurements in epicardial cells. As many of the proposed changes affected myofilament Ca^{2+} sensitivity, the flux-clamp protocol had to be repeated for each one in order to fit a new driving flux. Figure 6 shows the difference between model and experiment values of shortening time to peak and RT90 for each hypothesis tested in comparison to the original parameter set (abbreviated BASE in Figure 6). We tested the potential effects of transmural variation in myosin isoform expression (suggested by Cordeiro *et al.* [15]) by changing the crossbridge kinetic rates in the myofilament model to those described by Rice *et al.* [37] as corresponding to the faster V1 myosin isoenzyme (V1 in Figure 6). Passive cell stiffness was increased (TITIN in Figure 6), consistent with increased expression of the stiffer N2B titin isoform observed in the canine epicardium [19]. We hypothesized that phosphorylation of myosin binding protein C, which is thought to increase crossbridge attachment rate [50], could be altered in epicardial cells (MyBPC in Figure 6). We also tested the sensitivity of the model to increased myofilament Ca^{2+} sensitivity (SENS), increased myofilament cooperativity (COOP), and a combination of increased titin-based stiffness with steeper cooperative activation (TITIN+COOP). The myofilament model parameter sets used to represent each of these hypotheses are given in Appendix A.

Of all the hypotheses tested in the model, none was able to completely account for differences between the epicardial cell model and experimentally reported values (Figure 6). The V1 and COOP parameter sets reduced RT90 below that shown by the base model, but not significantly. Overall, relaxation of shortening in the model was not sensitive to any of the parameters changed in this process. Time to peak shortening was reduced to some extent by all but the SENS parameter set, which increased time to peak. Time to peak was most sensitive to the V1 parameter set, which brought this value to within the experimentally observed variation (Figure 2.5a, dotted trace, Figure 2.5b, dashed line and triangle).

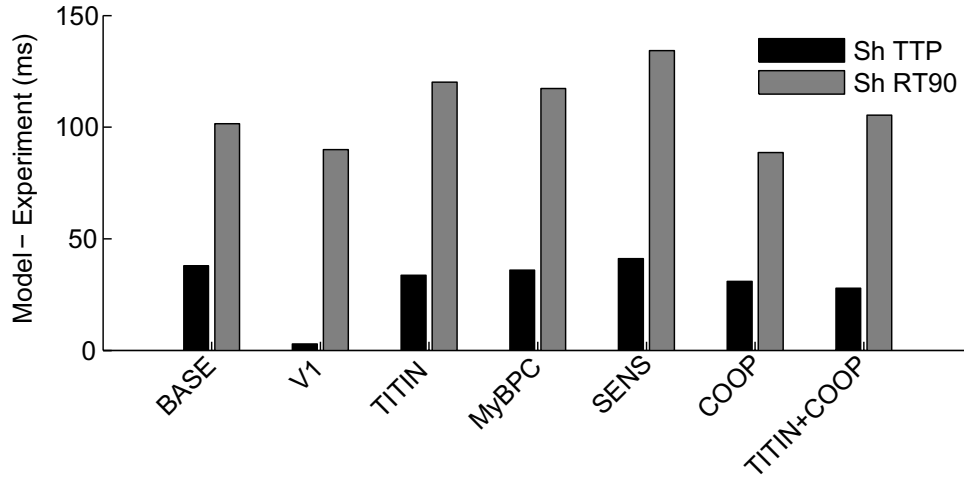


Figure 2.6: Testing of hypothesized mechanisms of altered Ca^{2+} -contraction coupling in epicardial myocytes. Description of the hypothesis represented by each abbreviation is presented in the text. Other abbreviations as in Figure 2.2.

2.4 Discussion

The present work suggests that much of the mechanical heterogeneity observed by Cordeiro *et al.* [15] in canine myocytes may be explained by previously identified and modelled differences in EC coupling and clarifies the mechanisms by which this control is likely to operate. We have presented evidence that where heterogeneity of Ca^{2+} transients do not completely explain differences in shortening, a specific alteration in myofilament protein expression reconciles experimental and modelling results.

2.4.1 Modulation of contractile dynamics by early repolarisation and I_{to1}

Cordeiro *et al.* [15] reported significantly prolonged time between stimulus and the onset of unloaded cell shortening in endocardial cells in comparison with mid- and epicardial cells. In the coupled model, this was the result of a large

difference in the slope of the rising phase of the Ca^{2+} transient. Early repolarisation of the AP was seen as the primary modulator of this aspect of Ca^{2+} morphology (see Figure 2.3). As I_{to1} magnitude determines distinctions in early repolarisation [11], we conclude that it ultimately controls contraction latency to a large extent.

The process by which I_{to1} changes time course of contraction is mechanically explained by the electromechanics model. The slowed rate of early repolarisation under endocardial AP clamp allows less extracellular Ca^{2+} into the dyadic subspace, and results in only a small amount of Ca^{2+} release through the RyRs. However, a lower concentration of Ca^{2+} in the dyadic subspace causes Ca^{2+} -dependent inactivation of L-type Ca^{2+} channels to proceed at a slower rate, prolonging the secondary phase of I_{CaL} relative to that seen under epicardial AP clamp. The sustained nature of this phase causes enough SR Ca^{2+} release to generate a cytosolic transient that is delayed but still of significant amplitude. A similar relationship between the rate of early repolarisation and Ca^{2+} transient shape has been seen experimentally [51].

Given the steep force- Ca^{2+} relation of cardiac muscle, it seems counterintuitive that the magnitudes of shortening between the two AP clamp cases would be closer than those of their respective Ca^{2+} transients. Simulations using realistic myofilament cooperativity reveal that the extent of unloaded shortening is strongly affected by the shape of the Ca^{2+} transient, not just the absolute magnitude (Figure 2.3, *b* and *c*). Cooperative recruitment of force slows the rate of force development at sub-maximal levels of myofilament activation [52], meaning that rapidly-peaking Ca^{2+} transients allow less time for the system to reach maximal force than their slower counterparts. Steep cooperativity of myofilament force production may therefore function as a mechanism to preserve contractile function in endocardial cells in the absence of I_{to1} . Similarly, Ca^{2+} transient morphology may explain why endocardial cells showed slightly larger peak unloaded shortening than the other cell types in spite of no significant difference in Ca^{2+} transient amplitude (Cordeiro *et al.* 2004).

2.4.2 Transmural heterogeneity of myofilament protein expression

Flux-clamp simulations suggested that mid- and epicardial cells could not share the same Ca^{2+} -contraction dynamics. Increased SR Ca^{2+} content observed in epicardial cells (Cordeiro *et al.* 2004), likely due to increased SERCA expression [10], may be responsible for faster time to peak of the Ca^{2+} transient compared with midmyocardial cells. Increased SERCA also has the effect of speeding decay and (to a lesser extent) the time to peak of the Ca^{2+} transient. Yet the combined effects of I_{to1} , increased SR content, and increased SR reuptake of Ca^{2+} , manifest in the experimentally measured epicardial Ca^{2+} transient, appear to be insufficient to account for the observed increase in contraction speed. We showed using the model that increasing crossbridge kinetics in a manner consistent with increased expression of the faster V1 isoform of myosin produces a relation between time course of free Ca^{2+} and time to peak shortening that agreed well with experiments. This change alone was the most effective compared with several alternative hypotheses and suggests a transmural gradient in the expression ratio of V1 to V3 myosin, with V1 expression highest at the epicardium. Although no study of which we are aware has examined transmural gradients of myosin isoform expression in canine, others have been performed in rat [53], rabbit [54], and most recently in pig [55]. These studies universally report higher expression of V1 myosin on the epicardium than endocardium, supporting our hypothesis.

We were unable to find a parameter set for the myofilament model of Rice, *et al.* [37] that would completely describe the epicardial myocyte Ca^{2+} -contraction dynamics reported experimentally [15]. While speeding the crossbridge cycling rate allowed the model to correctly predict time to peak shortening, relaxation still proceeded at too slow a rate. Indeed, none of the parameter modifications we attempted were able to account for the faster relaxation rate reported experimentally for epicardial cells. This is not a general failure of the model, as the relaxation- Ca^{2+} relation is apparently well reproduced in mid- and endocardial cells. Instead, this points to the absence of some mechanism not included in the model whereby faster crossbridge cycling influences deactivation of the thin fila-

ment.

2.4.3 Insights from tight coupling between EP and myofilament models

Modelling of cardiac EC coupling has usually stopped short of including contraction. Models and experiments have already examined the relationship between early repolarisation (primarily via I_{to1}) and the Ca^{2+} transient [26, 51]. These studies have emphasised the adverse effects on contraction of reduced I_{to1} seen in the diseased myocardium. However, it is clear that heterogeneous I_{to1} expression is present in the normal heart with little effect on the strength of contraction [15]. The electromechanics model suggests that several mechanisms working together can compensate for lower initial I_{CaL} in endocardial cells to preserve contractile function. Coupling of the EP and myofilament models allowed us to elucidate this subtle behaviour.

The majority of models of myocyte EC coupling assume a constant affinity of TnC for Ca^{2+} , while experiments suggest that thin filament activation and crossbridge binding alter TnC buffering capacity [56]. Because of the steep cooperative regulation of crossbridge binding by Ca^{2+} , the buffering capacity of the myofilament system may also be viewed as cooperative, undergoing large time- and Ca^{2+} -dependent shifts within a single cardiac cycle. In the coupled electromechanics model, this dynamic buffering shortened APD relative to the original EC coupling model with static TnC buffering by reducing the buffering capacity of the myofilaments during the diastolic interval and allowing more rapid decline of $[Ca^{2+}]_i$ via SR uptake and extrusion through other mechanisms. Dynamic buffering of Ca^{2+} by the myofilaments played an especially important role in the flux-clamp protocol we designed to estimate the Ca^{2+} transient after removal of the fluorescent indicator. In the absence of the exogenous buffer, the myofilament buffering capacity adjusted itself in a complex nonlinear manner resulting in changes to Ca^{2+} transient morphology.

Most models of myofilament force production are tested using a clamped Ca^{2+} transient based on the time course of fluorescent indicators. We used the

electromechanics model to show that such indicators can cause large errors in Ca^{2+} transient shape. Thus aspects of the EP/ Ca^{2+} -handling model allowed us to make greater quantitative use of the myofilament model. In summary, including tightly-coupled models of all three subsystems improved the quality of all models involved.

2.4.4 Limitations

The models presented here have several limitations. The published models that form the components of the present model each contain limitations of their own [25, 26, 37]. The most important of these is the strong cycle-length dependence of Ca^{2+} transient time to peak in the Greenstein model (see Figure 6b, Greenstein *et al.* [26]), especially when using the parameter sets for mid- and epicardial cells presented by Flaim *et al.* [25]. This dependence caused the electromechanics model to produce qualitatively different Ca^{2+} transients than those reported experimentally when run at a matching cycle length of 2000 ms. This discrepancy did not affect the utility of the model in elucidating the modulation of contraction time course by I_{to1} , but did limit the ability of the model to identify potential heterogeneities of myofilament properties. This shortcoming was effectively overcome via the flux-clamp simulations, which allowed the prediction of shortening directly from experimentally reported Ca^{2+} transients.

We did not fully explore the effects of increased SERCA and higher SR Ca^{2+} load reported in canine epicardial cells [10, 15]. The model of Flaim *et al.* [25] exhibits a higher SR Ca^{2+} load in epicardial cells relative to the other types at a cycle length of 1000 ms, which is consistent with experimental results. However, the electromechanics model at slower cycle lengths produced only a moderately elevated SR load, once again indicating an incorrect frequency dependence of Ca^{2+} -handling. The result achieved in the model of Flaim *et al.* [25] came by doubling the activity of SERCA relative to the other cell types to reflect experimental reports of much higher SERCA expression in epicardial cells. When this hypothesis was implemented in similar fashion in the flux clamp protocol, it resulted in unreasonable responses after withdrawal of fluo-3. As a result we

left SERCA parameters unchanged during epicardial cell flux-clamp and allowed any additional uptake of Ca^{2+} by SERCA present in these cells to be implicitly incorporated into the driving flux during the fitting process.

The flux clamp protocol involves several assumptions. The cytosolic concentration of fluo-3 is assumed to be equal to that reported for the bathing solution, and may not reflect the actual value. Furthermore, Ca^{2+} binding kinetics for fluo-3 were taken from experiments performed in vitro [57] and may not represent kinetics within an intact myocyte. Flux clamp was developed on the assumption that most cytosolic Ca^{2+} fluxes would not be strongly affected by withdrawing fluo-3 and that the Ca^{2+} dependence of myofilament buffering and SERCA activity were adequately described by their respective model representations. This series of assumptions seems reasonable, however, as through the use of the flux clamp protocol a set of myofilament parameters was determined that was able to describe the Ca^{2+} -contraction dynamics of both mid- and endocardial cells. Furthermore, this parameter set displayed a steady-state force- Ca^{2+} relation similar to those reported experimentally in isolated canine myocytes [58].

2.4.5 Conclusion

We have used an integrative model of ventricular myocyte function that includes electrophysiology, Ca^{2+} -handling, and myofilament dynamics to explore potential mechanisms by which myocytes within the same heart modulate their EC coupling characteristics. Our work identifies I_{tot} and crossbridge cycling kinetics as primary mechanisms underlying transmural variation of myocyte contractile function.

Acknowledgements

We gratefully acknowledge the generosity of Dr. Jeremy Rice and Jason Yang in providing the original code for the myofilament model. We also wish to thank Drs. Roy Kerckhoffs, Jeffrey Omens, and Jonathan Cordeiro for helpful discussion and other assistance during this study. This work was supported by

NSF Grant BES-0506252, the National Biomedical Computation Resource (NIH Grant RR08605), UC Discovery Grant 1T106-10159, Medtronic Inc., and Howard Hughes Medical Institute Interfaces Training Grant HHMI-56005681 (all to A. D. M.) and EPSRC Grant EP/D065666/1 (to S. N. F.).

Chapter 2, in full, is a reprint of the published article “Mechanisms of transmurally-varying myocyte electromechanics in an integrated computational model.” Campbell S.G., Flaim S.N., Leem C.H., and McCulloch A.D. *Philosophical Transactions of the Royal Society A*, 366:3361-3380, 2008. The dissertation author was the primary investigator and author of this paper.

References

- [1] Waldman, L.K., Nosan, D., Villarreal, F., and Covell, J.W., 1988. Relation between transmural deformation and local myofiber direction in canine left ventricle. *Circulation Research*, 63:550–62.
- [2] Costa, K.D., Takayama, Y., McCulloch, A.D., and Covell, J.W., 1999. Laminar fiber architecture and three-dimensional systolic mechanics in canine ventricular myocardium. *Am J Physiol*, 276:H595–607.
- [3] Mazhari, R., Omens, J.H., Pavelec, R.S., Covell, J.W., and McCulloch, A.D., 2001. Transmural distribution of three-dimensional systolic strains in stunned myocardium. *Circulation*, 104:336–41.
- [4] Tseng, W.Y., Reese, T.G., Weisskoff, R.M., Brady, T.J., and Wedeen, V.J., 2000. Myocardial fiber shortening in humans: initial results of MR imaging. *Radiology*, 216:128–39.
- [5] Arts, T., Prinzen, F.W., Snoeckx, L.H., Rijcken, J.M., and Reneman, R.S., 1994. Adaptation of cardiac structure by mechanical feedback in the environment of the cell: a model study. *Biophys J*, 66:953–61.
- [6] Ashikaga, H., Criscione, J.C., Omens, J.H., Covell, J.W., and Ingels, N.B., 2004. Transmural left ventricular mechanics underlying torsional recoil during relaxation. *Am J Physiol Heart Circ Physiol*, 286:H640–7.
- [7] Ashikaga, H., Coppola, B.A., Hopenfeld, B., Leifer, E.S., McVeigh, E.R., and Omens, J.H., 2007. Transmural dispersion of myofiber mechanics: implications for electrical heterogeneity in vivo. *J Am Coll Cardiol*, 49:909–16.

- [8] Wolk, R., Cobbe, S.M., Hicks, M.N., and Kane, K.A., 1999. Functional, structural, and dynamic basis of electrical heterogeneity in healthy and diseased cardiac muscle: implications for arrhythmogenesis and anti-arrhythmic drug therapy. *Pharmacol Ther*, 84:207–31.
- [9] Liu, D.W., Gintant, G.A., and Antzelevitch, C., 1993. Ionic bases for electrophysiological distinctions among epicardial, midmyocardial, and endocardial myocytes from the free wall of the canine left ventricle. *Circulation Research*, 72:671–87.
- [10] Laurita, K.R., Katta, R., Wible, B., Wan, X., and Koo, M.H., 2003. Transmural heterogeneity of calcium handling in canine. *Circ Res*, 92:668–75.
- [11] Litovsky, S.H. and Antzelevitch, C., 1988. Transient outward current prominent in canine ventricular epicardium but not endocardium. *Circulation Research*, 62:116–26.
- [12] Rosati, B., Grau, F., Rodriguez, S., Li, H., Nerbonne, J.M., and McKinnon, D., 2003. Concordant expression of KChIP2 mRNA, protein and transient outward current throughout the canine ventricle. *J Physiol (Lond)*, 548:815–22.
- [13] Wang, H.S. and Cohen, I.S., 2003. Calcium channel heterogeneity in canine left ventricular myocytes. *J Physiol (Lond)*, 547:825–33.
- [14] Bányász, T., Fülöp, L., Magyar, J., Szentandrassy, N., Varró, A., and Nánási, P.P., 2003. Endocardial versus epicardial differences in L-type calcium current in canine ventricular myocytes studied by action potential voltage clamp. *Cardiovasc Res*, 58:66–75.
- [15] Cordeiro, J., Greene, L., Heilmann, C., Antzelevitch, D., and Antzelevitch, C., 2004. Transmural heterogeneity of calcium activity and mechanical function in the canine left ventricle. *Am J Physiol Heart Circ Physiol*, 286:H1471–9.
- [16] Li, G.R., Lau, C.P., Ducharme, A., Tardif, J.C., and Nattel, S., 2002. Transmural action potential and ionic current remodeling in ventricles of failing canine hearts. *Am J Physiol Heart Circ Physiol*, 283:H1031–41.
- [17] Cazorla, O., Szilagyi, S., Guennec, J.Y.L., Vassort, G., and Lacampagne, A., 2005. Transmural stretch-dependent regulation of contractile properties in rat heart and its alteration after myocardial infarction. *The FASEB Journal*, 19:88–90.
- [18] Cazorla, O., Freiburg, A., Helmes, M., Centner, T., McNabb, M., Wu, Y., Trombitás, K., Labeit, S., and Granzier, H., 2000. Differential expression of cardiac titin isoforms and modulation of cellular stiffness. *Circulation research*, 86:59–67.

- [19] Bell, S.P., Nyland, L., Tischler, M.D., McNabb, M., Granzier, H., and LeWinter, M.M., 2000. Alterations in the determinants of diastolic suction during pacing tachycardia. *Circ Res*, 87:235–40.
- [20] Cazorla, O., Guennec, J.Y.L., and White, E., 2000. Length-tension relationships of sub-epicardial and sub-endocardial single ventricular myocytes from rat and ferret hearts. *Journal of molecular and cellular cardiology*, 32:735–44.
- [21] Wan, X., Bryant, S.M., and Hart, G., 2003. A topographical study of mechanical and electrical properties of single myocytes isolated from normal guinea-pig ventricular muscle. *J Anat*, 202:525–36.
- [22] Viswanathan, P.C., Shaw, R.M., and Rudy, Y., 1999. Effects of IKr and IKs heterogeneity on action potential duration and its rate dependence: a simulation study. *Circulation*, 99:2466–74.
- [23] Solovyova, O., Vikulova, N., and Katsnelson, L., 2003. Mechanical Interaction of Heterogeneous Cardiac Muscle Segments In Silico: Effects on Ca²⁺ Handling and Action Potential. *Internat J Bifurcation Chaos*, 13:3757–3782.
- [24] Saucerman, J.J., Healy, S.N., Belik, M.E., Puglisi, J.L., and McCulloch, A.D., 2004. Proarrhythmic consequences of a KCNQ1 AKAP-binding domain mutation: computational models of whole cells and heterogeneous tissue. *Circulation Research*, 95:1216–24.
- [25] Flaim, S.N., Giles, W.R., and McCulloch, A.D., 2006. Contributions of sustained I_{Na} and I_{Kv43} to transmural heterogeneity of early repolarization and arrhythmogenesis in canine left ventricular myocytes. *Am J Physiol Heart Circ Physiol*, 291:H2617–29.
- [26] Greenstein, J., Hinch, R., and Winslow, R., 2006. Mechanisms of excitation-contraction coupling in an integrative model of the cardiac ventricular myocyte. *Biophys J*, 90:77–91.
- [27] Noble, D. and Rudy, Y., 2001. Models of cardiac ventricular action potentials: iterative interaction between experiment and simulation. *Phil Trans R Soc A*, 359:1127–1142.
- [28] Irvine, L.A., Jafri, M.S., and Winslow, R.L., 1999. Cardiac sodium channel Markov model with temperature dependence and recovery from inactivation. *Biophys J*, 76:1868–85.
- [29] Clancy, C.E. and Rudy, Y., 1999. Linking a genetic defect to its cellular phenotype in a cardiac arrhythmia. *Nature*, 400:566–9.
- [30] Rice, J. and Jafri, M., 2001. Modelling calcium handling in cardiac cells. *Phil Trans R Soc Lond A*, 359:1143–1157.

- [31] Greenstein, J.L. and Winslow, R.L., 2002. An integrative model of the cardiac ventricular myocyte incorporating local control of Ca^{2+} release. *Biophys J*, 83:2918–45.
- [32] Hinch, R., Greenstein, J.L., Tanskanen, A.J., Xu, L., and Winslow, R.L., 2004. A simplified local control model of calcium-induced calcium release in cardiac ventricular myocytes. *Biophys J*, 87:3723–36.
- [33] Rice, J.J. and de Tombe, P.P., 2004. Approaches to modeling crossbridges and calcium-dependent activation in cardiac muscle. *Prog Biophys Mol Biol*, 85:179–95.
- [34] Landesberg, A., Livshitz, L., and ter Keurs, H.E., 2000. The effect of sarcomere shortening velocity on force generation, analysis, and verification of models for crossbridge dynamics. *Ann Biomed Eng*, 28:968–78.
- [35] Solovyova, O., Katsnelson, L., Guriev, S., Nikitina, L., Protsenko, Y., Routkevitch, S., and Markhasin, V., 2002. Mechanical inhomogeneity of myocardium studied in parallel and serial cardiac muscle duplexes: experiments and models. *Chaos, Solitons & Fractals*, 13:1685–1711.
- [36] Niederer, S.A., Hunter, P.J., and Smith, N.P., 2006. A quantitative analysis of cardiac myocyte relaxation: a simulation study. *Biophysical Journal*, 90:1697–722.
- [37] Rice, J., Wang, F., Bers, D., and TOMBE, P.D., 2008. Approximate model of cooperative activation and crossbridge cycling in cardiac muscle using ordinary differential equations. *Biophysical Journal*, 95:2368–90.
- [38] Rice, J.J., Jafri, M.S., and Winslow, R.L., 2000. Modeling short-term interval-force relations in cardiac muscle. *Am J Physiol Heart Circ Physiol*, 278:H913–31.
- [39] Matsuoka, S., Sarai, N., Kuratomi, S., Ono, K., and Noma, A., 2003. Role of individual ionic current systems in ventricular cells hypothesized by a model study. *Jpn J Physiol*, 53:105–23.
- [40] Iribe, G., Kohl, P., and Noble, D., 2006. Modulatory effect of calmodulin-dependent kinase II (CaMKII) on sarcoplasmic reticulum Ca^{2+} handling and interval-force relations: a modelling study. *Philos Transact A Math Phys Eng Sci*, 364:1107–33.
- [41] Kohl, P. and Sachs, F., 2001. Mechanoelectric feedback in cardiac cells. *Phil Trans R Soc Lond A*, 359:1173–1185.

- [42] Nickerson, D., Niederer, S., Stevens, C., Nash, M., and Hunter, P., 2006. A computational model of cardiac electromechanics. *Conf Proc IEEE Eng Med Biol Soc*, 1:5311–4.
- [43] Kohl, P., Day, K., and Noble, D., 1998. Cellular mechanisms of cardiac mechano-electric feedback in a mathematical model. *Can J Cardiol*, 14:111–9.
- [44] Solovyova, O., Vikulova, N., Konovalov, P., Kohl, P., and Markhasin, V., 2004. Mathematical modelling of mechano-electric feedback in cardiomyocytes. *Russ J Numer Anal M*, 19:331–351.
- [45] Bluhm, W.F., Lew, W.Y., Garfinkel, A., and McCulloch, A.D., 1998. Mechanisms of length history-dependent tension in an ionic model of the cardiac myocyte. *Am J Physiol*, 274:H1032–40.
- [46] Niederer, S.A. and Smith, N.P., 2007. A mathematical model of the slow force response to stretch in rat ventricular myocytes. *Biophysical Journal*, 92:4030–44.
- [47] Cortassa, S., Aon, M.A., O'Rourke, B., Jacques, R., Tseng, H.J., Marbán, E., and Winslow, R.L., 2006. A computational model integrating electrophysiology, contraction, and mitochondrial bioenergetics in the ventricular myocyte. *Biophys J*, 91:1564–89.
- [48] Crampin, E.J. and Smith, N.P., 2006. A dynamic model of excitation-contraction coupling during acidosis in cardiac ventricular myocytes. *Biophys J*, 90:3074–90.
- [49] Sipido, K.R. and Wier, W.G., 1991. Flux of Ca^{2+} across the sarcoplasmic reticulum of guinea-pig cardiac cells during excitation-contraction coupling. *J Physiol (Lond)*, 435:605–30.
- [50] Stelzer, J.E., Dunning, S.B., and Moss, R.L., 2006. Ablation of cardiac myosin-binding protein-C accelerates stretch activation in murine skinned myocardium. *Circulation Research*, 98:1212–8.
- [51] Sah, R., Ramirez, R.J., and Backx, P.H., 2002. Modulation of Ca^{2+} release in cardiac myocytes by changes in repolarization rate: role of phase-1 action potential repolarization in excitation-contraction coupling. *Circulation Research*, 90:165–73.
- [52] Campbell, K., 1997. Rate constant of muscle force redevelopment reflects cooperative activation as well as cross-bridge kinetics. *Biophys J*, 72:254–62.
- [53] Carnes, C.A., Geisbuhler, T.P., and Reiser, P.J., 2004. Age-dependent changes in contraction and regional myocardial myosin heavy chain isoform expression in rats. *J Appl Physiol*, 97:446–53.

- [54] Litten, R.Z., Martin, B.J., Buchthal, R.H., Nagai, R., Low, R.B., and Alpert, N.R., 1985. Heterogeneity of myosin isozyme content of rabbit heart. *Circulation Research*, 57:406–14.
- [55] Stelzer, J.E., Norman, H.S., Chen, P.P., Patel, J.R., and Moss, R.L., 2008. Transmural variation in myosin heavy chain isoform expression modulates the timing of myocardial force generation in porcine left ventricle. *J Physiol (Lond)*, 586:5203–14.
- [56] Davis, J.P., Norman, C., Kobayashi, T., Solaro, R.J., Swartz, D.R., and Tikunova, S.B., 2007. Effects of thin and thick filament proteins on calcium binding and exchange with cardiac troponin C. *Biophys J*, 92:3195–206.
- [57] Naraghi, M., 1997. T-jump study of calcium binding kinetics of calcium chelators. *Cell Calcium*, 22:255–68.
- [58] Wolff, M.R., Whitesell, L.F., and Moss, R.L., 1995. Calcium sensitivity of isometric tension is increased in canine experimental heart failure. *Circulation Research*, 76:781–9.

Chapter 3

A Model of Heterogeneous Ventricular Electromechanics

Abstract

The excitation-contraction coupling properties of cardiac myocytes isolated from different regions of the mammalian left ventricular wall have been shown to vary considerably, with uncertain effects on ventricular function. We embedded a cell-level excitation-contraction coupling model with region-dependent parameters within a simple finite element model of left ventricular geometry to study effects of electromechanical heterogeneity on local myocardial mechanics and global hemodynamics. This model was compared with one in which heterogeneous myocyte parameters were assigned randomly throughout the mesh while preserving the total amount of each cell subtype. The two models displayed nearly identical transmural patterns of fibre and cross-fibre strains at end systole, but showed clear differences in fibre strains at earlier points during systole. Hemodynamic function, including peak left ventricular pressure, maximum rate of left ventricular pressure development, and stroke volume were essentially identical in the two models. These results suggest that in the intact ventricle heterogeneously distributed myocyte subtypes primarily impact local deformation of the myocardium, and that these effects are greatest during early systole.

3.1 Introduction

In the most basic sense, electromechanical coupling occurs at the level of the individual myocyte where changes to membrane potential lead to release of Ca^{2+} and production of force by the myofilaments. This intrinsic activity is modulated by surrounding myocytes. Ionic currents through gap junctions electrically couple adjacent cells, allowing propagation of action potentials through the myocardium. Mechanical coupling among myocytes arises from cytoskeletal structures linking myocardial cells to each other and to the extracellular matrix. Thus, in a broader sense, electromechanics includes electrical and structural properties of the intact myocardium as these influence the local environment in which myocytes operate.

Regional deformation of the ventricular wall during the cardiac cycle is influenced by myocardial tissue structure [1–3]. Early modeling studies suggested that ventricular torsion and transmural patterns of fibre orientation act to minimize transmural differences in sarcomere length and fibre strain, both during ejection [1] and filling [4], thereby distributing the work of ejection equally through the heart wall [1, 2]. Studies using biplane radiography of radiopaque markers embedded in the ventricular wall [5, 6] as well as MRI tagging methods [7] showed patterns of transmural fiber strain that were in general agreement with those predicted in models.

In recent years, computational and experimental studies have revealed a more complex scenario. Kerckhoffs *et al.* [8] showed using a computational model of LV electromechanics that a physiological pattern of electrical activation produced large gradients of transmural fibre strain in comparison with a synchronously activated model. The authors postulated that a transmural gradient of intrinsic myocyte electromechanical delay opposing that of electrical activation would reduce transmural heterogeneity of systolic fibre strain. Shortly thereafter, a study of isolated canine myocytes demonstrated the existence of just such a transmural distribution, with endocardial myocytes (those earliest activated in the intact heart) showing increased latency to onset of shortening in comparison with midmyocardial and epicardial cells [9]. At the same time, improved spatial and temporal

resolution in the measurement of fibre strains have revealed transmural heterogeneity in the time courses of regional fibre strains during systole [10, 11]. These new results do not invalidate the overall hypothesis that realistic LV torsion and fibre orientation act to reduce transmural variation of fibre strain. But, they illustrate the need for more detailed examination of the mechanisms underlying observed transmural deformations during systole.

3.1.1 Models of Ventricular Electromechanics

The most advanced models of ventricular electromechanics depict three-dimensional action potential propagation, contractile force generation, and myocardial deformation under realistic hemodynamic loading conditions and within anatomically-detailed finite element meshes [8, 12–19]. The degree of coupling between component models varies, but newer studies have made use of algorithmic advances which allow full (two-way) coupling between and quasi-simultaneous solution of action potential propagation, ionic currents, myofilament force production, and tissue mechanics [16–19]. This form of coupling is useful for investigating questions relating to mechano-electric feedback [20, 21], where length changes on the level of myocytes influence Ca^{2+} buffering by myofilaments and the activity of stretch activated ion channels. In many other cases, it has been sufficient to obtain a spatiotemporal sequence of depolarization from the solution of electrophysiology equations which can then be used to drive myofilament force production in a separate simulation of ventricular mechanics [8, 12, 13, 22, 23].

In recent years a number of fully-coupled cellular electromechanics models have been published. These models simulate various cell responses by simultaneously solving the ordinary differential equations (ODEs) governing ionic currents, myofilament force production, and one-dimensional cell mechanics [21, 24]. We recently developed one such model to explore potential sources of heterogeneous excitation-contraction (EC) coupling behavior previously observed in isolated canine myocytes [25]. Here, we use this model to examine the effects of heterogeneous myocyte properties [9, 26, 27] on transmural systolic fibre mechanics and ventricular function. In particular, we investigate the hypothesis of Kerckhoffs *et al.*

[8] that cellular heterogeneity of myocyte EC coupling helps maintain transmural uniformity of systolic fibre strain in the presence of a physiological activation delay.

3.2 Methods

In the present study, we embedded our recently published canine myocyte model [25] within a model of ventricular action potential propagation and mechanics. This fully-coupled electromechanical model was used to predict the integrative effects of myocyte EC coupling heterogeneity on ventricular wall mechanics and global pump function during ejection.

3.2.1 Model of myocyte excitation-contraction coupling

A model of canine myocyte ionic currents and cytosolic Ca^{2+} cycling [28] was previously expanded and modified to reproduce observed transmurally-varying characteristics in action potential duration, early repolarization, and Ca^{2+} transient time course [29]. Three parameter sets for the model were developed corresponding to published measurements in endocardial (endo), midmyocardial (mid), and epicardial (epi) cells. In previous work [25], we developed parameter sets for the myofilament model of Rice *et al.* [24], which quantitatively reproduced observed characteristics of unloaded shortening in the three canine myocyte subtypes driven by experimentally-derived Ca^{2+} transients [9]. In that same study, we combined this re-parameterized version of the Rice model with the excitation- Ca^{2+} coupling model of Flaim *et al.* [29] to create a fully-coupled model of canine myocyte electromechanics [25]. The Rice model itself uses a system of coupled ODEs to reproduce the dynamic response of cardiac muscle to time-varying inputs of sarcomere length and cytosolic Ca^{2+} . The model is capable of reproducing a variety of classical responses such as steep activation of force by Ca^{2+} and a realistic force-velocity relation. Length dependent activation is represented by a model of thick and thin filament overlap according to the classic work of Gordon *et al.* [30]. Velocity dependence is imparted through crossbridge distortion, whereby changes to sarcomere length alter average distortion of a population of cycling crossbridges

[31].

In the present work, we have embedded the fully-coupled myocyte electromechanics model with region-dependent parameters within a model of LV electrical activation and mechanics. Instances of the myocyte model located at each collocation point throughout the mesh take as inputs membrane potential, sarcomere length, and shortening velocity which originate from solutions to the corresponding monodomain and finite deformation partial differential equations. The myocyte model provides as outputs its contribution to changes in membrane potential and active tension. Initial conditions for myocyte electromechanical model were determined by running it independently of the ventricular model under conditions of unloaded shortening [24] for 50 beats, at which point model responses had achieved steady-state. Pacing rate was 1 Hz.

3.2.2 Coupling of velocity-dependent contraction and finite-element biomechanics models

Multi-scale models such as that used in the present study present an inherent challenge in that several time scales have to be taken under consideration. Stable numerical methods for coupling the various model components under mixed time-stepping schemes are critical for computational efficiency [17, 19]. Niederer and coworkers [19] recently developed a scheme which allows stable and efficient coupling of velocity-dependent contraction models and finite-element mechanics. In this 'update' scheme, the contraction model outputs an activation value each coarse time step rather than the final active tension. The mechanics solver then uses the activation value to re-compute a length- and velocity-dependent tension with each intermediate Newton iteration until the solution converges and the coarse time step is complete.

We have modified the update scheme of Niederer *et al.* [19] to function with the Rice contraction model [24], which is embedded within the myocyte electromechanics model. Instead of a generic activation level, the entire vector of contraction-associated state variables is output from the myocyte model. ODEs upon which tension directly depends are then re-integrated over the coarse time

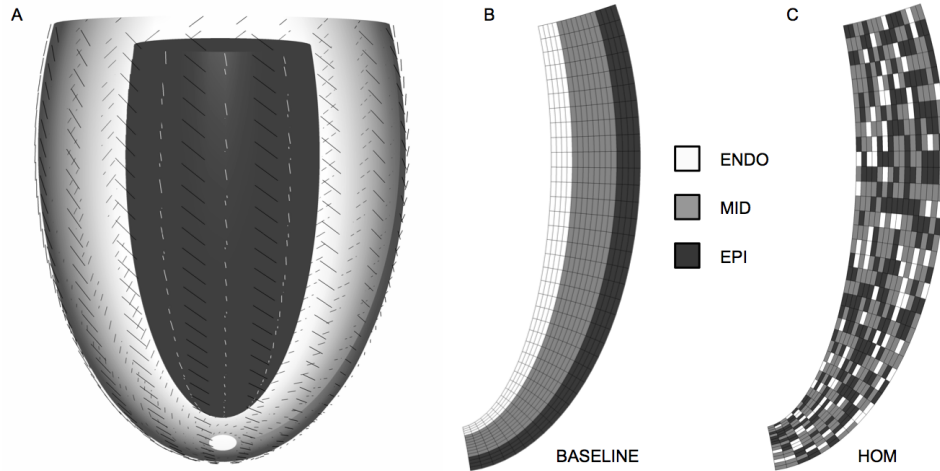


Figure 3.1: Depiction of finite element meshes and myocyte subtype distribution used in this study. (a) Left ventricular geometry was approximated as a truncated ellipse of revolution with embedded fibres. White and black lines show orientation of endocardial and epicardial fibres, respectively. (b) In the BASELINE simulation, myocyte subtype was set as a proportion of wall thickness to be 1:2:1 endo:mid:epi. Their spatial distribution is shown here superimposed on the two-dimensional mesh used for solution of electrical propagation across the ventricular wall. (c) In the HOM simulation, myocyte subtypes were assigned randomly throughout the mesh while preserving the total volume of each subtype to be equal that used in the BASELINE simulation.

step for each Newton iteration using an explicit Euler scheme. Sarcomere length and velocity are updated with every re-integration. This scheme stably accommodates relatively large mechanics time steps with minimal loss of accuracy. A coarse time step of 0.5 ms was used in all simulations. ODEs were solved on a finer time step with a Radau solver [32], using a maximum time step of 0.5 ms.

3.2.3 Finite Element model of myocardial deformation

Left ventricular (LV) geometry was approximated using a truncated ellipse of revolution [33]. At zero pressure, focal length was 3.75 cm [34], endocardial radial coordinate was 0.32, epicardial radial coordinate was 0.65, and longitudinal coordinate of the base was 120 degrees. This initial shape was subdivided 16 times radially and 36 times longitudinally to yield a 576 element mesh (Figure 3.1a).

Interpolating functions were linear in the circumferential, longitudinal, and radial directions, giving rise to a total of 1887 degrees of freedom [33]. The myocardium was modelled as a slightly-compressible, transversely isotropic material with respect to local fibre coordinates [4]. Fibre angles were varied transmurally in a piecewise-linear fashion determined by fit to angles measured in a previous study by our group [6]. As these fibre angles were not directly reported in the original publication, they have been included in Appendix B. Sarcomere length (SL) in the unloaded myocardium was assumed to vary transmurally according to detailed measurements in rat myocardium [35], and offset to a mean SL of 1.95 in accordance with published data from canine hearts [36, 37].

Boundary constraints were identical to those described in the original work of Costa *et al.* [33]. Nodes along the basal ($\mu = 120$ degrees) and apical ($\mu = 5$ degrees) boundaries were fixed in the longitudinal direction. The most epicardial node on the basal boundary was also constrained in the radial direction. Finally, the most endocardial of the basal nodes was fixed in the circumferential direction.

3.2.4 Finite Element model of electrical propagation

The monodomain equation for electrical propagation was solved using a collocation-Galerkin method along with an operator-splitting scheme to incorporate the myocyte electromechanics model [38, 39]. Electrical activation initiating contraction was assumed to occur simultaneously everywhere on the endocardial surface. Under this assumption, there are no circumferential gradients in membrane voltage. Accordingly, electrical propagation was solved on a two-dimensional mesh in rectangular Cartesian coordinates representing the cross-section of the mechanics mesh, with identical refinement (Figure 3.1, *b* and *c*). The voltage solution was interpolated using cubic Hermite basis functions, giving rise to a total of 5032 degrees of freedom. Transmural activation time and action potential duration were converged to within 1% at this level of refinement, based on comparison with an equivalent problem having twice as many (32) transmural elements. Error in the calculation of electrical propagation arising from the absence of circumferential curvature in the two-dimensional model was also assessed in preliminary calcula-

tions. Briefly, a three-dimensional wedge was created by extracting a 30-degree circumferential portion of the original ellipsoid mesh. This wedge was refined four times in the circumferential direction, and converted to rectangular Cartesian coordinates. Action potential propagation was simulated in two- and three-dimensional meshes (with inputs from the mechanics model held constant) and compared. Differences in transmural activation times between the two models were small ($<8\%$). The tissue conductivity coefficient was set at 2.4 mS cm^{-1} to give a transmural activation time of approximately 24 ms at the thickest part of the ventricular wall [40]. Geometry of the electrical mesh was updated every 4 ms in accordance with mechanical deformation induced by contraction.

3.2.5 Representation of heterogeneous cellular properties

In the complete ventricular model, the myocyte model parameter set (epi, mid, or endo) was specified in an element-wise fashion according to myocardial region (Figure 3.1*b*). For purposes of comparison, an alternate distribution of cell subtypes was created in which elements were assigned parameters randomly (Figure 3.1*c*). This was done in such a way that the overall ventricular volume corresponding to each cell subtype was identical between the two distributions.

3.2.6 Lumped-parameter circulatory model

A three-element Windkessel model was used to provide pressure boundary conditions at the endocardial surface of the finite element mesh using a previously-established coupling method [41]. A simplified system in which the Windkessel model was coupled to a time-varying elastance model was used to determine circulatory parameters which best fit averaged LV pressure and aortic flow traces measured in a set of dog experiments (experiments described below). The resulting model parameters are shown in Table 1. LV pressure from the ventricular model and arterial pressure computed from the circulatory model were used to determine timing of events in the cardiac cycle such as aortic valve opening and closure.

Table 3.1: Three-element Windkessel Model Parameters.

Initial aortic pressure	67.5 mmHg
Arterial compliance	0.67 cm ³ mmHg ⁻¹
Aortic impedance	52.5 mmHg ms cm ⁻¹
Peripheral resistance	3000 mmHg ms cm ⁻¹

3.2.7 Simulation protocol

The unloaded mesh was inflated to an end-diastolic pressure (EDP) of 3.9 mmHg in the absence of active myofilament tension, to correspond with the average end-diastolic pressure reported in the study of Mazhari *et al.* [6]. LV volume increased from 30.2 ml in the unloaded state to 38.4 ml at EDP. After inflation, a stimulus current was applied to the endocardial surface to initiate action potential propagation and contraction. All simulations made use of this same protocol unless otherwise noted.

End-diastolic geometry served as the reference for calculation of fibre strains throughout the cycle. All strains reported below reflect averages of strains in five longitudinally-consecutive elements at constant wall depth. Except where specifically noted, these groups of five elements corresponded to an apical region of the myocardium, centered about the prolate spheroidal coordinate of $\mu = 40$ degrees.

3.2.8 Experimentally-measured fibre strains

All animal studies were performed according to the National Institutes of Health Guide for the Care and Use of Laboratory Animals. Surgical protocols were approved by the Animal Subjects Committee of the University of California, San Diego, which is accredited by the American Association for Accreditation of Laboratory Animal Care.

Surgical Preparation. Six adult mongrel dogs (19-24 kg) were anesthetized with intravenous propofol (6mg/kg), intubated, and mechanically ventilated with isoflurane (0.5% - 2.5%), nitrous oxide (2 l/min), and medical oxygen (2 l/min) to maintain a surgical plane of anesthesia. Once data collection was complete, animals

were removed from respiratory support and euthanized with a lethal dose of propofol. Left ventricular pressure was measured with an 8-Fr pigtail micromanometer catheter with lumen (Millar Instruments, Houston, TX). End-diastole was defined as coinciding with peak of the R-wave of the electrocardiogram (ECG). A Doppler flow probe (model #T208, Transonic Systems, Ithaca, NY) was positioned around the ascending aorta to define the onset and conclusion of ejection.

In Vivo LV Mechanics. As described previously [10, 42], implanted radio-plaque marker positions were followed throughout the cardiac cycle. Three columns (4-6 beads) of gold (0.9 mm) beads were plunged into anterolateral wall to form a triad of material makers at 1/3 of the apex-base distance. Using a biplane X-ray system, cineradiographic images were acquired at sampling rate of 125 frames/sec with mechanical ventilation suspended at end expiration. LV and systemic pressures, aortic flow, and surface ECG were digitally acquired simultaneously with these images.

Myofibre Orientation. Local fibre architecture [34] in the region of the transmural bead set was determined [10]. Mean fibre angles, θ , were measured at 1 mm increments across the wall and interpolated with least-squared best-fit line. Finite 3D Deformation Analysis. Continuous, non-homogenous 3-D systolic strain distributions were determined in a local Cartesian cardiac coordinate system (X_1, X_2, X_3), defining the circumferential, longitudinal, and radial directions, respectively. Strain was computed with reference to the end-diastolic state in all cases. At each transmural depth the mean fibre angle, α , was used to rotate the cardiac strain tensor into fibre, cross-fibre, radial (X_f, X_{cf}, X_3) coordinate system [5]. Time courses of myofibre strain, E_{ff} , during successive cardiac contractions as well as transmural distributions at end-systole were obtained for each animal.

3.3 Results

Results from the baseline model, in which myocyte subtypes were heterogeneously arranged in layers (BASELINE), were compared with those from a model in which subtypes were homogeneously distributed at random throughout the mesh

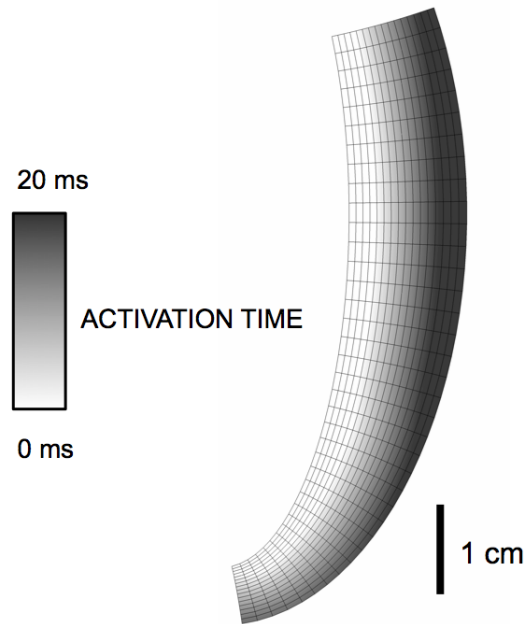


Figure 3.2: Myocardial activation time as calculated in the BASELINE simulation. Activation was the result of simultaneously stimulating the entire endocardial surface.

(HOM). Assignment of cell subtype in the HOM simulation was performed in an element-wise fashion such that total myocardial volume of corresponding to each subtype was equal in both models (Figure 3.1, *b* and *c*).

3.3.1 Hemodynamics and electrical activation

Global LV pump function during ejection against arterial loading generated by the three-element Windkessel model showed only minor differences between BASELINE and HOM cases. The largest difference was in ejection time, which was 6% shorter in the HOM case (104 for BASELINE vs. 98 ms in HOM). Maximum dP/dt , peak LV pressure, and stroke volume were essentially the same between the two cases (see Table 2). Total transmural delay of action potential propagation, measured in the thickest region of the wall, was also nearly the same (24.0 ms for BASELINE vs. 23.9 in HOM). The spatial pattern of electrical activation produced in the BASELINE model is shown in Figure 3.2.

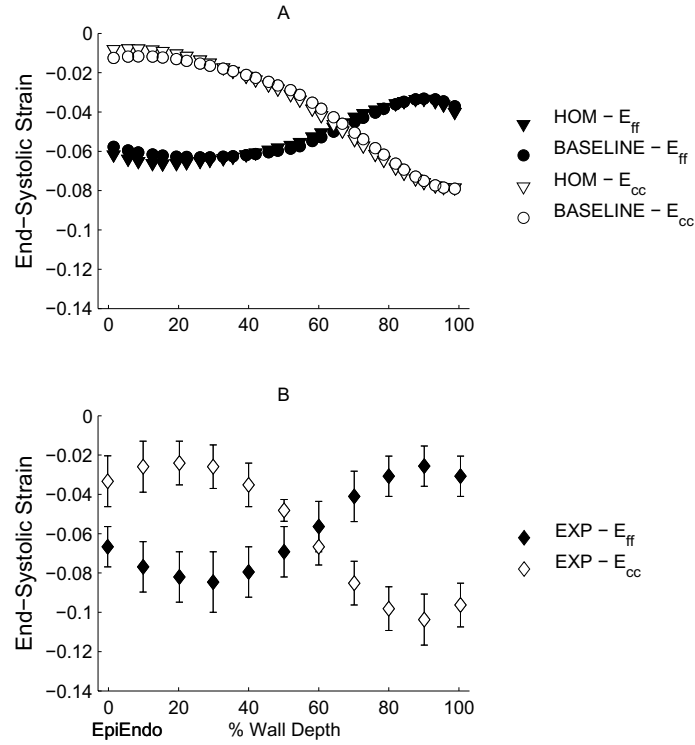


Figure 3.3: Comparison of model-generated fibre (E_{ff}) and cross-fibre (E_{cc}) strains at end-systole (a) with those reported experimentally in the study of Mazhari et al. [6] (b). BASELINE and HOM simulations produced essentially identical transmural patterns of fibre and crossfibre strains in spite of different spatial arrangement of myocyte subtypes. End-systolic strains produced by the models displayed transmural patterns that were in good agreement with experimental measurements.

3.3.2 Transmural gradients of end-systolic strains

The two cases displayed nearly identical transmural gradients of fibre and cross-fibre strain at the time of aortic valve closure (Figure 3.3a). For both simulations, end-systolic fibre and cross-fibre strains were in good qualitative agreement with experiments [6] in terms of strain magnitudes and transmural trends (Figure 3.3). The largest negative fibre strain measured in the study of Mazhari *et al.* [6] was -0.085 at 30% wall depth from the epicardium, the largest in simulations were -0.063 (BASELINE) and -0.066 (HOM), at wall depths of 26% and 15%, respectively.

3.3.3 Time course of fibre strain during systole

Time courses of fibre strain were markedly different between BASELINE and HOM simulations during isovolumic contraction and early ejection, in contrast to their similarity at end-systole (Figure 3.4). The HOM model produced a time course of fibre strain during isovolumic contraction which had a smaller transmural range than the heterogeneous case (0.05 HOM vs. 0.07 BASELINE at aortic valve opening). Also, in the HOM case fibres at both epicardial and endocardial extremes were stretched prior to ejection, in the BASELINE case only endocardial fibres were stretched during the same period (Figure 3.4, *a* and *b*). Fibre shortening in the BASELINE model was greatest in the epicardial region throughout systole, while in the HOM model mid-myocardial fibre shortening tended to be greatest.

Since the only time courses of transmurally distributed fibre strains reported in the literature are for individual animals [10, 11], here we use previously unpublished measurements from our laboratory in six anesthetized dogs for comparison with model-produced time courses (Figure 3.4). Fibre strain time courses of individual dogs are presented in Appendix B. Large differences in fibre strain magnitude and transmural range were observed across animals (Figure 3.4*c*). When maximum and minimum fibre strains across the wall were examined at each time point and averaged across dogs, a general stretching of fibres (without regard to transmural location) can be observed around the time of aortic valve opening (Figure 3.4*c*). On an individual basis, maximum fibre strain at the time of aortic valve opening occurred at the epicardium in four of the six dogs, and was located at the endocardium in the other two (see Appendix B).

3.3.4 Sensitivity Analysis

Additional simulations were performed to assess the sensitivity of global LV function and regional fibre strains to factors other than cell subtype distribution (Table 2). Effects of cell subtype composition were examined by using midmyocardial cell parameters throughout the mesh (column ALLMID in Table 2). Activation time was altered by doubling the conductivity, from 2.4 to 4.8 mS cm⁻¹ (HIGH-COND). Fibre angles were altered in two separate simulations to match the largest

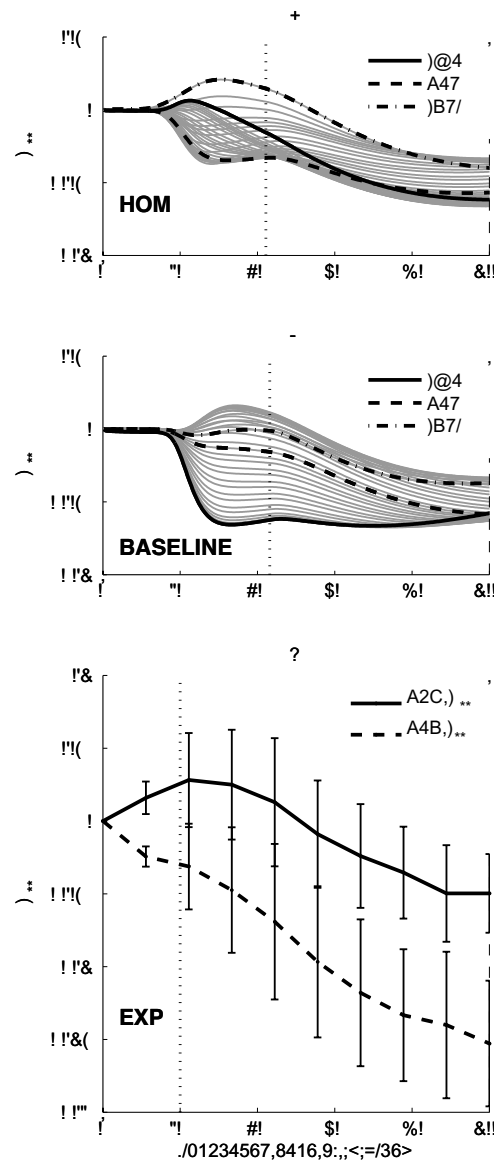


Figure 3.4: Comparison of time courses of fibre strain (E_{ff}) in models and experiments. Time courses have been normalised to the length of the systolic interval in each case, with dotted vertical lines indicating aortic valve opening. Shaded lines in panels *a* and *b* represent fibre strains at wall depths between the heavier lines corresponding to epi-, mid-, and endocardial depths as labelled. Experimentally measured strains (*c*) were obtained in an anesthetized adult dogs ($n = 6$) using radiopaque beads implanted in the LV free wall. Plotted values represent means \pm S.D. of maximum and minimum fibre strains at each time point across animals.

and smallest total transmural gradients observed among individual dogs used in the study of Mazhari *et al.* [6]. In these simulations, the total transmural fibre angle ranges were 170 and 112 degrees (STEEPFIB and SHALLOWFIB, respectively), compared with a range of 145 degrees used for all other simulations. The transmural gradient in sarcomere length was removed and instead set to the average value of $1.95 \mu\text{m}$ [36] throughout the mesh (NOSLGRAD). The EDP used to inflate the model prior to activation was increased by 50% (from 3.9 to 5.9 mmHg) to examine the effect of preload (HIGHEDP). This increase in preload resulted in a new end-diastolic LV volume of 42.7 ml. Finally, effects of afterload on modelled results was assessed by reducing initial aortic pressure by 25%, from 67.5 to 50.6 mmHg (LOWAOP).

Time courses of fibre strain were reduced to two moments in the cycle, aortic valve opening and closure, for purposes of comparison between simulations. At these times, minimum and maximum fibre strains and their corresponding wall depths were determined. Average transmural fibre strain and absolute range were also calculated. To account for possible variation of the results due to the longitudinal wall location at which strains were calculated, these fibre strain parameters were calculated at a basal location ($\mu = 90$ degrees) in addition to the standard apical location described in the Methods ($\mu = 40$ degrees). Thresholds for significance were defined relative to the BASELINE simulation for each measure included in the sensitivity analysis and are as follows: >0.02 change for fibre strain values (including strain range), >20 percentage-point change for percent wall depth of minimum/maximum strain, and $>20\%$ change in hemodynamic measures and activation time.

Results from these simulations are compared with those from the BASELINE simulation in Table 2. The largest changes to hemodynamic function were seen in the HIGHEDP and LOWAOP simulations, which showed 47% and 35% increases in stroke volume, respectively. HIGHEDP also produced a 14% increase in maximum dP/dt. For both HIGHEDP and LOWAOP, hemodynamic changes were not associated with significant change in fibre strains. The ALLMID simulation produced a 20% increase in ejection time as well as changes to fibre strains at

the time of aortic valve opening. Greatest among these was a reduction in strain range from 0.07 to 0.02. Apart from the HOM and ALLMID simulations, none of the simulated conditions produced above-threshold changes to strain metrics at aortic valve opening. At end-systole, only the SHALLOWFIB simulation produced significant changes to fibre strains.

All strain differences that were above-threshold when calculated at the apical location remained significant when a more basal wall location was used (lower half of table 2). Several additional differences became significant under these conditions, including location in the wall of minimum and maximum fibre strains at end-systole for the STEEPFIB simulation.

3.4 Discussion

We have studied the role of myocyte heterogeneity in LV function by coupling a model of length- and velocity-dependent EC-coupling dynamics with finite element models of LV action potential propagation and mechanics. EC-coupling model parameters were spatially varied according to previous work [25, 29] to reflect measured regional differences in cell behavior. Results from the model in which epi, mid, and endo cells were arranged in their corresponding layers were compared with those obtained by homogeneously distributing cell subtypes throughout the LV wall. Differences in fibre strain time courses between the models were clearly evident during early systole, but essentially vanished by end-systole. There was no substantial difference in hemodynamic performance between the two models. Several additional simulations in which other factors such as fibre angle, activation time, preload, and afterload were perturbed revealed that transmural strain patterns early in systole were still most sensitive to the cell subtype distribution. Additionally, end-systolic fibre strains were seen to be sensitive to changes in fibre angles and the longitudinal location of strain measurement.

Table 3.2: Sensitivity of model-generated haemodynamics, activation delay and transmural fibre strain to perturbation. Asterisks indicate the following: >20% difference from baseline for haemodynamics and activation delay; >0.02 absolute difference from baseline for fibre strains; and >20 percentage-point difference in percentage wall depth. Abbreviations: E_{ff} , fibre strain; ET, ejection time; LVP, left ventricular pressure; SV, stroke volume; AVO, aortic valve opening; Min./Max., minimum/maximum fibre strain; % WD, location of min./max. fibre strain as a percentage of total ventricular wall depth measured from the epicardial surface; and EF, ejection fraction. For an explanation of the column headings, see §3.3.4.

	BASELINE	HOM	ALLMID	HIGHCOND	STEEPFIB	SHALLOWFIB	NOSLGRAD	HIGHEDP	LOWAOP
Hemodynamics									
ET (ms)	104.0	98.0	125.5*	103.5	103.5	106.5	104.0	115.5	112.5
Max. LVP (mmHg)	74.5	75.0	73.5	74.5	73.9	74.7	74.4	78.8	62.0
dP/dt Max. (mmHg ms ⁻¹)	1.88	1.91	1.68	1.75	1.81	1.87	1.84	2.14	1.88
EF (%)	17.26	17.21	17.80	17.15	16.41	18.28	17.31	22.89*	23.32*
SV (mL)	6.64	6.62	6.84	6.60	6.34	6.92	6.66	9.78*	8.97*
Transmural Delay of Activation (ms)									
	24.0	23.9	23.9	17.55*	24.0	24.0	24.0	23.3	24.0
Transmural E_{ff}, apical location, at AVO									
Min.	-0.062	-0.033*	-0.032*	-0.062	-0.066	-0.070	-0.058	-0.062	-0.065
% WD of Min.	1	55*	15	1	6	6	6	1	1
Max.	0.012	0.015	-0.011*	0.009	0.013	0.023	0.011	0.018	0.016
% WD of Max.	82	99	99	79	67	99	84	79	82
Range	0.074	0.048*	0.021*	0.071	0.079	0.093	0.069	0.079	0.081
Average	-0.020	-0.022	-0.026	-0.020	-0.022	-0.023	-0.019	-0.016	-0.019
Transmural E_{ff}, apical location, at end-systole									
Min.	-0.063	-0.066	-0.067	-0.063	-0.066	-0.072	-0.062	-0.070	-0.072
% WD of Min.	26	15	15	26	13	29	36	33	33
Max.	-0.033	-0.033	-0.035	-0.033	-0.034	-0.021	-0.036	-0.043	-0.041
% WD of Max.	90	90	88	90	73	99	93	88	90
Range	0.030	0.033	0.032	0.030	0.033	0.051*	0.026	0.027	0.031
Average	-0.052	-0.052	-0.053	-0.052	-0.051	-0.057	-0.052	-0.060	-0.060
Transmural E_{ff}, basal location, at AVO									
Min.	-0.049	-0.020*	-0.023*	-0.052	-0.053	-0.059	-0.044	-0.047	-0.047
% WD of Min.	1	75*	84*	1	5	1	1	1	1
Max.	0.014	0.001	-0.007*	0.021	0.022	0.025	0.014	0.022	0.017
% WD of Max.	69	99*	12*	72	59	90*	69	72	69
Range	0.063	0.021*	0.016*	0.072	0.075	0.084	0.058	0.069	0.064
Average	-0.010	-0.012	-0.012	-0.009	-0.013	-0.012	-0.009	-0.006	-0.007
Transmural E_{ff}, basal location, at end-systole									
Min.	-0.050	-0.053	-0.053	-0.050	-0.060	-0.064	-0.047	-0.059	-0.060
% WD of Min.	15	1	8	19	99*	28	32	28	28
Max.	-0.035	-0.033	-0.035	-0.034	-0.028	-0.018	-0.039	-0.044	-0.041
% WD of Max.	84	87	81	84	59*	99	87	84	87
Range	0.015	0.019	0.019	0.016	0.032	0.046*	0.008	0.015	0.019
Average	-0.043	-0.043	-0.044	-0.043	-0.044	-0.049	-0.043	-0.053	-0.053

3.4.1 Transmural gradients of end-systolic fibre strains

End-systolic fibre strains have been used as an index of regional ventricular function [6]. We used such strains, measured under carefully-controlled conditions in a previous study by our group [6], to validate end-systolic strains produced by the model (Figure 3.3). The lack of substantial differences in end-systolic fibre strains between BASELINE and HOM models was unexpected given large differences seen at other times throughout systole (Figures 3.3 and 3.4). The similarity between the models indicates that end-systolic fibre strain was not sensitive to heterogeneous distribution of cell subtypes. That end-systolic fibre strain was also insensitive to the overall cell subtype composition is evident from results of the ALLMID simulation. The sensitivity analysis instead suggests that end-systolic fibre strains are highly dependent on a combination of fibre angle and measurement location. The latter implicates wall thickness or curvature as important determinants of end-systolic fibre strain.

3.4.2 Effects of cellular heterogeneity on the time course of systolic fibre strains

Transmurally heterogeneous arrangement of myocyte subtypes resulted in large gradients of fibre strain around the beginning of ejection (Table 2 and Figure 3.4*b*). These gradients are larger than those from simulations in which cell subtype assignment was perturbed (HOM, ALLMID, Table 2). While this difference is interesting, variability of experimentally-measured time courses prevents stringent validation of those produced by the BASELINE simulation. The fibre strain range measured in dogs for this study was sufficiently large to accommodate strains produced by either of the two models (Figure 3.4).

The sensitivity analysis performed here may partially explain the large variability of experimental time courses. For instance, a combination of perturbations to cell subtype composition (ALLMID) and location of strain measurement (basal) reversed the transmural gradient of fibre strain at aortic valve opening in comparison with BASELINE (see Table 2).

Interestingly, a 27% reduction in transmural activation delay had essentially no effect on fibre strain patterns at either of the two cycle times reported (BASELINE vs. HIGHCOND, Table 2). The present results do not therefore support the notion that activation delay and cellular heterogeneity interact to affect fibre strains as previously proposed [8, 9].

3.4.3 Comparison with previous work

Previous modelling studies have examined the interaction of activation delay with heterogeneous electromechanics [17, 43]. Solovyova and co-workers [43] modelled two muscle elements coupled in series, one (representing endocardial cells) having slower twitch kinetics than the other. They found that in the presence of an activation delay the heterogeneous duplex produced greater twitch force than either type of homogeneous pairing (both slow or both fast). We failed to observe any connection between heterogeneity and overall contractility. This discrepancy may be attributed to the fact that in our model, heterogeneous muscle fibres are essentially parallel to each other in the ventricular wall, not in series as in the work of Solovyova *et al.* [43].

Nickerson *et al.* [17] used a representation of LV mechanics similar to that used here to examine the effects of heterogeneous action potential duration on transmural fibre strain. In both their study and ours, stretching of endocardial fibres in late isovolumic contraction was observed. Nickerson *et al.* also noted a significant difference in fibre strain dispersion between homogeneous and heterogeneous cases during action potential repolarization. In this study we have referenced strains to hemodynamic events rather than action potential repolarization, which prevents direct comparison. However, differences in strain time course can be seen between BASELINE and HOM simulations as late as 80% into the systolic interval (Figure 3.4), in spite of their close agreement at the moment of aortic valve closure (Figure 3.3a). Thus, the results of both studies are fairly consistent.

Other studies have examined sensitivity of transmural strains to fibre angle distribution as we did in the SHALLOWFIB and STEEPFIB simulations. We found that the range of fibre strains was sensitive to the fibre distribution, which

has been shown before by Bovendeerd *et al.* [44] and Geerts *et al.* [45]. Our results are in agreement with the latter study in that a shallower transmural fibre angle distribution resulted in an increase in the coefficient of variation of sarcomere length shortening during ejection [45] and range of end-systolic fibre strains in our study. The insensitivity of range of fibre strains at aortic valve opening to the gradient of resting sarcomere length (BASELINE vs. NOSLGRAD, Table 2) was in agreement with the findings of Kerckhoffs *et al.* [8].

3.4.4 Limitations and future work

The simplified model of LV geometry used in the present study is appropriate for the examination of transmural gradients in LV strain, but does not account for the activity of the right ventricle (RV). Because coupling with the RV might influence stresses and strains at the LV-RV junction and in the septum, our model applies only to the left ventricular free wall. In addition, the activation sequence used here assumes simultaneous activation of the entire endocardium, which is a simplification with regard to in-vivo measurements of myocardial activation [46, 47]. Finally, we have considered only transmural variations in myocyte properties, whereas apex-base and LV-RV variations have also been identified [48–51]. The strong effects of heterogeneous myocyte properties and spatial arrangement on fibre strain time course shown in this study suggest that efforts to represent additional heterogeneities would be worthwhile.

Myocardial cell model parameters used here were chosen to reproduce behaviors observed in isolated cells, which can be quite different from that occurring in vivo. The consequences of this are perhaps most evident in the magnitude of peak end-systolic fibre shortening produced by the present models (6%), which is substantially lower than the experimental mean observed in data presented in this study (15%).

The cellular electromechanics model used here, with its accompanying parameter sets for the three myocyte sub-types is subject to its own set of limitations (see [25] for discussion). Parameters in the original contraction model of Rice *et al.* [24] derive mainly from rat data. In previous work [25], we modified a limited

number of these parameters to reproduce transmural variations in time to peak unloaded shortening reported among canine myocytes [9]. The paucity of canine-specific muscle physiology data and its transmural variation currently prevents a more detailed validation. The high sensitivity of early-systolic fibre strains to cellular electromechanical function shown in this study suggests that future studies are needed in which the location of strain measurements are more carefully controlled and local fiber angle distributions are measured individually for each experimental subject.

3.4.5 Conclusions

The present results suggest that heterogeneous myocyte behavior exerts substantial effects on regional myocardial strains during early systole. At the same time, end-systolic fibre strains appear insensitive to heterogeneities. Instead, strains at end-systole were most sensitive to the combined effects of fibre angle and longitudinal measurement location. Finally, global LV function was found to be insensitive to perturbations of spatial myocyte subtype distribution. Multi-scale computational models of ventricular electromechanics have the potential to help understand the integrative nature of myocardial function in vivo in terms of underlying cellular and EC coupling properties, however, such models must reflect regional variations in these properties with increasing accuracy in order to be effective.

Acknowledgments

This study has been supported by an American Heart Association Pre-doctoral Fellowship (to S.G.C.), Medtronic, UC Discovery Grant ITL06-10159 (to A.D.M.), the National Biomedical Computation Resource (NIH grant P41 RR08605) (to A.D.M), the National Science Foundation (BES-0506252) (to A.D.M) and NIH grant HL32583 (to J.H.O.). This investigation was conducted in part using a facility constructed with support from Research Facilities Improvement Program Grant Number C06 RR-017588-01 from the National Center for Research

Resources, National Institutes of Health.

Andrew McCulloch and Jeffrey Omens are co-founders of and consultants to Insilicomed Inc., a licensee of UCSD-owned software used in this research. Insilicomed was not involved in this research. Lawrence Mulligan is an employee of Medtronic.

Chapter 3, in full, is a reprint of the published article “Effect of Transmurally Heterogeneous Myocyte Excitation-Contraction Coupling on Left Ventricular Electromechanics.” Campbell S.G., Howard E.J., Aguado-Sierra J., Coppola B.A., Omens J.H., Mulligan L.J., McCulloch A.D., and Kerckhoffs, R.C.P. *Experimental Physiology*. 95:541-552, 2009. The dissertation author was the primary investigator and author of this paper.

References

- [1] Arts, T., Reneman, R.S., and Veenstra, P.C., 1979. A model of the mechanics of the left ventricle. *Ann Biomed Eng*, 7:299–318.
- [2] Arts, T., Prinzen, F.W., Snoeckx, L.H., Rijcken, J.M., and Reneman, R.S., 1994. Adaptation of cardiac structure by mechanical feedback in the environment of the cell: a model study. *Biophys J*, 66:953–61.
- [3] Legrice, I.J., Smaill, B.H., Chai, L.Z., Edgar, S.G., Gavin, J.B., and Hunter, P.J., 1995. Laminar structure of the heart: ventricular myocyte arrangement and connective tissue architecture in the dog. *Am J Physiol*, 269:H571–82.
- [4] Guccione, J.M., Costa, K.D., and McCulloch, A.D., 1995. Finite element stress analysis of left ventricular mechanics in the beating dog heart. *J Biomech*, 28:1167–77.
- [5] Costa, K.D., Takayama, Y., McCulloch, A.D., and Covell, J.W., 1999. Laminar fiber architecture and three-dimensional systolic mechanics in canine ventricular myocardium. *Am J Physiol*, 276:H595–607.
- [6] Mazhari, R., Omens, J.H., Pavelec, R.S., Covell, J.W., and McCulloch, A.D., 2001. Transmural distribution of three-dimensional systolic strains in stunned myocardium. *Circulation*, 104:336–41.
- [7] Tseng, W.Y., Reese, T.G., Weisskoff, R.M., Brady, T.J., and Wedeen, V.J., 2000. Myocardial fiber shortening in humans: initial results of MR imaging. *Radiology*, 216:128–39.

- [8] Kerckhoffs, R.C.P., Bovendeerd, P.H.M., Prinzen, F.W., Smits, K., and Arts, T., 2003. Intra- and interventricular asynchrony of electromechanics in the ventricularly paced heart. *Journal of Engineering Mathematics*, 47:201–216.
- [9] Cordeiro, J., Greene, L., Heilmann, C., Antzelevitch, D., and Antzelevitch, C., 2004. Transmural heterogeneity of calcium activity and mechanical function in the canine left ventricle. *Am J Physiol Heart Circ Physiol*, 286:H1471–9.
- [10] Ashikaga, H., Criscione, J.C., Omens, J.H., Covell, J.W., and Ingels, N.B., 2004. Transmural left ventricular mechanics underlying torsional recoil during relaxation. *Am J Physiol Heart Circ Physiol*, 286:H640–7.
- [11] Ashikaga, H., Coppola, B.A., Hopfenfeld, B., Leifer, E.S., McVeigh, E.R., and Omens, J.H., 2007. Transmural dispersion of myofiber mechanics: implications for electrical heterogeneity in vivo. *J Am Coll Cardiol*, 49:909–16.
- [12] Usyk, T.P., Legrice, I.J., and McCulloch, A.D., 2002. Computational model of three-dimensional cardiac electromechanics. *Computing and Visualization in Science*, 4:249–257.
- [13] Usyk, T.P. and McCulloch, A.D., 2003. Electromechanical model of cardiac resynchronization in the dilated failing heart with left bundle branch block. *J Electrocardiol*, 36 Suppl:57–61.
- [14] Sermesant, M., Rhode, K., Sanchez-Ortiz, G.I., Camara, O., Andriantsimiavona, R., Hegde, S., Rueckert, D., Lambiase, P., Bucknall, C., Rosenthal, E., Delingette, H., Hill, D.L.G., Ayache, N., and Razavi, R., 2005. Simulation of cardiac pathologies using an electromechanical biventricular model and XMR interventional imaging. *Med Image Anal*, 9:467–80.
- [15] Kerckhoffs, R.C.P., McCulloch, A.D., Omens, J.H., and Mulligan, L.J., 2009. Effects of biventricular pacing and scar size in a computational model of the failing heart with left bundle branch block. *Med Image Anal*, 13:362–9.
- [16] Watanabe, H., Sugiura, S., Kafuku, H., and Hisada, T., 2004. Multiphysics simulation of left ventricular filling dynamics using fluid-structure interaction finite element method. *Biophysical Journal*, 87:2074–85.
- [17] Nickerson, D., Smith, N., and Hunter, P., 2005. New developments in a strongly coupled cardiac electromechanical model. *Europace*, 7 Suppl 2:118–27.
- [18] Nash, M.P. and Panfilov, A.V., 2004. Electromechanical model of excitable tissue to study reentrant cardiac arrhythmias. *Prog Biophys Mol Biol*, 85:501–22.

- [19] Niederer, S.A. and Smith, N.P., 2008. An improved numerical method for strong coupling of excitation and contraction models in the heart. *Prog Biophys Mol Biol*, 96:90–111.
- [20] Kohl, P., Hunter, P., and Noble, D., 1999. Stretch-induced changes in heart rate and rhythm: clinical observations, experiments and mathematical models. *Prog Biophys Mol Biol*, 71:91–138.
- [21] Niederer, S.A. and Smith, N.P., 2007. A mathematical model of the slow force response to stretch in rat ventricular myocytes. *Biophysical Journal*, 92:4030–44.
- [22] Kerckhoffs, R.C.P., Faris, O.P., Bovendeerd, P.H.M., Prinzen, F.W., Smits, K., McVeigh, E.R., and Arts, T., 2005. Electromechanics of paced left ventricle simulated by straightforward mathematical model: comparison with experiments. *Am J Physiol Heart Circ Physiol*, 289:H1889–97.
- [23] Usyk, T.P. and McCulloch, A.D., 2003. Relationship between regional shortening and asynchronous electrical activation in a three-dimensional model of ventricular electromechanics. *J Cardiovasc Electrophysiol*, 14:S196–202.
- [24] Rice, J., Wang, F., Bers, D., and TOMBE, P.D., 2008. Approximate model of cooperative activation and crossbridge cycling in cardiac muscle using ordinary differential equations. *Biophysical Journal*, 95:2368–90.
- [25] Campbell, S., Flaim, S., Leem, C., and McCulloch, A., 2008. Mechanisms of transmurally-varying myocyte electromechanics in an integrated computational model. *Philosophical transactions Series A, Mathematical, physical, and engineering sciences*, 366:3361.
- [26] Sicouri, S. and Antzelevitch, C., 1991. A subpopulation of cells with unique electrophysiological properties in the deep subepicardium of the canine ventricle. The M cell. *Circulation Research*, 68:1729–41.
- [27] Sicouri, S., Fish, J., and Antzelevitch, C., 1994. Distribution of M cells in the canine ventricle. *J Cardiovasc Electrophysiol*, 5:824–37.
- [28] Greenstein, J., Hinch, R., and Winslow, R., 2006. Mechanisms of excitation-contraction coupling in an integrative model of the cardiac ventricular myocyte. *Biophys J*, 90:77–91.
- [29] Flaim, S.N., Giles, W.R., and McCulloch, A.D., 2006. Contributions of sustained INa and IKv43 to transmural heterogeneity of early repolarization and arrhythmogenesis in canine left ventricular myocytes. *Am J Physiol Heart Circ Physiol*, 291:H2617–29.

- [30] Gordon, A.M., Huxley, A.F., and Julian, F.J., 1966. The variation in isometric tension with sarcomere length in vertebrate muscle fibres. *The Journal of Physiology*, 184:170–92.
- [31] Razumova, M.V., Bukatina, A.E., and Campbell, K.B., 1999. Stiffness-distortion sarcomere model for muscle simulation. *J Appl Physiol*, 87:1861–76.
- [32] Hairer, E. and Wanner, G., 1999. Stiff differential equations solved by Radau methods. *Journal of Computational and Applied Mathematics*, 111:93–111.
- [33] Costa, K.D., Hunter, P.J., Wayne, J.S., Waldman, L.K., Guccione, J.M., and McCulloch, A.D., 1996. A three-dimensional finite element method for large elastic deformations of ventricular myocardium: II—Prolate spheroidal coordinates. *J Biomech Eng*, 118:464–72.
- [34] Streeter, D.D. and Hanna, W.T., 1973. Engineering mechanics for successive states in canine left ventricular myocardium. I. Cavity and wall geometry. *Circulation Research*, 33:639–55.
- [35] Rodriguez, E.K., Omens, J.H., Waldman, L.K., and McCulloch, A.D., 1993. Effect of residual stress on transmural sarcomere length distributions in rat left ventricle. *Am J Physiol*, 264:H1048–56.
- [36] Rodriguez, E.K., Hunter, W.C., Royce, M.J., Leppo, M.K., Douglas, A.S., and Weisman, H.F., 1992. A method to reconstruct myocardial sarcomere lengths and orientations at transmural sites in beating canine hearts. *Am J Physiol*, 263:H293–306.
- [37] Streeter, D.D. and Hanna, W.T., 1973. Engineering mechanics for successive states in canine left ventricular myocardium. II. Fiber angle and sarcomere length. *Circulation research*, 33:656–64.
- [38] Rogers, J.M. and McCulloch, A.D., 1994. A collocation–Galerkin finite element model of cardiac action potential propagation. *IEEE Trans Biomed Eng*, 41:743–57.
- [39] Flaim, S.N., Giles, W.R., and McCulloch, A.D., 2007. Arrhythmogenic consequences of Na⁺ channel mutations in the transmurally heterogeneous mammalian left ventricle: analysis of the I1768V SCN5A mutation. *Heart Rhythm*, 4:768–78.
- [40] Yan, G.X., Shimizu, W., and Antzelevitch, C., 1998. Characteristics and distribution of M cells in arterially perfused canine left ventricular wedge preparations. *Circulation*, 98:1921–7.

- [41] Kerckhoffs, R.C.P., Neal, M.L., Gu, Q., Bassingthwaite, J.B., Omens, J.H., and McCulloch, A.D., 2007. Coupling of a 3D finite element model of cardiac ventricular mechanics to lumped systems models of the systemic and pulmonic circulation. *Ann Biomed Eng*, 35:1–18.
- [42] Waldman, L.K., Fung, Y.C., and Covell, J.W., 1985. Transmural myocardial deformation in the canine left ventricle. Normal in vivo three-dimensional finite strains. *Circulation Research*, 57:152–63.
- [43] Solovyova, O., Vikulova, N., and Katsnelson, L., 2003. Mechanical Interaction of Heterogeneous Cardiac Muscle Segments In Silico: Effects on Ca²⁺ Handling and Action Potential. *Internat J Bifurcation Chaos*, 13:3757–3782.
- [44] Bovendeerd, P.H., Arts, T., Huyghe, J.M., van Campen, D.H., and Reneman, R.S., 1992. Dependence of local left ventricular wall mechanics on myocardial fiber orientation: a model study. *J Biomech*, 25:1129–40.
- [45] Geerts, L., Kerckhoffs, R., Bovendeerd, P.H.M., and Arts, T., 2003. Towards Patient Specific Models of Cardiac Mechanics: a Sensitivity Study. *Lecture Notes Comp Sci*, pages 81–90.
- [46] Scher, A., Young, A., Malmgren, A., and Paton, R., 1953. Spread of electrical activity through the wall of the ventricle. *Circulation Research*, 1:539–47.
- [47] Durrer, D., van Dam, R.T., Freud, G.E., Janse, M.J., Meijler, F.L., and Arzbaecher, R.C., 1970. Total excitation of the isolated human heart. *Circulation*, 41:899–912.
- [48] Kondo, R., Dederko, D., Teutsch, C., Chrast, J., Catalucci, D., Chien, K., and Giles, W., 2006. Comparison of contraction and calcium handling between right and left ventricular myocytes from adult mouse heart: a role for repolarization waveform. *The Journal of Physiology*, 571:131.
- [49] Carnes, C.A., Geisbuhler, T.P., and Reiser, P.J., 2004. Age-dependent changes in contraction and regional myocardial myosin heavy chain isoform expression in rats. *J Appl Physiol*, 97:446–53.
- [50] Krenz, M., Sadayappan, S., Osinska, H.E., Henry, J.A., Beck, S., Warshaw, D.M., and Robbins, J., 2007. Distribution and structure-function relationship of myosin heavy chain isoforms in the adult mouse heart. *J Biol Chem*, 282:24057–64.
- [51] Litten, R.Z., Martin, B.J., Buchthal, R.H., Nagai, R., Low, R.B., and Alpert, N.R., 1985. Heterogeneity of myosin isozyme content of rabbit heart. *Circulation Research*, 57:406–14.

Chapter 4

A Markov Model of Cardiac Myofilament Activation

Abstract

We developed a Markov model of cardiac thin filament activation that accounts for interactions among nearest-neighbor regulatory units (RU) in a spatially-explicit manner. Interactions were assumed to arise from structural coupling of adjacent tropomyosins (Tm), such that Tm shifting within each RU was influenced by Tm status of its neighbors. Simulations using the model demonstrate that this coupling is sufficient to produce observed cooperativity in both steady-state and dynamic force- Ca^{2+} relationships. The model was further validated by comparison with reported responses under various conditions including inhibition of myosin binding and the addition of strong-binding, non-force-producing myosin fragments. The model also reproduced the effects of 2.5 mM added Pi on Ca^{2+} -activated force and the rate of force redevelopment measured in skinned rat myocardial preparations. Model analysis suggests that Tm-Tm coupling potentiates the activating effects of strongly-bound crossbridges and contributes to force- Ca^{2+} dynamics of intact cardiac muscle. The model further predicts that activation at low Ca^{2+} concentrations is cooperatively inhibited by nearest-neighbors, requiring Ca^{2+} binding to $> 25\%$ of RUs to produce appreciable levels of force. Without excluding other

putative cooperative mechanisms, these findings suggest that structural coupling of adjacent Tm molecules contributes to several properties of cardiac myofilament activation.

4.1 Introduction

The mechanisms by which Ca^{2+} transients in cardiac myocytes determine the dynamics of systolic tension development and relaxation are critical to normal heart function, and to key alterations in diseases such as heart failure. That mutations in each component of the Ca^{2+} regulatory switch have been associated with cardiomyopathy underscores the importance of thin filament activation mechanisms in cardiac mechanical performance [1, 2].

The troponin complex (Tn) and tropomyosin (Tm) are the primary components of the thin filament regulatory switch. Ca^{2+} binding to a low-affinity site on the troponin C (TnC) subunit of Tn induces a conformational change that in turn allows Tm to move across the surface of the actin filament, exposing sites on actin to which the S1 region of myosin cyclically attaches to generate force [3]. However, there is also evidence for reverse interactions in this cascade. Experiments in skinned myocytes have shown that S1 binding to actin increases the affinity of TnC for Ca^{2+} [4] and is able to activate force production in myofilaments at extremely low $[\text{Ca}^{2+}]$ [5]. These observations suggest that myosin crossbridge (XB) formation plays an important part in the steep cooperative relationship between steady-state force and activating Ca^{2+} that is well recognized in cardiac muscle.

Other molecular interactions have been identified with cooperative myofilament activation. Neighboring Tm molecules along the actin filament overlap by 8-11 amino acid residues [6]. Steric end-to-end interactions in this region may modulate cooperative binding of S1 to regulated actin in vitro [7], and spatially-explicit models have demonstrated that the propagation of this interaction among adjacent Tm molecules can produce cooperative steady-state force- $[\text{Ca}^{2+}]$ responses (see [8] and references therein). However, it was not feasible in these models to investigate the dynamics of cardiac myocyte twitch tension or the observed strong

$[\text{Ca}^{2+}]$ dependence of the rate at which cardiac muscle redevelops force following a length perturbation (k_{tr}). Mean-field models do recapitulate features of cardiac force- $[\text{Ca}^{2+}]$ dynamics [9, 10], but all of them have relied on empirical feedback mechanisms that may not accurately represent proposed structural mechanisms [8, 11].

Among many putative cooperative mechanisms [8], the purpose of this study was to test the ability of Tm-Tm coupling to reproduce both steady-state and dynamic Ca^{2+} -force relations seen in cardiac muscle. We formulated a Markov model of thin filament activation based on Tm-Tm coupling and recognized structural relations among signaling proteins. A continuous-time implementation of the model was used to compute both steady-state and dynamic responses through an efficient new technique for quasi-explicit representation of nearest-neighbor interactions. The model was also solved using Monte Carlo methods for perturbations requiring fully-explicit representation of full-length filaments and for validation of continuous-time solutions. Using the model, we show that Tm-Tm interactions potentiate the activating effects of XBs and are sufficient to explain steep cooperative activation of force, the observed dependence of k_{tr} on $[\text{Ca}^{2+}]$, and Ca^{2+} -force dynamics during isometric myocyte twitches.

4.2 Model Development

The model is based on actin regulatory units (RUs), comprising seven actin monomers, TnC, TnI (the inhibitory subunit of Tn), and Tm, together with the S1 region of myosin. We assume conformations for each component as a simplification of the Tn switch mechanism [3]. TnC has Ca^{2+} -free and Ca^{2+} -bound conformations, and a third conformation associated with bulk movement of the Tn complex due to Tm shifting [12]. The C-terminal region of TnI is assumed to be either bound to actin or bound to TnC [3]. Three conformations of Tm are assumed, corresponding to observed structural positions on the surface of the actin filament [13] and following the model of McKillop and Geeves [14]. In the blocking position, S1 binding sites on actin are sterically blocked by Tm, in the closed position only

weak binding of S1 to actin is possible, and the open position corresponds to the presence of strongly-bound S1.

4.2.1 Assumptions of the Model

The model formulation is based on four allosteric interactions:

1. Ca^{2+} binding to TnC induces transfer of TnI from actin to TnC, dissociation of Ca^{2+} reverses the transfer,
2. Tm can transition from blocked to closed only when TnI is dissociated from actin,
3. Tm must be in the blocked conformation before TnI can re-bind actin and before Ca^{2+} can dissociate from TnC, and
4. Strong binding of myosin places and holds Tm in the open conformation.

Assumptions 1-3 collectively implement the tight coupling premise [15], because activation of Tn is tightly coupled to the binding of Ca^{2+} , and because Ca^{2+} cannot dissociate from Tn when Tm is in the closed or open positions. Assumption 3 is based on the idea that when in the closed or open states Tm prevents the inhibitory region of TnI from re-binding actin, similar to the assumption used by Smith & Geeves [16]. They considered TnI and S1 as competing for the same binding site on actin, while we assume TnI and Tm compete such that Tm can influence Tn even in the absence of S1 binding.

We initially made the simplification that each RU in effect regulated a single myosin binding site. An augmented version of the model allowing binding of >1 XB was also tested, since structural studies [17] have suggested that in the intact myofilament lattice as many as three XBs can bind a single RU (see Appendix C). A similar assumption, made necessary by representation of the thin filament at RU-level resolution, is that Ca^{2+} binding to an RU cannot directly expose binding sites in adjacent RUs.

The above assumptions form a four-state model of an individual RU regulated by Ca^{2+} , each state containing information about the conformational status

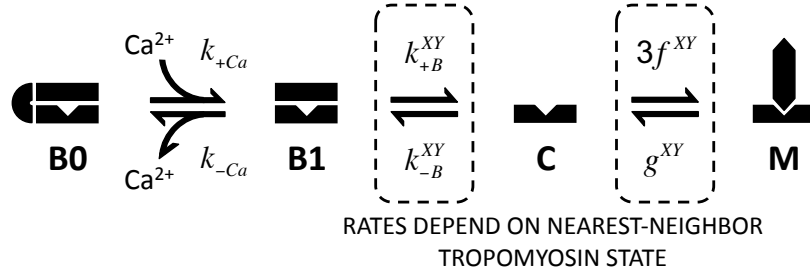


Figure 4.1: Scheme depicting individual regulatory-unit (RU) model. Each RU resides in one of four states depicting Ca^{2+} binding, tropomyosin (Tm) shifting, and myosin attachment. The $B1 \leftrightarrow C$ and $C \leftrightarrow M$ transition rates are functions of Tm states of the two neighboring RUs (X and Y). See text for details.

of the four signaling components (Figure 4.1). This may be thought of as a modification of the three-state Tm model [14] in which the blocked state (B) is partitioned into Ca^{2+} -free ($B0$) and Ca^{2+} -bound ($B1$) states. Binding of Ca^{2+} to the RU ($B0 \rightarrow B1$) is represented as a second-order process dependent on $[\text{Ca}^{2+}]$ and governed by the second order rate constant, k_{+Ca} . Ca^{2+} dissociation is determined by the rate constant k_{-Ca} . The transition between $B1$ and the closed state (C) is according to forward rate constant k_{+B} and the reverse rate k_{-B} . We assume that the transition between closed and open (M) states is rate-limited by activity of myosin S1, and accordingly assign this transition to be governed by the simplified XB-cycling rate constants f and g [18].

4.2.2 Representation of nearest-neighbor thin filament interactions

Individual RUs do not operate independently owing to structural connections with adjacent RUs along the thin filament [6]. This structural interaction inspired an early model by Hill and co-workers [19] and later several others [8, 16]. We represented these interactions by assuming that the free energy change required for the $B \leftrightarrow C$ transition of a single RU depends on nearest-neighbor RUs as follows:

$$\Delta G_{B \rightarrow C}^{XY} = \Delta G_{B \rightarrow C}^{ref} + \Delta G_{B \rightarrow C}^X + \Delta G_{B \rightarrow C}^Y$$

$\Delta G_{B \rightarrow C}^{ref}$ is the free energy change under reference conditions, which we chose as being those in which both neighbors are in the C state. $\Delta G_{B \rightarrow C}^X$ and $\Delta G_{B \rightarrow C}^Y$ represent additive contributions of either neighboring RU (having Tm states X and Y, respectively) to the free energy change. The notion underlying this formulation is that Tm-Tm coupling imposes additional energy change on transitions that result in neighboring RUs occupying dissimilar states. The equilibrium constant between C and B states, K_B^{XY} , may be expressed in terms of $\Delta G_{B \rightarrow C}^{XY}$ using the Gibbs relation:

$$K_B^{XY} = e^{-\Delta G_{B \rightarrow C}^{XY}/RT}$$

or alternatively as

$$K_B^{XY} = \gamma(XY) K_B^{ref}$$

where $K_B^{ref} = e^{-\Delta G_{B \rightarrow C}^{ref}/RT}$ and $\gamma(XY) = e^{-(\Delta G_{B \rightarrow C}^X + \Delta G_{B \rightarrow C}^Y)/RT}$. For convenience, we define the following cooperative coefficients:

$$\gamma_B = \left(e^{-\Delta G_{B \rightarrow C}^B/RT} \right)^{-1}$$

$$\gamma_M = e^{-\Delta G_{B \rightarrow C}^M/RT}$$

Using these definitions, $\gamma(XY)$ takes on the following neighbor-dependent values:

$$\gamma(BB) = \gamma_B^{-2}$$

$$\gamma(BC) = \gamma_B^{-1}$$

$$\gamma(BM) = \gamma_B^{-1} \gamma_M$$

$$\gamma(CC) = 1$$

$$\gamma(CM) = \gamma_M$$

$$\gamma(MM) = \gamma_M^2$$

Thus, when either coefficient is >1 , the system of interacting RUs is more tightly coupled and therefore more cooperative.

Analogously, the neighbor-dependent equilibrium constant between M and C states, K_M^{XY} , is

$$K_M^{XY} = K_M^{ref} \mu(XY)$$

with $\mu(XY)$ taking on values

$$\mu(BB) = \mu_B^{-2}$$

$$\mu(BC) = \mu_B^{-1}$$

$$\mu(BM) = \mu_B^{-1} \mu_M$$

$$\mu(CC) = 1$$

$$\mu(CM) = \mu_M$$

$$\mu(MM) = \mu_M^2$$

It can be shown that in order to satisfy microscopic reversibility in a system of interacting RUs and under the above assumptions, the constraint $\gamma_M = \mu_B$ must be applied. Thus, in the model the cooperative mechanisms represented by γ_M and μ_B are not independent.

For dynamic simulations, it is necessary to divide cooperative coefficients between forward and reverse rates. This is accomplished using the parameters r and q as follows:

$$k_{+B}^{XY} = k_{+B}^{ref} \gamma(XY)^q$$

$$k_{-B}^{XY} = k_{-B}^{ref} \gamma(XY)^{-(1-q)}$$

$$f^{XY} = f_{ref} \mu(XY)^r$$

$$g^{XY} = g_{ref} \mu(XY)^{-(1-r)}$$

4.2.3 Selection of model parameters

Four model parameter sets were used to represent different experimental systems and conditions (Table 4.1). The equilibrium constant of Ca^{2+} binding to TnC ($K_{Ca} = k_{+Ca}/k_{-Ca}$) was set at $0.8 \mu_M^{-1}$ based on recent FRET measurements in rat cardiac Tn.Tm complexes at 15°C [20]. We also chose baseline values of $k_{+Ca} = 0.09 \text{ ms}^{-1}$ and $k_{-Ca} = 0.113 \text{ ms}^{-1}$, based on the fastest phase of stopped-flow FRET data from the same study, these rates were increased for simulations of intact muscle at 22°C (Table 4.1, Set 4). Rates k_{+B}^{ref} and k_{-B}^{ref} were assumed to be very rapid relative to other rates [21]. The equilibrium constant K_B^{ref} ($k_{+B}^{ref}/k_{-B}^{ref}$) was adjusted in each parameter set for fixed values of K_M^{ref} (f^{ref}/g^{ref}) such that Ca^{2+} sensitivity of the response in question matched measured values. Rates f^{ref} and g^{ref} were scaled to match dynamic force responses.

The value of $\gamma_B = 10$ (Table 4.1, Set 1) was determined by matching thin filament Ca^{2+} binding predicted by the model with data obtained using fluorescently-labeled TnC in the absence of myosin [22], bovine Tm). This value corresponds with an energy change of 5.5 kJ/mol at 15°C . (Values of γ_M and μ_M were not used in Set 1 because of the absence of myosin.) A higher energy of 8.1 kJ/mol ($= 30$) was assumed in the remaining parameter sets, which were chosen to reproduce data in rat. In selecting values of γ_M and μ_M , we assumed $\gamma_B > \gamma_M > \mu_M$ as a general framework. This inequality was reasoned from the relative azimuthal positions of Tm on actin observed in structural studies [13], in which the difference between positions associated with B and C states was more than twice that between C and M (25° vs. 10°). Values of (4.7 kJ/mol) and (1.7 kJ/mol) were assumed accordingly. Model responses were not sensitive to q , and its value was set to 0.5 . It was initially assumed that neighbor status would affect XB attachment more than detachment, and r was set to 1.0 for all simulations. Simulations showing the other extreme ($r = 0$) are presented in Appendix C.

4.2.4 Simulations of coupled thin filament regulatory units

In a system of multiple interacting RUs, the model formulation requires explicit tracking of the Tm status of each RU in order to calculate transition rates

Table 4.1: Model parameter sets.

Set	k_{+Ca} ($\mu M^{-1}ms^{-1}$)	k_{-Ca} (ms^{-1})	k_{+B} (ms^{-1})	k_{-B} (ms^{-1})	f (ms^{-1})	g (ms^{-1})	γ_B	γ_M	μ_M	r	q
1	0.09	0.113	15	0.375	-	-	10	-	-	-	0.5
2	0.09	0.113	15	0.327	0.0028	0.0116	30	7	2	1	0.5
3	0.09	0.15	15	0.327	0.0025	0.0135	30	7	2	1	0.5
4	1	1.4286	2.5	0.0333	0.04	0.0686	30	7	2	1	0.5

(equations 19-22). Two approaches were used. In the first, we assumed that a given spatial arrangement of RUs in various Tm states constitutes a discrete energetic state of the entire thin filament. To make the problem tractable, we considered a shorter segment of nine adjacent RUs joined to form a ring, similar to the approach of Dobrunz *et al.* [23]. We improved the efficiency of this approach by collapsing degenerate states that arise from the ring arrangement, which yielded a Markov model containing 1219 unique states. Continuous-time solutions were obtained by solving the system of ordinary differential equations described by the Markov model. In the second approach, we used a Monte Carlo method to simulate responses in a full-length thin filament (26 RUs). This method allowed transition probabilities for each RU to be updated at every time step based on status of nearest-neighbors. Monte Carlo simulations were used to determine accuracy of and bypass certain limitations imposed by the ring simplification. Results presented below were obtained using the first method except where noted.

4.2.5 Additional Methods

Appendix C contains full details regarding development and implementation of solution methods. It also contains description of protocols and assumptions involved in simulating k_{tr} , the action of NEM-S1 fragments, presence of non-functional TnC, and TnC conformation.

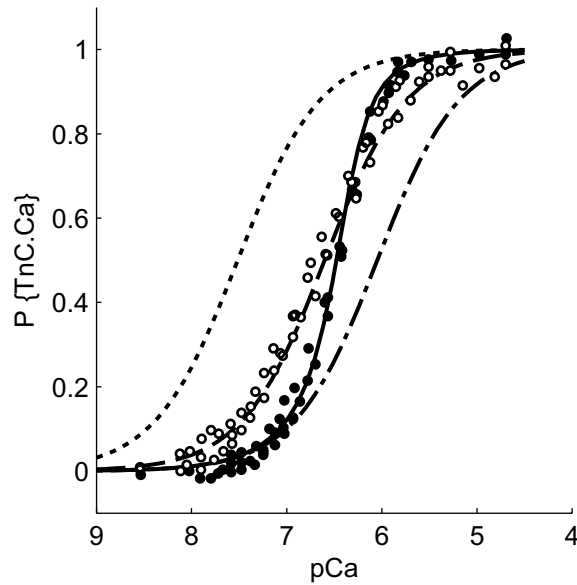


Figure 4.2: Nearest-neighbor coupling modifies thin filament Ca^{2+} binding. Fraction of regulatory-units with Ca^{2+} bound ($P\{TnC.Ca\}$) was assumed to equal normalized fluorescence intensity of labeled troponin C from experiments. Model parameters were adjusted such that $P\{TnC.Ca\}$ matched measurements in conventional, full-length filaments (filled circles, solid line is model). Using this parameter set, Ca^{2+} binding to mini thin filaments approximately one regulatory-unit in length (open circles) was modeled by assuming that filament capping proteins interacted with Tm ends to resemble nearest-neighbors in the BB (dash-dotted line), BC (dashed line), or CC (dotted line) configurations. The assumption of BC apparent nearest-neighbor conditions closely matched measurements ($R^2 = 0.900$). Data points digitized from ref. [22]. Parameter Set 1.

4.3 Results

4.3.1 Tm-Tm coupling alters Ca^{2+} binding properties of the thin filaments

We first tested the ability of the model to reproduce activation behavior in a simplified system. It was assumed the total fraction of RUs with bound Ca^{2+} corresponded with normalized fluorescence intensity from labeled TnC in normal and mini thin filaments one RU long [22]. A set of model parameters (Table 4.1, Set 1) were determined which reproduced data from full-length thin filaments ($R^2 = 0.92$, Figure 4.2). In mini thin filaments, Tm ends interacted with tropomodulin and troponin T-gelsolin fusion proteins used to cap F-actin, rather than neighboring Tm molecules. As the precise nature of these interactions is unknown, we considered the possibilities that Tm ends were constrained in a manner equivalent to BB, BC, or CC nearest-neighbor configurations. Fixing neighbor conditions to BC without changing any parameter values predicted Ca^{2+} binding to mini thin filaments with high fidelity ($R^2 = 0.90$, Figure 4.2).

4.3.2 Distinct roles of nearest-neighbor interactions in myofilament activation

A sensitivity analysis was constructed using various sets of cooperative coefficient values to evaluate the relative role of each coefficient in the Ca^{2+} dependence of force and the rate of force redevelopment following a rapid slack/re-stretch maneuver (k_{tr} (Figure 4.3). Interaction between cooperative coefficients and myosin binding was examined using low and high values of the effective crossbridge duty cycle (δ_{eff}), the steady-state fraction of RUs in the M state. Values of γ , f , and g were simultaneously adjusted for each combination of γ_B , γ_M , and μ_M such that half activation of force (pCa50) was 5.85, k_{tr} at pCa 4.5 was 9.5 s^{-1} , and δ_{eff} was either 0.25 or 0.75. The first two constraints derive from measured values [5] and provide a physiologically-relevant range of model responses. Fitted parameter values satisfying these constraints and complete sensitivity analysis results are

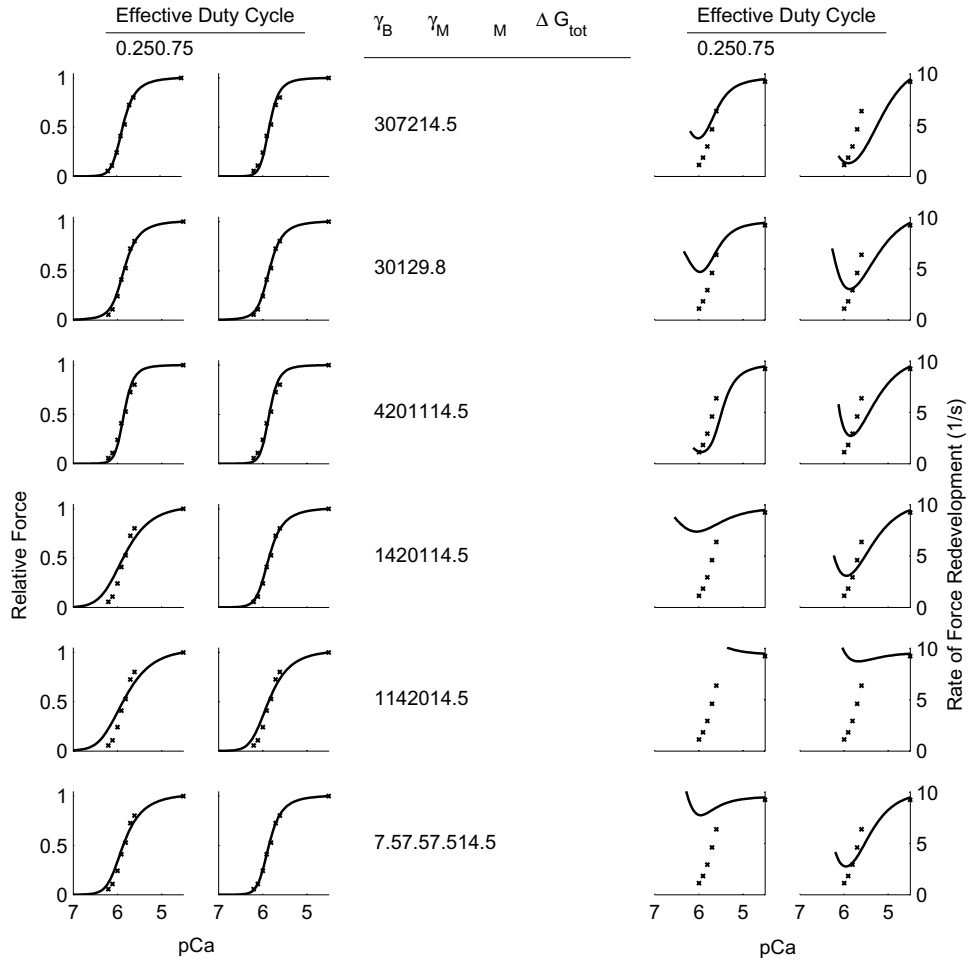


Figure 4.3: Different effects of cooperative coefficients γ_B , γ_M , and μ_M on Ca^{2+} sensitivities of force and the rate of force redevelopment (k_{tr}). Relations shown on the first row, effective duty cycle 0.25 were obtained using Parameter Set 2. The remaining panels show results from variations on this base parameter set. Corresponding values of γ_B , γ_M , and μ_M are given for each row of results along with ΔG_{tot} , the sum of absolute energy changes (kJ/mol) described by the given combination of cooperative coefficients. For each set of cooperative coefficients, the equilibrium constant and crossbridge kinetic rates f and g were adjusted simultaneously until half activation of force was pCa 5.85, effective crossbridge duty cycle was either 0.25 or 0.75, and k_{tr} at pCa 4.5 was 9.5 s^{-1} . Experimentally measured values from ref. [5] are repeated in each panel for comparison.

presented in Appendix C.

The baseline model response (Parameter Set 2) making use of the inequality $\gamma_B > \gamma_M > \mu_M$ exhibited strong Ca^{2+} dependence of k_{tr} , which was consistent with experiments. Increasing δ_{eff} to 0.75 slowed k_{tr} at low levels of activation, but shifted the k_{tr} -pCa relation to the right of the experimentally measured relation. The higher value of δ_{eff} was seen to have this effect regardless of the combination of cooperative coefficients used (Figure 4.3, left-most column).

Most parameter sets produced asymmetric steady-state force-pCa curves, wherein the Hill Coefficient of force at levels below half-maximal (n_1) is greater than that of force above half maximal (n_2). Setting γ_M to unity had a disproportionate effect on n_1 , independent of δ_{eff} (Figure 4.3, second row). In the absence of this interaction, n_1 was reduced from 3.64 to 2.76, while n_2 underwent a smaller change, from 2.35 to 2.19 ($\delta_{eff} = 0.25$). Removing γ_M also raised k_{tr} at low activation, showing that responses on that interval are particularly sensitive to this type of cooperative interaction.

We assessed relative potency of the three types of cooperative interactions by associating each in turn with the same absolute free energy change (Figure 4.3, rows 3-5). γ_B showed the highest cooperativity at both levels of δ_{eff} ($n_H = 4.0$ in both cases). γ_M and μ_M showed greater cooperativity at $\delta_{eff} = 0.75$ ($n_H = 2.76$ and 2.0 , respectively) than at $\delta_{eff} = 0.25$ ($n_H = 1.57$ and 1.52 , respectively), but in all cases were less cooperative than γ_B . γ_B was also sufficient on its own to introduce physiologic dependence of k_{tr} on pCa, while γ_M required $\delta_{eff} = 0.75$ to produce a similar effect. μ_M produced almost no pCa dependence of k_{tr} .

To test the inequality $\gamma_B > \gamma_M > \mu_M$, we distributed a total amount of free energy equivalent to that used in Parameter Set 2 equally among the three coefficients (Figure 4.3, row 6). Doing so reduced nH from 3.07 to 2.17 and attenuated dependence of k_{tr} on pCa ($\delta_{eff} = 0.25$ case).

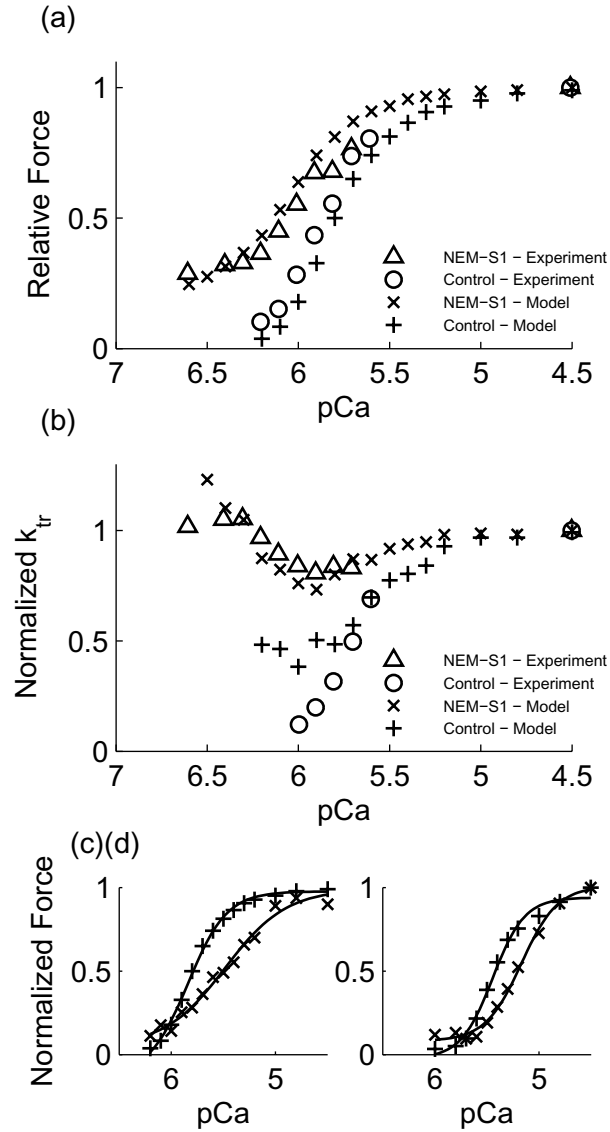


Figure 4.4: Model responses from spatially-explicit Monte Carlo simulations on full-length filaments containing 26 regulatory units. Each model data point was obtained from responses averaged across >1000 trials. (a) Effect of NEM-S1 on Ca^{2+} sensitivities of force and (b) the rate of force redevelopment (k_{tr} , normalized to values at pCa 4.5 for control (+) and NEM-S1 (x) conditions). Data from control (circles) and NEM-S1 (triangles) conditions digitized from ref. [5]. (c) Modeled effect of 50% non-functional TnC (x) on steady-state force-pCa relation compared with control (+). (d) Experimental measurements under the same conditions, digitized from ref. [24]. Each data series in (c) and (d) has been normalized to its maximum value. Parameter Set 2 was used for all simulations shown.

4.3.3 Effects of NEM-S1 on force-pCa and k_{tr} -pCa relations

Monte Carlo simulations of full-length filaments were used to examine effects of NEM-S1 binding at random to 10% of RUs. This caused a marked reduction in the Hill coefficient fit to points below half maximal force (from 3.15 to 1.68, compared with 4.72 to 1.54 in experiments) and shifted pCa₅₀ leftward from 5.80 to 6.03, compared with an experimentally recorded shift of 5.85 to 5.95 [5]. NEM-S1 blunted the activation dependence of k_{tr} , increasing k_{tr} at pCa 6.0 from 3.7 to 9.0 s⁻¹ (compared with 1.1 to 8.9 s⁻¹ in experiments). The model also predicted trends of steady-state force and k_{tr} over the entire range of pCa values which were in good agreement with the data (Figure 4.4 *a*, and *b*).

4.3.4 Effects of non-functional TnC on force-pCa relations and k_{tr}

Monte Carlo simulations were also used to assess the effects of randomly replacing varying fractions of TnC with mutant non-functional (non Ca²⁺ binding) TnC (xTnC, [24]). In the model, RUs containing xTnC were fixed in the B0 state. Levels of 25% and 50% xTnC reduced maximal Ca²⁺ activated force to 20% and 1% of control, respectively, compared with less extreme values of 71% and 28% seen experimentally. Conditions of 50% xTnC (Figure 4.4 *c* and *d*) reduced n_H of steady-state force from 2.3 to 1.5 (compared with 3.4 to 2.8 in experiments) and shifted half-activation rightward by 0.36 pCa units (0.2 in experiments). k_{tr} was not reduced below the control value at pCa 4.0 but was slowed to 5.0 s⁻¹ (down from 9.7 s⁻¹) by pCa 5.3. This is similar to experiments, which showed that 50% xTnC conditions slowed k_{tr} at sub-maximal activation.

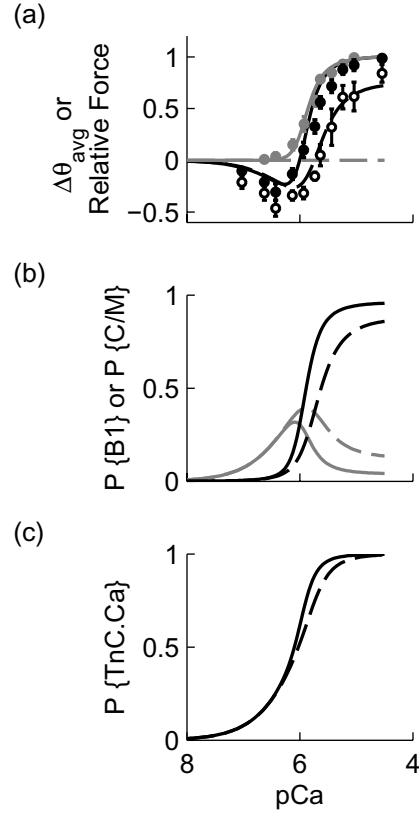


Figure 4.5: Effect of crossbridges on Ca^{2+} -dependence of TnC conformation. (a) Relative change in probe angle ($\Delta\theta_{avg}$) of labeled TnC was modeled under control conditions (solid line and circles) and during inhibition of crossbridge binding (dashed line and open circles). Relative force (shaded line and circles) also shown for comparison. Data points digitized from ref. [12], bars show \pm S.E. (b) Ca^{2+} -dependent occupancy of B1 (PB1) and C/M states (PC/M) under control (shaded and solid continuous traces, respectively) and crossbridge-inhibited conditions (shaded and solid dashed traces, respectively). (c) Ca^{2+} -dependent Ca^{2+} binding to TnC ($P\{\text{TnC.Ca}\}$) under control (continuous trace) and crossbridge-inhibited (dashed trace) conditions. Parameter Set 2.

4.3.5 Cooperative inhibition allows substantial TnC-Ca²⁺ binding without activating force

Tn state occupancy from the model was expressed as a relative average probe angle $\Delta\theta_{avg}$ and compared with rhodamine-labeled TnC experiments [12, 25]. The Ca²⁺-dependence of $\Delta\theta_{avg}$ was biphasic, resembling observations [12] (Figure 4.5 *a*). The transition from negative to positive $\Delta\theta_{avg}$ was concomitant with force in both model and experiments, with both showing substantial changes in $\Delta\theta_{avg}$ (-0.20 and -0.31, respectively) by pCa 6.4 (at which point force was less than 1% its maximum value) (Figure 4.5 *a*).

The effect of XB inhibition on the $\Delta\theta_{avg}$ -pCa relation was obtained by setting $f = 0$. This shifted the rising phase of the curve rightward and increased the magnitude of the negative phase, in good agreement with measurements made in the presence of vanadate [12] (Figure 4.5 *a*).

Tm-Tm coupling inhibited force at low [Ca²⁺]. At pCa 6.36, the force predicted by the model is less than 1% maximum even as >25% of TnC Ca²⁺ binding sites are occupied (Figure 4.5 *c*). As [Ca²⁺] is increased, RUs in the B1 state accumulate to a level sufficient to overcome cooperative inhibition, and activation becomes highly sensitive to [Ca²⁺] (Figure 4.5 *b*). In the presence of XB inhibitors, the model predicts that greater amounts of TnC.Ca²⁺ must accumulate before cooperative inhibition by Tm-Tm interaction is overcome (Figure 4.5 *b*). This may explain the larger magnitude of the negative phase of $\Delta\theta_{avg}$ observed experimentally in the presence of vanadate [12] (Figure 4.5 *a*).

4.3.6 XBs indirectly increase thin filament Ca²⁺ affinity

XB binding increased the total fraction of TnC sites occupied by Ca²⁺ ($P\{TnC.Ca\}$) between pCa 6.3 and 5.0, having maximal effect at pCa 5.81 where XBs increased $P\{TnC.Ca\}$ by 14% (Figure 4.5 *c*). At low [Ca²⁺], cooperative inhibition eliminates the effects of XBs on apparent Ca²⁺ affinity. XBs also have little effect on affinity at high [Ca²⁺] because at saturating concentrations Ca²⁺ binding alone is sufficient for activation.

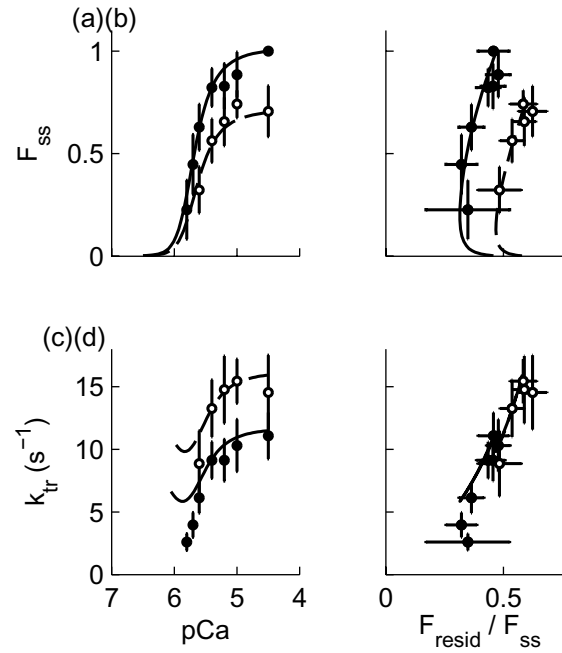


Figure 4.6: Effects of added Pi on Ca^{2+} dependencies of steady-state force, residual force following re-stretch (F_{resid}), and k_{tr} in skinned rat myocardial preparations. Each panel shows means of pooled data from control ($n = 13$ to 52 for different pCa values, solid circles) and 2.5 mM added Pi ($n = 6$ to 9 , open circles) \pm S.D. Also in each panel are model responses matching control (continuous traces) and added Pi (dashed traces). (a) Relative steady-state force (F_{ss}) as a function of pCa. (b) F_{ss} plotted against F_{resid}/F_{ss} . (c) k_{tr} as a function of pCa. (d) k_{tr} plotted against F_{resid}/F_{ss} . Parameter Set 3.

4.3.7 Thin filament cooperativity can account for effects of inorganic phosphate

Model predictions of the effects of inorganic phosphate (P_i) were compared with unpublished data from experiments described by Campbell [26]. After adjusting model parameters to match control responses (Table 4.1, Set 3), increasing the parameter g from 0.0135 to 0.0185 ms^{-1} in the model was sufficient to match the changes to steady-state force (F_{ss}) and k_{tr} measured under 2.5 mM added P_i . Elevating $[P_i]$ increased normalized residual tension following re-stretch (F_{resid}/F_{ss}) relative to control (Figure 4.6*b*). In the model, control F_{resid}/F_{ss} values were best fit by setting the duty cycle during re-stretch (δ_{rs} , described in §C.2.9) to 0.275. Fitting F_{resid}/F_{ss} values from the 2.5 mM $[P_i]$ set required a slight decrease in δ_{rs} to 0.25. The predicted k_{tr} - F_{resid}/F_{ss} relations (Figure 4.6*d*) were qualitatively similar to those observed.

4.3.8 Tm-Tm interactions potentiate the activating effects of XBs

In the absence of Tm-Tm interaction (γ_B , γ_M , and $\mu_M = 1$), Ca^{2+} -dependent activation (A_{Ca}) was greater than the XB-dependent component (A_{XB} , see caption to Figure 4.7) for all pCa (Figure 4.7 *b*). When Tm-Tm interactions were included (Figure 4.7 *e*, Parameter Set 2) peak A_{XB} exceeded A_{Ca} around pCa 5.95, near the value at which XBs had maximal influence on thin filament Ca^{2+} buffering. This demonstrates an interaction between XB-mediated recruitment of activation and structural coupling of RUs via Tm.

4.3.9 Model responses to time-varying $[\text{Ca}^{2+}]$ input

Model parameters were adjusted to reproduce steady-state force-pCa curves obtained during pharmacologically-slowed twitches in intact rat trabeculae at 22°C [23]. Without changing equilibrium constants, it was then possible to adjust kinetic rates such that twitch force in response to a measured Ca^{2+} transient agreed closely with measured twitch force ($R^2 = 0.846$, 5.6% RMS error) also from rat

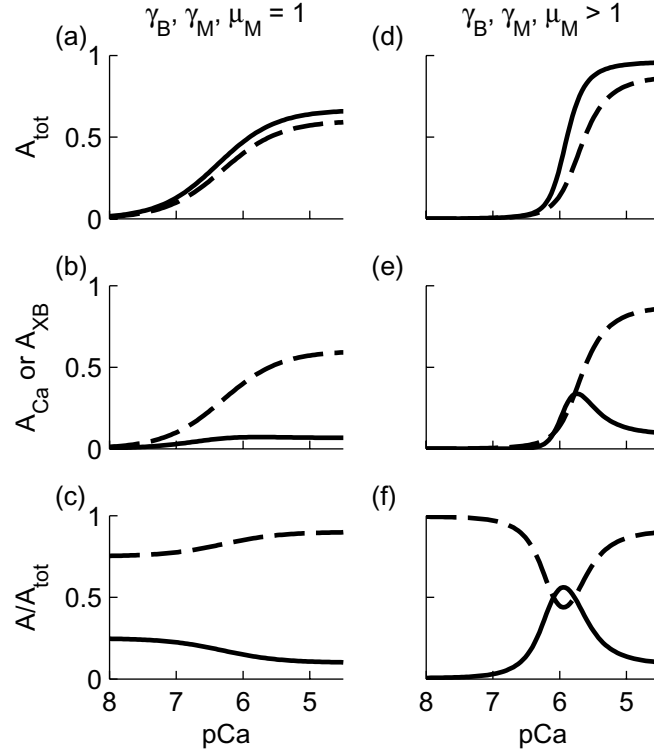


Figure 4.7: Tropomyosin-tropomyosin interactions potentiate crossbridge-dependent activation. The model was used to examine thin filament activation in the absence (γ_B , γ_M , and $\mu_M = 1$, panels *a-c*) and presence ($\gamma_B = 30$, $\gamma_M = 7$, and $\mu_M = 2$, panels *d-f*) of Tm-Tm interactions. (*a* and *d*) Total thin filament activation, defined as the sum of the fraction of RUs in C and M states (A_{tot}), in presence (continuous traces) and absence (dashed traces) of crossbridge binding. (*b* and *e*) Ca^{2+} -dependent activation (A_{Ca} , dashed traces) is equal to A_{tot} in the absence of crossbridges, the crossbridge-dependent component of activation (A_{XB} , solid traces) is $A_{tot} - A_{Ca}$. (*c* and *f*) Ca^{2+} and crossbridge components of activation normalized by A_{tot} at each pCa value (A_{Ca}/A_{tot} and A_{XB}/A_{tot} , dashed and dotted lines, respectively). A_{Ca}/A_{tot} as a function of pCa resembles corresponding k_{tr} -pCa relations. Parameter Set 2.

trabecula at 22°C and under constant sarcomere length (ref. [27], Table 4.1, Set 4). Driving the model with measured Ca^{2+} transients from the study of Dobrunz *et al.* [23] qualitatively recapitulated time courses of recorded twitches (Figure 4.8 *a*). Elapsed time from peak twitch force to 50% decay predicted by the model also agreed well with measured values.

4.3.10 Tm-Tm coupling and XB-binding synergistically enhance systolic and diastolic twitch function

In response to an idealized Ca^{2+} transient, loss of Tm-Tm coupling ($\gamma_B, \gamma_M, \mu_M = 1$) increased diastolic activation and reduced the time required to reach peak A_{tot} (Figure 4.8 *b*). Removal of XB binding ($f \approx 0$) reduced peak activation, shortened duration of the A_{tot} transient, and shortened time to peak A_{tot} (Figure 4.8 *b*). (See Table C.3.)

4.4 Discussion

The purpose of this work was to examine the role of Tm-Tm structural coupling in cardiac myofilament activation. We created a relatively simple model and an efficient new solution method to address this question. The model demonstrates that this single mechanism is capable of producing cooperative activation of force by Ca^{2+} and Ca^{2+} sensitivity of k_{tr} . The ability of the model to respond appropriately to simulations of added NEM-S1, added $[\text{P}_i]$, XB inhibition, and interruption of Tm-Tm interactions (in mini thin filaments) is supportive of a central role for Tm overlap in cardiac myofilament function. At the same time, certain discrepancies between modeled and measured responses suggest other important cooperative mechanisms at work that were not represented in the model.

Hoffman and Fuchs [4] reported that the amount of Ca^{2+} bound to the myofilaments is lowered by inhibiting force with vanadate. They postulated that XBs feed back cooperatively on Ca^{2+} binding, in turn recruiting additional XB attachment. This basic hypothesis motivated a number of models that rely on feedback to achieve cooperative activation [9, 10, 15]. Here, we reproduced the

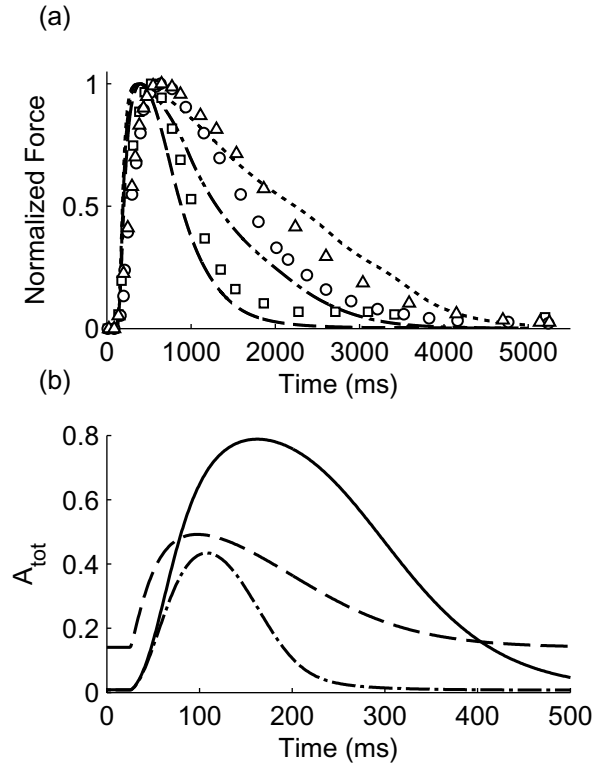


Figure 4.8: Model predictions of $[Ca^{2+}]$ -force dynamics in intact cardiac muscle and the effects of tropomyosin-tropomyosin interactions and crossbridges on twitch activation. (a) Model predicted twitch force in response to pharmacologically slowed Ca^{2+} transients digitized from ref. [23] in 3.0, 4.5, and 6.0 mM $[Ca]_o$ solutions (dashed, dash-dotted, and dotted lines, respectively), shown with measured twitches for comparison. (b) Total thin filament activation (A_{tot}) in response to an idealized Ca^{2+} transient under normal conditions (continuous trace), in the absence of Tm-Tm interactions (dashed trace), and in the absence of crossbridge binding (dash-dotted trace). Parameter Set 4.

observed effects of XBs on Ca^{2+} binding without any direct interaction between Ca^{2+} and force or Ca^{2+} and XBs in the model (compare our Figure 4.8 *b* with Figure 4.5 in [4]).

Studies of TnC conformation in contracting cardiac muscle as a function of Ca^{2+} concentration show an interval of positive probe angle change appearing to correspond with the rise of myofilament force [12, 25]. Both studies found that this phase persisted even in the presence of XB inhibitors, an effect reproduced by the model (Figure 4.5 *a*). Sun and co-workers [25] concluded that most of the cooperativity observed in the force-pCa relation can be accounted for by cooperativity intrinsic to the thin filament, without need of strongly-bound XBs. Mini thin filament results (Figure 4.2) demonstrate that at least part of that intrinsic thin filament cooperativity is due to Tm-Tm interactions.

In the model k_{tr} was nearly proportional to the fraction of steady-state activation attributed to Ca^{2+} binding to TnC (Figure 4.7 *f*, also see Figure C.7). This does not mean that the k_{tr} -pCa relation is determined solely by Ca^{2+} binding properties of TnC, because A_{Ca} is influenced by both Tm- and XB-related properties, most sensitively at intermediate pCa (~ 6.0 , see Figure 4.7). However, as Ca^{2+} reaches higher concentrations, it alone is nearly sufficient to activate the thin filament, causing A_{Ca} (and hence relative k_{tr}) to be essentially independent of myosin activity. This is consistent with the observation that myosin regulatory light chain phosphorylation in skinned rat myocardium increased the Ca^{2+} sensitivity of steady-state force without altering the k_{tr} -pCa relation [28].

Model results further suggest that a common mechanism underlies Ca^{2+} dependencies of F_{ss} , k_{tr} , and F_{resid} . The model reproduced our measured changes of all three quantities under added Pi when we changed two parameters (g and δ_{rs}), both of which should be $[\text{P}_i]$ sensitive. This result suggests a simple correspondence between model parameters and effects of XBs on myofilament activation.

After showing that the same model can be used to reproduce experimental observations in both skinned and intact preparations, we used it to illustrate the unique contributions of Tm-Tm coupling and XB-based thin filament activation on myocardial twitch dynamics (Figure 4.8). Their combined effects appear to be

(1) to delay the development of peak tension, (2) to increase peak activation, and (3) to prolong twitch duration (Figure 4.8 *b*). The overall result is a temporal decoupling of Ca^{2+} transient time course from twitch dynamics, allowing force to develop at a much slower rate than Ca^{2+} release and Ca^{2+} reuptake to be slower than force relaxation.

Tm-Tm coupling also acts independently to inhibit development of tension at diastolic $[\text{Ca}^{2+}]$. It is within this context that the distinction between cooperative activation only (i.e. via positive feedback, [9, 10]) and combined cooperative inhibition/activation may be important. Our model suggests that any change lessening the strength of Tm-Tm coupling could raise diastolic tension owing to loss of cooperative inhibition at those Ca^{2+} levels (Figure 4.8). The phenotype of extreme diastolic dysfunction observed in transgenic mice expressing the FHC-causing E180G Tm mutation [29] may be explained at least in part by this mechanism. It is interesting that a common feature among various perturbations to Tm in cardiac muscle is altered contractile dynamics [29, 30], considering that kinetic transitions between Tm states are generally thought to be rapid relative to other events [21]. The present model illustrates the effects Tm-Tm coupling can have on twitch dynamics and may be relevant to these unexplained findings.

The ODE implementation of the model reproduced brute-force simulations with high accuracy and a nearly 10,000 fold speedup in time course simulations (see comparison in §??). It thereby achieves efficiency without producing complications observed in some mean-field models such as hysteresis in the force-pCa relation and other non-physiological properties [8, 11]. For example, the model of Razumova *et al.* [31] suggested that RU-RU interaction produces steady-state force-pCa curves with the property , which they saw as being characteristic of this type of cooperativity. Meanwhile, models employing this same mechanism but with explicit representation of each RU (including the present model) actually give the opposite asymmetry, showing that RU-RU cooperativity leads to the physiological [8, 16].

Some have suggested that nearest-neighbor interactions are not of primary importance in cooperativity of the cardiac myofilaments. Gillis *et al.* [24] reasoned

that 50% replacement of functioning TnC with xTnC would isolate remaining functional RUs and abolish cooperative effects due to nearest-neighbor interactions, if present. When no change in n_H of the force-pCa relation and continued dependence of k_{tr} on Ca^{2+} were observed under these conditions, they concluded that these properties could not be explained by nearest-neighbor interactions. In the model, some cooperativity and Ca^{2+} dependence of k_{tr} was retained at 50% xTnC content. This behavior was due to the fact that randomly distributed xTnC in the filaments placed only 27% of functional TnC in an isolated configuration (both neighbors containing xTnC). The remainder were arranged in functional islands of size two RUs and greater which interacted to produce cooperative behavior similar to that seen in normal conditions. These results illustrate a plausible means by which Tm-Tm interactions could contribute to the measured phenomena.

4.4.1 Model limitations and additional forms of cooperativity

The aspects of the non-functional TnC experiments that were poorly reproduced by the model may be informative in that they suggest presence of additional mechanisms of cooperativity not depicted here. The same may be said of the systematic overestimation of k_{tr} at low activation (e.g. Figure 4.3, row 1). We have considered the thin filament at the resolution of individual RUs, whereas more detailed models have considered regulation of each actin binding site [16, 32], and ascribed cooperative behavior of the thin filament to interactions at that scale. One of these, the model of Smith & Geeves [16], is based on the widely accepted idea that adjacent Tm molecules behave more like a continuous flexible chain than rigid, interacting units. Certain behaviors produced by their model, including asymmetry in the force-pCa curve and XB-dependent thin filament Ca^{2+} binding, are also produced by the model we present here. Still, the present approach limits the description of Tm position to a single, generalized point every seventh actin monomer and cannot be used to examine contributions intra-RU cooperative events in a direct way.

An additional limitation of the model is that it applies only to isometric

conditions, specifically to a sarcomere length at which thick and thin filaments are fully overlapping. The current approach also neglects the effects of filament compliance, which is thought to enhance the overall number of attached XBs [33]. In the context of strong Tm-Tm coupling, which potentiates the activating effects of XBs (Figure 4.7), this may take on added significance. Future work integrating the two mechanisms is therefore likely to be worthwhile.

Acknowledgments

We wish to acknowledge one of the reviewers for suggesting an energetic interpretation of cooperative coefficients used in formulation of the model. This study was supported by an American Heart Association Predoctoral Fellowship (to S.G.C.), the National Biomedical Computation Resource (NIH grant P41 RR08605, to A.D.M), and the National Science Foundation (BES-0506252, to A.D.M). This investigation was conducted in part using a facility constructed with support from Research Facilities Improvement Program Grant Number C06 RR-017588-01 from the National Center for Research Resources, National Institutes of Health.

Chapter 4, in full, is a reprint of the published article “Coupling of Adjacent Tropomyosins Enhances Crossbridge Mediated Cooperative Activation in a Markov Model of the Cardiac Thin filament.” Campbell S.G., Lionetti F.V., Campbell K.S., and McCulloch A.D. *Biophysical Journal*. 98, 2010. The dissertation author was the primary investigator and author of this paper.

Model predictions of $[Ca^{2+}]$ -force dynamics in intact cardiac muscle and the effects of tropomyosin-tropomyosin interactions and crossbridges on twitch activation. (a) Model predicted twitch force in response to pharmacologically slowed Ca^{2+} transients digitized from ref. [23] in 3.0, 4.5, and 6.0 mM $[Ca]_o$ solutions (dashed, dash-dotted, and dotted lines, respectively), shown with measured twitches for comparison. (b) Total thin filament activation (A_{tot}) in response to an idealized Ca^{2+} transient under normal conditions (continuous trace), in the absence of Tm-Tm interactions (dashed trace), and in the absence of crossbridge binding (dash-dotted trace). Parameter Set 4.

References

- [1] Tardiff, J.C., 2005. Sarcomeric proteins and familial hypertrophic cardiomyopathy: linking mutations in structural proteins to complex cardiovascular phenotypes. *Heart Failure Rev*, 10:237–48.
- [2] Landstrom, A.P., Parvatiyar, M.S., Pinto, J.R., Marquardt, M.L., Bos, J.M., Tester, D.J., Ommen, S.R., Potter, J.D., and Ackerman, M.J., 2008. Molecular and functional characterization of novel hypertrophic cardiomyopathy susceptibility mutations in TNNC1-encoded troponin C. *Journal of molecular and cellular cardiology*, 45:281–8.
- [3] Gordon, A.M., Homsher, E., and Regnier, M., 2000. Regulation of contraction in striated muscle. *Physiol Rev*, 80:853–924.
- [4] Hofmann, P.A. and Fuchs, F., 1987. Evidence for a force-dependent component of calcium binding to cardiac troponin C. *Am J Physiol*, 253:C541–6.
- [5] Fitzsimons, D.P., Patel, J.R., and Moss, R.L., 2001. Cross-bridge interaction kinetics in rat myocardium are accelerated by strong binding of myosin to the thin filament. *J Physiol (Lond)*, 530:263–72.
- [6] McLachlan, A.D. and Stewart, M., 1975. Tropomyosin coiled-coil interactions: evidence for an unstaggered structure. *J Mol Biol*, 98:293–304.
- [7] Pan, B.S., Gordon, A.M., and Luo, Z.X., 1989. Removal of tropomyosin overlap modifies cooperative binding of myosin S-1 to reconstituted thin filaments of rabbit striated muscle. *J Biol Chem*, 264:8495–8.
- [8] Rice, J.J. and de Tombe, P.P., 2004. Approaches to modeling crossbridges and calcium-dependent activation in cardiac muscle. *Prog Biophys Mol Biol*, 85:179–95.
- [9] Landesberg, A. and Sideman, S., 1994. Mechanical regulation of cardiac muscle by coupling calcium kinetics with cross-bridge cycling: a dynamic model. *Am J Physiol*, 267:H779–95.
- [10] Campbell, K., 1997. Rate constant of muscle force redevelopment reflects cooperative activation as well as cross-bridge kinetics. *Biophys J*, 72:254–62.
- [11] Rice, J., Tu, Y., Poggesi, C., and Tombe, P.D., 2007. Spatially-compressed Cardiac Myofilament Models Generate Hysteresis that is not Found in Real Muscle. *Pacific Symposium on Biocomputing 2008: Kohala Coast, Hawaii, USA, 4-8 January 2008*, 13:366–377.

- [12] Bell, M.G., Lankford, E.B., Gonye, G.E., Ellis-Davies, G.C.R., Martyn, D.A., Regnier, M., and Barsotti, R.J., 2006. Kinetics of cardiac thin-filament activation probed by fluorescence polarization of rhodamine-labeled troponin C in skinned guinea pig trabeculae. *Biophys J*, 90:531–43.
- [13] Vibert, P., Craig, R., and Lehman, W., 1997. Steric-model for activation of muscle thin filaments. *J Mol Biol*, 266:8–14.
- [14] McKillop, D.F. and Geeves, M.A., 1993. Regulation of the interaction between actin and myosin subfragment 1: evidence for three states of the thin filament. *Biophysical Journal*, 65:693–701.
- [15] Robinson, J.M., Wang, Y., Kerrick, W.G.L., Kawai, R., and Cheung, H.C., 2002. Activation of striated muscle: nearest-neighbor regulatory-unit and cross-bridge influence on myofilament kinetics. *J Mol Biol*, 322:1065–88.
- [16] Smith, D.A. and Geeves, M.A., 2003. Cooperative regulation of myosin-actin interactions by a continuous flexible chain II: actin-tropomyosin-troponin and regulation by calcium. *Biophys J*, 84:3168–80.
- [17] Tregear, R.T., Reedy, M.C., Goldman, Y.E., Taylor, K.A., Winkler, H., Franzini-Armstrong, C., Sasaki, H., Lucaveche, C., and Reedy, M.K., 2004. Cross-bridge number, position, and angle in target zones of cryofixed isometrically active insect flight muscle. *Biophys J*, 86:3009–19.
- [18] Brenner, B., 1988. Effect of Ca^{2+} on cross-bridge turnover kinetics in skinned single rabbit psoas fibers: implications for regulation of muscle contraction. *Proc Natl Acad Sci USA*, 85:3265–9.
- [19] Hill, T.L., Eisenberg, E., and Greene, L., 1980. Theoretical model for the cooperative equilibrium binding of myosin subfragment 1 to the actin-troponin-tropomyosin complex. *Proc Natl Acad Sci USA*, 77:3186–90.
- [20] Dong, W.J., Jayasundar, J.J., An, J., Xing, J., and Cheung, H.C., 2007. Effects of PKA phosphorylation of cardiac troponin I and strong crossbridge on conformational transitions of the N-domain of cardiac troponin C in regulated thin filaments. *Biochemistry*, 46:9752–61.
- [21] Geeves, M.A. and Lehrer, S.S., 1994. Dynamics of the muscle thin filament regulatory switch: the size of the cooperative unit. *Biophysical Journal*, 67:273–82.
- [22] Gong, H., Hatch, V., Ali, L., Lehman, W., Craig, R., and Tobacman, L.S., 2005. Mini-thin filaments regulated by troponin-tropomyosin. *Proc Natl Acad Sci USA*, 102:656–61.

- [23] Dobrunz, L.E., Backx, P.H., and Yue, D.T., 1995. Steady-state $[Ca^{2+}]_i$ -force relationship in intact twitching cardiac muscle: direct evidence for modulation by isoproterenol and EMD 53998. *Biophys J*, 69:189–201.
- [24] Gillis, T.E., Martyn, D.A., Rivera, A.J., and Regnier, M., 2007. Investigation of thin filament near-neighbour regulatory unit interactions during force development in skinned cardiac and skeletal muscle. *J Physiol (Lond)*, 580:561–76.
- [25] Sun, Y.B., Lou, F., and Irving, M., 2009. Calcium- and myosin-dependent changes in troponin structure during activation of heart muscle. *J Physiol (Lond)*, 587:155–63.
- [26] Campbell, K.S. and Holbrook, A.M., 2007. The rate of tension recovery in cardiac muscle correlates with the relative residual tension prevailing after restretch. *Am J Physiol Heart Circ Physiol*, 292:H2020–2.
- [27] Janssen, P.M. and Tombe, P.P.D., 1997. Uncontrolled sarcomere shortening increases intracellular Ca^{2+} transient in rat cardiac trabeculae. *Am J Physiol*, 272:H1892–7.
- [28] Olsson, M., Patel, J., Fitzsimons, D., Walker, J., and Moss, R., 2004. Basal myosin light chain phosphorylation is a determinant of Ca^{2+} sensitivity of force and activation dependence of the kinetics of myocardial force development. *American Journal of Physiology- Heart and Circulatory Physiology*, 287:H2712.
- [29] Prabhakar, R., Boivin, G.P., Grupp, I.L., Hoit, B., Arteaga, G., Solaro, J.R., and Wieczorek, D.F., 2001. A familial hypertrophic cardiomyopathy alpha-tropomyosin mutation causes severe cardiac hypertrophy and death in mice. *Journal of molecular and cellular cardiology*, 33:1815–28.
- [30] Jagatheesan, G., Rajan, S., Petrashevskaya, N., Schwartz, A., Boivin, G., Vahabi, S., DeTombe, P., Solaro, R.J., Labitzke, E., Hilliard, G., and Wieczorek, D.F., 2003. Functional importance of the carboxyl-terminal region of striated muscle tropomyosin. *J Biol Chem*, 278:23204–11.
- [31] Razumova, M.V., Bukatina, A.E., and Campbell, K.B., 2000. Different myofilament nearest-neighbor interactions have distinctive effects on contractile behavior. *Biophysical Journal*, 78:3120–37.
- [32] Tobacman, L.S. and Butters, C.A., 2000. A new model of cooperative myosin-thin filament binding. *J Biol Chem*, 275:27587–93.
- [33] Tanner, B., Daniel, T., and Regnier, M., 2007. Sarcomere lattice geometry influences cooperative myosin binding in muscle. *PLoS Comput Biol*, 3:e115.

Chapter 5

Regulatory Light Chain

Phosphorylation in the Intact

Myocardium

5.1 Introduction

Myosin regulatory light chain (RLC) is a ~ 20 kDa protein that associates with and mechanically stabilizes the neck region of myosin heavy chain [1]. In skinned, constantly activated cardiac muscle preparations, RLC phosphorylation by myosin light chain kinase (MLCK) increases Ca^{2+} sensitivity and maximally-activated tension [2]. RLC phosphorylation has also been shown to accelerate delayed tension response to rapid stretch (stretch activation) in skinned mouse myocardium [3]. Electron microscopy studies on isolated skeletal muscle thick filaments have shown that phosphorylation of RLC allows myosin heads to displace further from the thick filament backbone [4], contributing to the long-standing hypothesis that the principal effect of RLC phosphorylation in striated muscle is to increase probability of actin-myosin crossbridge formation [1, 3].

The importance of RLC phosphorylation in the regulation of heart function is evident from its connection to certain forms of heart disease. Davis and co-workers [5] identified a gain-in-function mutation to MLCK in patients with

a variant form of familial hypertrophic cardiomyopathy (FHC). Another study demonstrated that FHC-linked mutations to RLC alter the extent of its phosphorylation by MLCK [6]. Various studies have been performed with a transgenic mouse line expressing mutant RLC in which 3 phosphorylatable serines were mutated to alanine [7–9]. Hearts in these mice were dilated, and functional studies of myocardial tissue revealed depressed contractile function, myofilament Ca^{2+} sensitivity, and reduced responsiveness to β -adrenergic stimulation.

Another possible role for RLC phosphorylation in the heart is suggested by the presence of phosphorylation gradients in the left ventricular myocardium, first reported by Davis *et al.* [5] and subsequently by others [10, 11]. Elevated levels of RLC phosphorylation in the epicardial and apical regions of the LV are hypothesized to regulate ventricular wall deformation, particularly torsion or twisting motion observed during the cardiac cycle [5].

While these results demonstrate the importance of RLC phosphorylation in heart muscle, its effects on intact cardiac muscle behavior as well as the specific molecular mechanisms that may explain them are still poorly understood. The study of intact cardiac muscle presents several challenges including time-varying Ca^{2+} concentrations and limited options for introducing specific molecular-level perturbations (e.g. to RLC phosphorylation). To address these challenges, we have developed a gene-targeted knock-in mouse in which the endogenous *Mlc-2v* gene has been replaced by one coding for mutant RLC lacking phosphorylatable serines at residues 14 and 15. Ca^{2+} transients and twitch tension were measured simultaneously in right ventricular papillary muscles isolated from these mice and analyzed using a novel computational model capable of accounting for the complex processes underlying transient activation of the myofilaments by Ca^{2+} . This analysis suggested specific alterations to myosin crossbridge function mediated by RLC phosphorylation which, when included in a computational model of left ventricular mechanics, were capable of explaining altered ventricular torsion measured in mutant mice.

5.2 Methods

5.2.1 Generation of gene-targeted mouse lines

Mlc-2v genomic DNA was isolated from a 129-SV/J mouse genomic DNA library, as previously described [12]. PCR-based mutagenesis was used to introduce (*i*) a single mutation (SM) of T to G in codon 15 as well as (*ii*) a double mutation (DM) from AG to GC in codon 14 and from T to G in codon 15 to generate targeted alleles for SM and DM mice, respectively. The SM changed codon 15 from Ser to Ala and simultaneously abolished a SstI site, whereas the DM changed codon 14 and 15 from Ser to Ala and also simultaneously abolished a SstI site. A pGKneo-tk cassette flanked by two loxP sites was inserted into intron 2 as a selectable marker in both targeted alleles such that it could subsequently be deleted by Cre mediated recombination. The linearized targeting constructs were electroporated into R1 ES cells. For SM mice, a total of 30 G418 resistant colonies screened, 14 were identified as homologous recombinants by Southern blot hybridization analysis of ES cell genomic DNA. Three of the fourteen colonies were injected into C57/B6 blastocysts, all three resulting in the generation of chimeras, one of which displayed germ line transmission. To avoid the interference of the pGKneo-tk cassette with expression of the Ser15 to Ala15 allele, the cassette was deleted by crossing the heterozygous mice with protamine cre transgenic mice, which express Cre recombinase in the male germ line [13].

5.2.2 Measurement of Ca^{2+} -contraction dynamics in RV papillary muscles

All procedures were performed in accordance with protocols approved by the Institutional Animal Care and Use Committee of the University of California, San Diego. All muscles were isolated from 5-7 week old male and female DM mice and control C57-B1/6 mice (Charles River Laboratories). Animals were anesthetized with inhaled isoflurane and euthanized by cervical dislocation, after which hearts were rapidly excised, cannulated, and perfused with a high-[K+] modified Krebs-

Henseleit solution (described below) containing 20 mM 2,3-BDM and bubbled with a mixture of 95% O₂/5% CO₂. An unbranched right-ventricular papillary muscle was selected when present and removed under continuous perfusion, leaving a large block of septal wall attached on one end, and a portion of the tricuspid valve attached to the other. Muscles were then placed in a temperature-controlled, 1.7 ml muscle bath (801C, Aurora Scientific, Inc.) mounted on an inverted microscope (Nikon Eclipse TE300). The septal wall end of the muscle was attached to a force transducer (model 405A, Aurora Scientific, Inc.) through a platinum wire basket. The valve end was attached to a hook at the end of a high-speed, servo-controlled lever arm (model 322C, Aurora Scientific, Inc.). With the muscle in position, the muscle was superfused with oxygenated modified Krebs-Henseleit solution at a rate of 3-5 volume exchanges per minute. The muscle was allowed to equilibrate for 10-20 minutes while being paced at 1 Hz using platinum electrodes positioned along the sides of the bath.

After initial equilibration the muscle was stretched by ~20% to achieve an approximate mean sarcomere length of 2.2 μm . Titanium dioxide particles applied to the muscle prior to mounting were used to measure and adjust stretch at a centrally-located segment of the papillary muscle. After setting the muscle at optimal length, the top and side aspects of the muscle were photographed (using a prism placed in the bath) for determination of the muscle's cross sectional area. Subsequently pacing was increased to either 2 Hz (25°C protocol) or 5 Hz (37°C protocol), and the muscle was allowed to equilibrate for an additional 20-30 minutes.

Perfusion was then stopped and the bathing solution replaced with a loading solution containing the membrane-permeable fluorescent Ca²⁺ indicator Fura-2AM (2 μM final concentration, Invitrogen, Inc.). The muscle was allowed to load at room temperature for 25-30 minutes, after which the bath temperature was set to its corresponding value (25 or 37°C) and perfusion and pacing were resumed.

Muscles were imaged using an extra-long working distance 20X objective. Ratiometric measurement of Fura-2 fluorescence was accomplished by illuminating the muscle with rapidly alternating (333 Hz) 340/380 nm light. Excitation wave-

length switching was performed using a fast filter switcher (Lambda DG-4, Sutter Instrument, Inc.). Fura-2 emission (~ 540 nm) was then filtered and measured with a photomultiplier tube system (PMT-100, Applied Scientific Instrumentation).

Integration of the control and measurement systems for the apparatus was handled by a Data Acquisition Processor (5216a, Microstar Laboratories, Inc.) running custom programs. Experimental protocols, including patterns of pacing and length perturbations, were designed and run using custom software running on the host PC.

Papillary muscle preparations were excluded which exhibited excessive run-down or large increases in resting tension over the course of the protocol, which typically lasted ~ 90 minutes including Fura-2 loading. For the 37°C protocol, preparations exhibiting excessive leakage of Fura-2 dye (seen as a loss in Ca^{2+} sensitive fluorescent signal) were not included in Ca^{2+} transient analysis at that temperature, but twitch tension data were still used in the absence of other exclusions.

5.2.3 Solutions

The modified Krebs-Henseleit solutions contained (in mM): NaCl, 141; NaHCO_3 , 25; dextrose, 10; CaCl_2 , 2; NaH_2PO_4 , 1.2; KCl, 5; MgSO_4 , 1; HEPES, 5. For arrest solution, KCl concentration was increased to 25 mM, and BDM (20 mM) and heparin (10 units/ml) were added.

5.2.4 Markov model of myofilament force production

The Markov model of myofilament activation described in Chapter 4, with some modifications, was used to relate steady-state and time-varying Ca^{2+} concentration to myofilament force. Changes to the model are described in detail in Appendix ?? and depicted schematically in Figure 5.1. Briefly, the 'open' state (M) of the original model was split into two states, M_{pr} and M_{po} , representing pre- and post-powerstroke states of the myosin crossbridge cycle. Rate constants for crossbridge attachment (f), detachment from pre-powerstroke state (g), forward powerstroke (h_f), reverse powerstroke (h_b), and detachment from post-powerstroke

state (g_{xb}) were taken from the model of Rice and co-workers [14]. Additionally, rate dependence of tropomyosin shifting on the status of nearest-neighbor regulatory units was limited to the $B1 \leftrightarrow C$ transition, as this was the most critical in reproducing myofilament behavior (see Chapter 4).

All simulations assumed constant sarcomere length, meaning that force is produced in proportion to the occupancy of the M_{po} state. Tension produced by the model was calculated as the product of individual crossbridge stiffness (k_{xb}), crossbridge distortion induced by the powerstroke (x_0), and the number of attached, post-powerstroke myosin heads [M_{po}]:

$$P = k_{xb}x_0[M_{po}]$$

The value of k_{xb} was set to 18.8 kPa/nm in order to match mean peak twitch tension at 2 Hz pacing frequency at 25°C bath temperature. Values for all other parameters are shown in Table 5.1. Parameters not described in this section were introduced previously in Chapter 4.

5.2.5 Model representation of RLC phosphorylation

Five model parameters, f , h_f , h_b , g_{xb} , and x_0 , were identified as potentially dependent on RLC phosphorylation. In order to conveniently summarize RLC phosphorylation-based changes to these parameters, the final value of each was re-calculated in the following generic format:

$$k_{final} = k_{base} (1 + p_k Q_{RLCP}),$$

where k represents one of the five model parameters, p_k is the corresponding RLC-P weighting coefficient, and Q_{RLCP} is a representation of RLC phosphorylation level. Thus, values of the five RLC-P weighting coefficients (Table 5.1) describe the sensitivity of corresponding parameters to Q_{RLCP} .

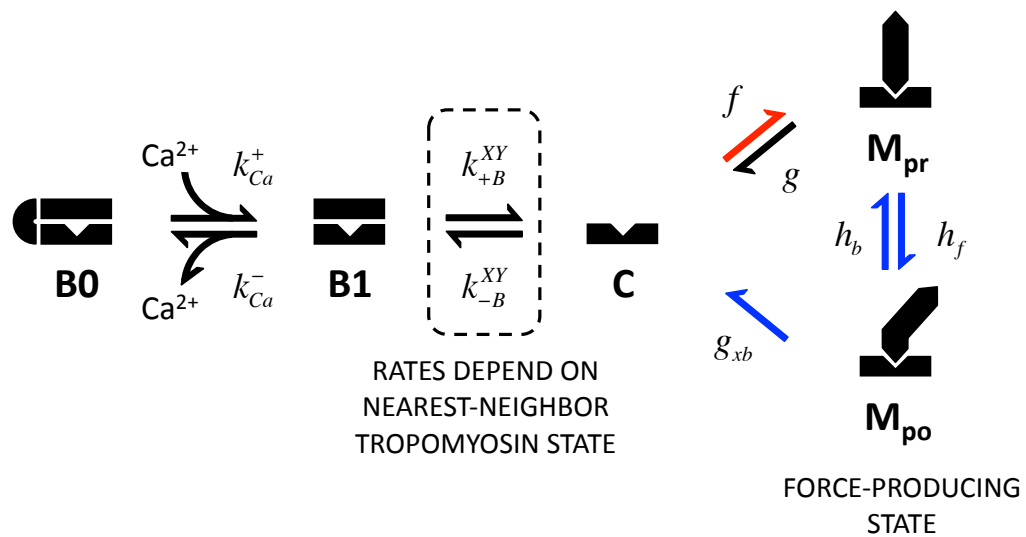


Figure 5.1: Diagram of simplified Markov myofilament activation model with 3-state crossbridge cycle. The model is based upon that described in Chapter 4, but has been simplified to contain only one neighbor-dependent pair of rate constants (for the $B1 \leftrightarrow C$ transition). At the same time, the 2-state crossbridge model used in Chapter 4 has been expanded to include pre-powerstroke (M_{pr}) and post-powerstroke (M_{po}) states for myosin binding. Rate constants hypothesized to be affected by RLC phosphorylation are indicated by red (Hypothesis 1, see text) and blue arrows (Hypothesis 2). See text for description of rate constants.

5.2.6 MRI protocol and methods

In vivo murine cardiac imaging was performed on a 7T horizontal-bore MR scanner (Varian magnet with a Buker console), equipped with a 21 cm bore. Mice were anesthetized with isoflurane and imaged in a 2.5 cm Bruker volume coil. Body temperature and the electrocardiogram were also monitored. Heart rate was maintained around 400 BPM. Cine anatomical imaging was performed using the Fast Low Angle Shot sequence (FLASH) with flip angle = 15° , echo time = 2.8 ms, repetition time = 6 ms, data matrix = 128 x 128, field of view = 2.0 cm, slice thickness = 1 mm, and 4 averages. Myocardial tagging was performed using spatial modulation of magnetization (SPAMM) [15]. The tag thickness was 0.3 mm and tag line separation was 0.7 mm, which allowed for 2-3 taglines to be placed across the ventricular wall of the mouse heart. Parameters for the image acquisition were the same as the cine acquisition except for the inclusion of the tagging module and the number of averages was increased to 20. During imaging, the long axis of the left ventricle was first identified. Both cine and SPAMM tagged short axis images were then taken at the base and apex of the left ventricle. 6 wk old WT and mutant littermates were scanned (n=3 for each group). For one mouse, the total imaging time was approximately 30 minutes.

5.2.7 Torsion Analysis

Tag intersections near the epicardium of the LV free wall are tracked from end diastole to end systole in the basal and apical slice. Torsion was calculated as the circumferential angular displacement between two points, one near the base and one near the apex, normalized by the vertical distance separating them [16]. All measured values are reported as the mean \pm S.E.M.

5.2.8 Multi-scale model of left ventricular mechanics

We used a finite element model of the mouse left ventricle (LV) to examine the effects of RLC phosphorylation on ventricular torsion (Figure 5.2). LV geometry was approximated as a thick-walled, truncated ellipse of revolution whose

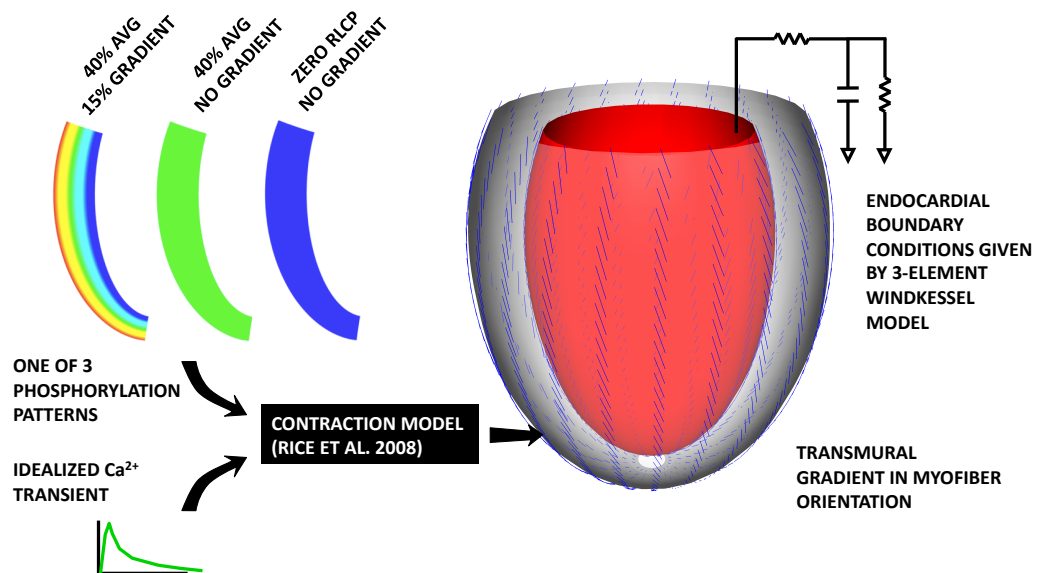


Figure 5.2: Scheme for modeling effects of RLC phosphorylation on left ventricular mechanics. The recent Ca^{2+} -contraction coupling model of Rice *et al.* [14], which includes velocity and length-dependent mechanisms, was modified to include hypothesized effects of RLC phosphorylation level on crossbridge kinetics. The altered model was embedded within a simplified model of mouse LV geometry that included reported values of myofiber orientation [17]. The systolic phase was simulated by driving the Rice model with an idealized Ca^{2+} transient and causing the ventricle to eject against a realistic afterload [18]. This integrated model was used to predict the effects of spatial gradients in phosphorylation on hemodynamic function and movement of the ventricle during ejection.

dimensions (wall thickness, focal length, and end-diastolic volume) were based on MR-derived anatomical data obtained as a part of this study. A transmural pattern of myofiber orientation was assumed based on published gradients in the murine LV free wall [17]. A three-element Windkessel model of the circulation was used to provide appropriate ventricular afterload. Mouse-specific parameter values for the circulatory model were taken from published in vivo measurements [18]. A five millisecond delay in activation was assumed across the thickness of the LV wall, based on typical conduction velocities in mouse myocardium [19]. Ca^{2+} and length-dependent myocardial contractile force was simulated using the model of Rice *et al.* [14]. The original parameter values for this model were modified to reproduce responses reported for intact mouse myocardium including pCa50 and Hill coefficient of steady-state Ca^{2+} -activated force [20]. Parameters describing myosin crossbridge kinetics were modified to vary as a function of phosphorylated RLC in accordance with data showing that phosphorylation increases crossbridge binding and accumulation of crossbridges in the strongly-bound state [2, 3].

A single cardiac beat was simulated by applying a realistic Ca^{2+} transient [20], regionally adjusted for activation delay, to each point throughout the mesh. The time course of myocardial deformation was obtained through solution of model equations under this time-varying input. Ventricular torsion was calculated using the same method as described for the MR tagging measurements.

Three separate simulations were performed. In the first, RLC phosphorylation was assumed to vary linearly across the thickness of the LV wall, with 30% phosphorylation at the endocardium and 45% at the epicardium. This transmural difference of 15% phosphorylated RLC is based on measurements made in isolated rat ventricle [10]. In the second simulation, phosphorylation was assumed to be zero at all locations in the ventricle to mimic conditions in the mutant mouse. In the third simulation, RLC phosphorylation was uniformly 40% throughout the LV, corresponding to the volume-weighted average phosphorylation in the first simulation.

5.3 Results

5.3.1 Characterization of SM and DM mice

Single mutation (SM) mice having the S15A mutation in *Mlc-2v* and double mutation (DM) mice having S14A/ S15A mutations were examined for signs of heart failure and cardiomyopathy (Figure 5.3). Mortality was markedly increased in DM mice relative to both WT and SM strains, starting at 6 months of age. By 18 months of age, survival rate was 40% in DM mice, compared with 95% and 90% in WT and SM mice, respectively (WT, $n = 20$; SM, $n = 14$; and DM, $n = 16$). At 12 months of age, DM mice also showed significantly larger ventricular mass relative to body weight in comparison with both SM and WT (Figure 5.3*b*). An examination of cardiac morphology at 12 months revealed enlarged chambers and thinning of the ventricular walls in DM (but not SM) mice. Histological examination of ventricular tissue did not reveal signs of fibrosis (common in many forms of cardiomyopathy) in either SM or DM mice. Gene expression was examined for signs of reversion to fetal patterns, but increases in key mRNA transcripts such as β -myosin heavy chain and atrial natriuretic factor were not evident in either mutant.

Signs of contractile dysfunction assessed by echocardiography were evident in DM mice by two months of age, and had worsened at four months. Fractional shortening (FS) of the myocardium at two months of age was $40.5 \pm 6.5\%$ in DM mice, significantly lower than the value of $47.3 \pm 3.2\%$ measured in WT. At four months, FS was $35.4 \pm 11.3\%$ (DM) and $44.7 \pm 4.5\%$ (WT), also significantly different (DM $n = 8$, WT $n = 12$ at both ages). No significant differences in FS between WT and SM mice were seen (not shown).

A group of WT and DM hearts ($n = 3$ and $n = 4$, respectively) were snap frozen in liquid nitrogen and myofilament proteins isolated from these hearts were screened for altered phosphorylation levels (see Figure 5.4 and the accompanying description). No significant changes were observed in either phosphorylation of cardiac tropomyosin (cTm) or myosin binding protein C (cMyBP-C). At the same time, phosphorylation of cardiac troponins T (cTnT) and I (cTnI) were signifi-

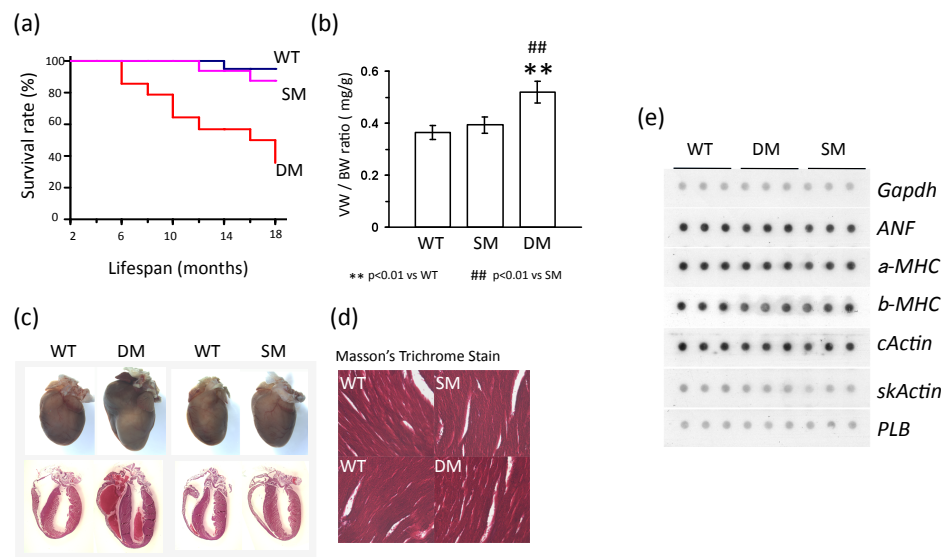


Figure 5.3: Characterization of survival, cardiac morphology, and gene expression in SM and DM mice. Survival studies show increased mortality in DM mice compared with WT and SM (a). Increased ventricular weight to body weight ratios (b) and altered ventricular morphology (c) in DM mice indicate a form of dilated cardiomyopathy in these but not SM mice. Histology of ventricular tissue (d) did not reveal fibrosis in either strain. Expression of fetal genes in SM and DM mice were also unchanged relative to WT controls (e).

cantly increased in DM hearts compared with WT. While the increase in cTnT phosphorylation was modest, cTnI phosphorylation was increased ~ 3 - fold.

5.3.2 Model-based hypothesis of RLC Phosphorylation effects on the myofilaments

Two separate hypotheses have been advanced to explain observed effects of RLC phosphorylation on striated muscle function, (1) that phosphorylation enhances diffusion of myosin heads away from the thick filament backbone [4] and (2) that it increases stiffness of the converter domain, thereby altering crossbridge cycling kinetics [21]. We examined the plausibility of either mechanism (or a combination thereof) to quantitatively reproduce Ca^{2+} sensitivities of force and the rate of force development following restretch (k_{tr}) under low ($\sim 7\%$) and elevated ($\sim 58\%$) RLC phosphorylation reported by Olsson *et al.* [2]. Parameters of the Markov model of myofilament activation (Figure 5.1) were first adjusted to simultaneously match both force and k_{tr} data at low phosphorylation levels. Leaving all other model parameters unchanged, coefficients modifying crossbridge attachment rate (f , Hypothesis 1) and powerstroke/detachment rates (h_f , h_b , and g_{xb} , Hypothesis 2) were adjusted until responses reported at elevated levels of RLC phosphorylation were matched (Figure 5.5).

Essential characteristics of the Olsson data set include the observations that RLC phosphorylation (*i*) increased maximum Ca^{2+} -activated force by $\sim 5\%$, (*ii*) increased Ca^{2+} sensitivity of force, and (*iii*) did not significantly change k_{tr} , even when several levels of Ca^{2+} activation were examined. In order to reproduce all three results, we found that parameter changes amounting to a combination of Hypotheses 1 & 2 were necessary. Increasing the crossbridge attachment rate alone (Hypothesis 1) was sufficient to increase pCa50 by the required amount, but doing so greatly exaggerated the increase in maximum tension and also caused an increase in k_{tr} , which was not observed. Hypothesis 2 was implemented as a reduction in h_f and increase in h_b to reflect the increased energetic cost of isomerization against the stiffer converter domain. We also reasoned that greater strain in post-powerstroke myosin heads would speed dissociation of crossbridges (g_{xb}).

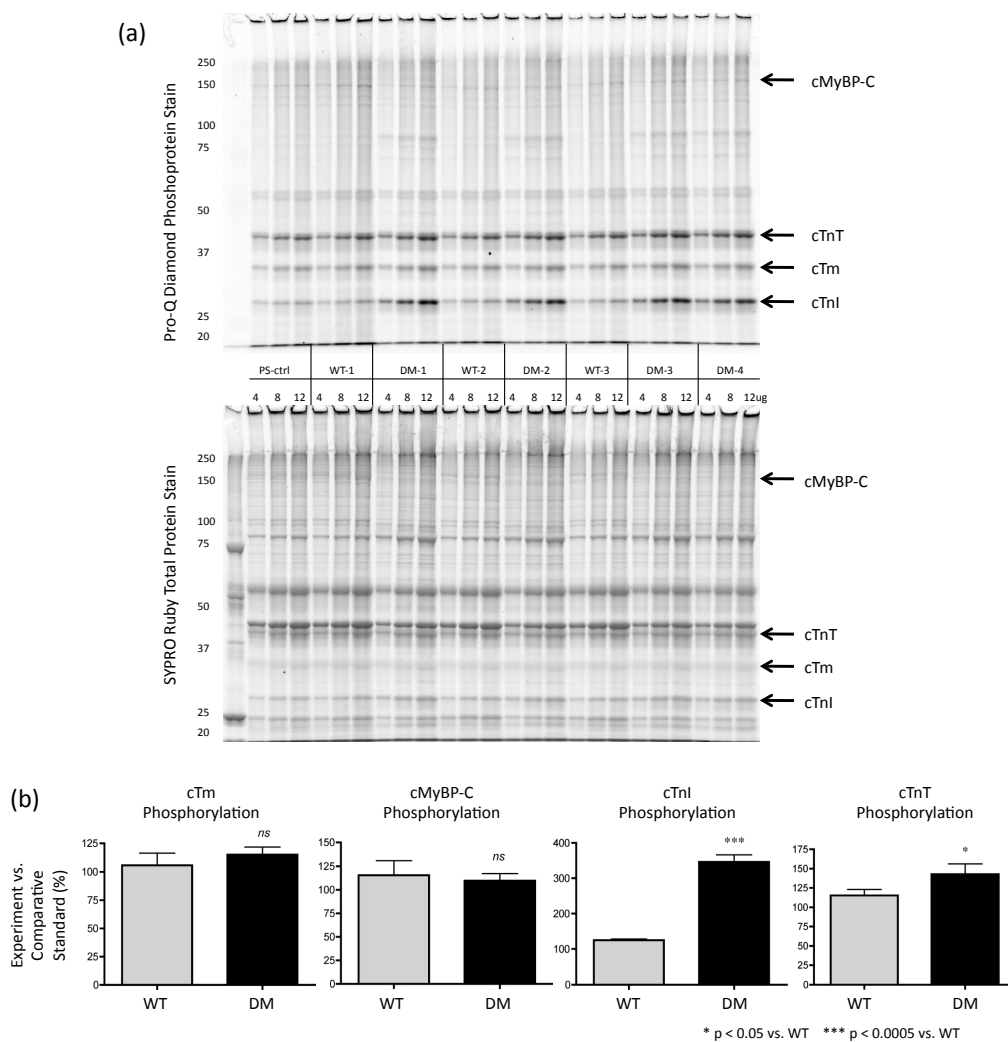


Figure 5.4: Quantification of myofibrillar protein phosphorylation in WT and DM myocardium. (a) Myofibrils from WT and DM hearts were subjected to SDS-PAGE and stained sequentially with Pro-Q Diamond stain (for phosphoprotein, upper image) and Sypro Ruby stain (for total protein, lower image). (b) Phosphoprotein content of individual bands was quantified by comparing the ratio of Pro-Q density (per μg loaded protein) to Sypro Ruby density (per μg loaded protein). Quantities are expressed as a percentage of a comparative standard run on the same gel. Phosphorylation of cardiac troponin I and troponin T were significantly elevated in DM myofibrils compared with WT. No significant difference was observed in phosphorylation of cardiac tropomyosin (cTm) and myosin binding protein C (cMyBP-C).

Table 5.1: Default Markov myofilament model parameters, including those describing hypothesized effects of RLC phosphorylation. See Section 5.2.4 for definition of parameters.

Model Parameter	Skinned Rat Trabeculae (15°C)	Intact Mouse Papillary (25°C)	Units
k_{Ca}^+	0.09	0.09	$\mu\text{M ms}^{-1}$
k_{Ca}^-	0.56	0.45	ms^{-1}
k_{+B}	75	350	ms^{-1}
k_{-B}	0.327	0.327	ms^{-1}
γ_B	75	300	-
q	0.5	0.5	-
f	1.41e-3	2.22e-2	ms^{-1}
g	4.94e-4	7.8e-3	ms^{-1}
h_f	1.41e-2	0.22	ms^{-1}
h_b	2.8e-3	4.44e-2	ms^{-1}
g_{xb}	1.41e-3	0.22	ms^{-1}
x_0	7.0	7.0	nm
Q_{RLCP}	0.0	0.0	-
p_f	0.4	0.6	-
p_{hf}	-0.7	-0.4	-
p_{hb}	0.7	0.4	-
p_{gxb}	0.175	0.3	-
p_{x0}	0.15	0.3	-

When both sets of parameter changes were used together, the result was an increased accumulation of myosin heads in the non-force producing, pre-powerstroke state (M_{pr}). Crossbridges in this state are able to increase myofilament Ca^{2+} sensitivity (by cooperatively recruiting neighboring neighboring myosin binding sites) without causing an unrealistic increase in isometric force. Slowing the overall rate of forward isomerization also offset kinetic effects of increased f , causing k_{tr} to appear insensitive to RLC phosphorylation level. The parameter set used to simulate conditions of low RLC phosphorylation are shown in Table 5.1; values for RLC-P weighting coefficients (p_f , p_{hf} , p_{hb} , p_{gab} , and p_{x0} , Table 5.1) were set such that elevated phosphorylation was simulated simply by changing Q_{RLCP} to 0.6.

5.3.3 Ca^{2+} -contraction dynamics at 25°C

Having developed a specific molecular-level description of the action of RLC phosphorylation, the DM mice (having an observable, phosphorylation-related phenotype) were an ideal tool for testing hypothesized mechanisms and their relevance to the function of intact cardiac muscle.

To this end, Ca^{2+} transients and twitch tension were measured simultaneously in isolated right ventricular papillary muscles at 25°C (Figure 5.6). No significant differences in amplitude, time constant of decay (τ_{decay}), or time from peak to 50% decay (TP50) of Ca^{2+} transients were seen between WT and DM muscles paced at the same frequency. In both strains, increasing the pacing rate from 2 Hz to 4 Hz increased Ca^{2+} transient amplitude significantly (by ~30%) without changing decay properties (Figure 5.6c).

Although Ca^{2+} transients were no different in the two strains, DM muscles displayed significantly faster twitch relaxation than WT (Figure 5.6b). In DM muscles, TP50 of tension time course was reduced by 22% relative to WT at 2 Hz, and by 10% at 4 Hz. Within strains, increased pacing frequency significantly accelerated relaxation, although this response was attenuated in DM muscles. Mean peak twitch tension at 2 Hz was lower in DM muscles (5.6 ± 1.1 kPa) than in WT (7.0 ± 0.7 kPa), although this difference was not significant. This same trend was evident at 4 Hz (DM 5.4 ± 1.4 vs. WT 7.1 ± 0.5 kPa). Time from stimulus to

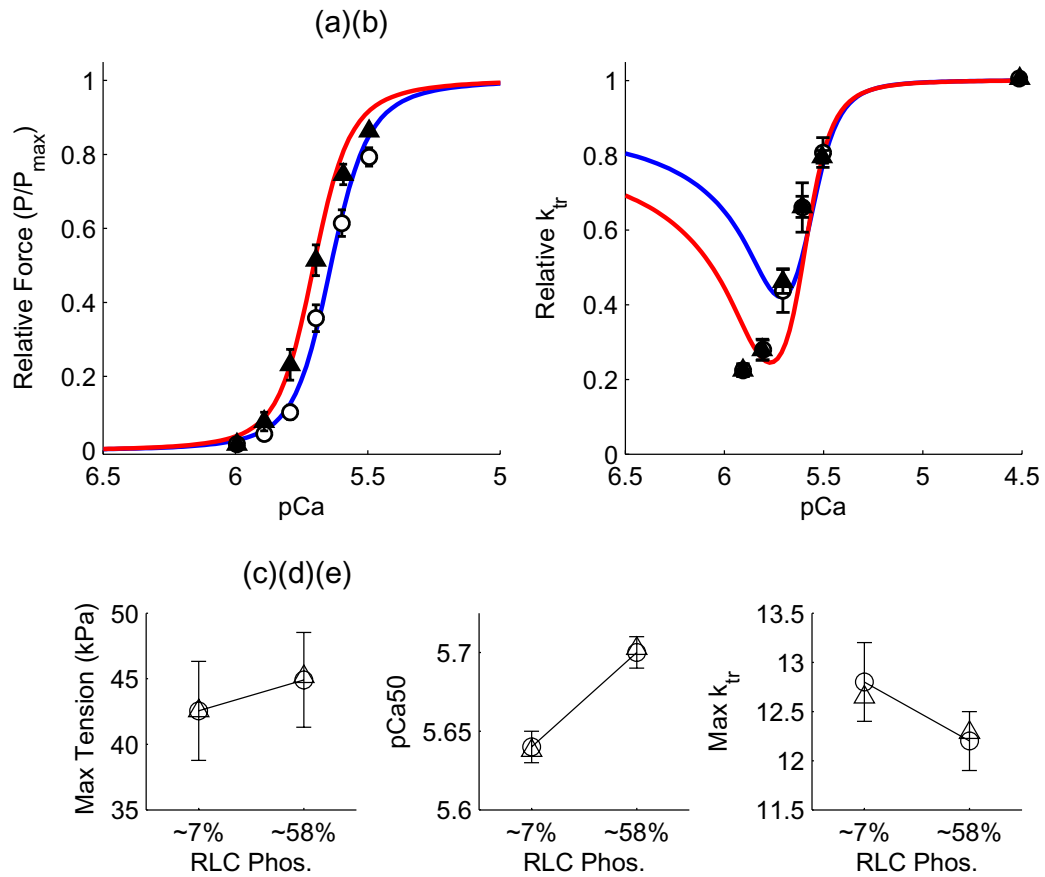


Figure 5.5: Recapitulation of RLC phosphorylation effects on skinned cardiac preparations using the Markov myofilament model. Parameters of the myofilament model were adjusted until the steady-state force- pCa (a) and k_{tr} -pCa relations (b) agreed with those reported under conditions of low (~7%) RLC phosphorylation in skinned rat trabeculae at 15°C. Blue traces and open circles show simulated and measured data, respectively. Simulations and measurements corresponding to elevated RLC phosphorylation (~58%) are shown by red traces and filled triangles. A specific combination of changes in crossbridge kinetic parameters (see Table 5.2 and description in §5.3.2) was required to reproduce observed phosphorylation-induced trends in maximal Ca^{2+} -activated force (c), half activation of steady-state force (pCa50, d), and maximum k_{tr} (e). Circles and triangles in panels c-e represent measured and simulated properties, respectively. Experimental data are shown as means \pm S.E.M. and were digitized from Olsson *et al.* [2].

peak tension (TTP-T) was the same in both strains, and was significantly reduced by increasing pacing frequency to 4 Hz (Figure 5.6c).

5.3.4 Ca^{2+} -contraction dynamics at 37°C

Intracellular Ca^{2+} transients and twitch tension were also measured in a separate group of muscles at 37°C 5 Hz pacing frequency to determine if the same alterations to contractile function could be observed under near-physiologic conditions (Figure 5.7). Time from stimulus to peak of the Ca^{2+} transient (WT 30 ± 3 ms, DM 31 ± 4 ms) was similar in the two strains. Time constants of Ca^{2+} transient decay were also not significantly different (WT 67 ± 6 ms, DM 56 ± 5 ms; $n = 4$ and 5 for WT and DM muscles respectively.) Peak twitch tension was similar in the two strains (WT 8.7 ± 2.6 kPa, DM 6.4 ± 1.4 kPa), as was time to peak tension (WT 46 ± 2 ms, DM 42 ± 1 ms). As seen in the 25°C data, the time from peak tension to 50% relaxation was significantly reduced in DM muscles (WT 21.4 ± 0.9 ms, $n = 7$; DM 16.2 ± 0.3 ms, $p < 0.001$). ($n = 7$ and 6 for WT and DM muscles respectively.)

5.3.5 Mechanisms underlying altered Ca^{2+} -contraction coupling in DM mice

The Markov myofilament model was used to test the ability of the proposed molecular actions of RLC phosphorylation to explain observed differences between WT and DM muscles. Baseline model parameters were first coarsely adjusted to reflect increased Ca^{2+} sensitivity and cooperativity associated with intact mouse cardiac muscle [20]. Then, twitch events were simulated by driving the model with a representative Ca^{2+} transient recorded in a WT preparation paced at 2 Hz and 25°C. The transient was scaled to match calibrated traces reported by Gao *et al.* [20] at the same temperature and pacing frequency. The same scaling was applied to a Ca^{2+} transient measured at 4 Hz from the same preparation for simulation of twitches at that frequency. Relative RLC phosphorylation level was assumed to be $\sim 30\%$ ($Q_{RLCP} = 0.3$) to agree roughly with reported values of phosphorylation on the endocardium [10]. Due to the fact that increased pacing frequency has

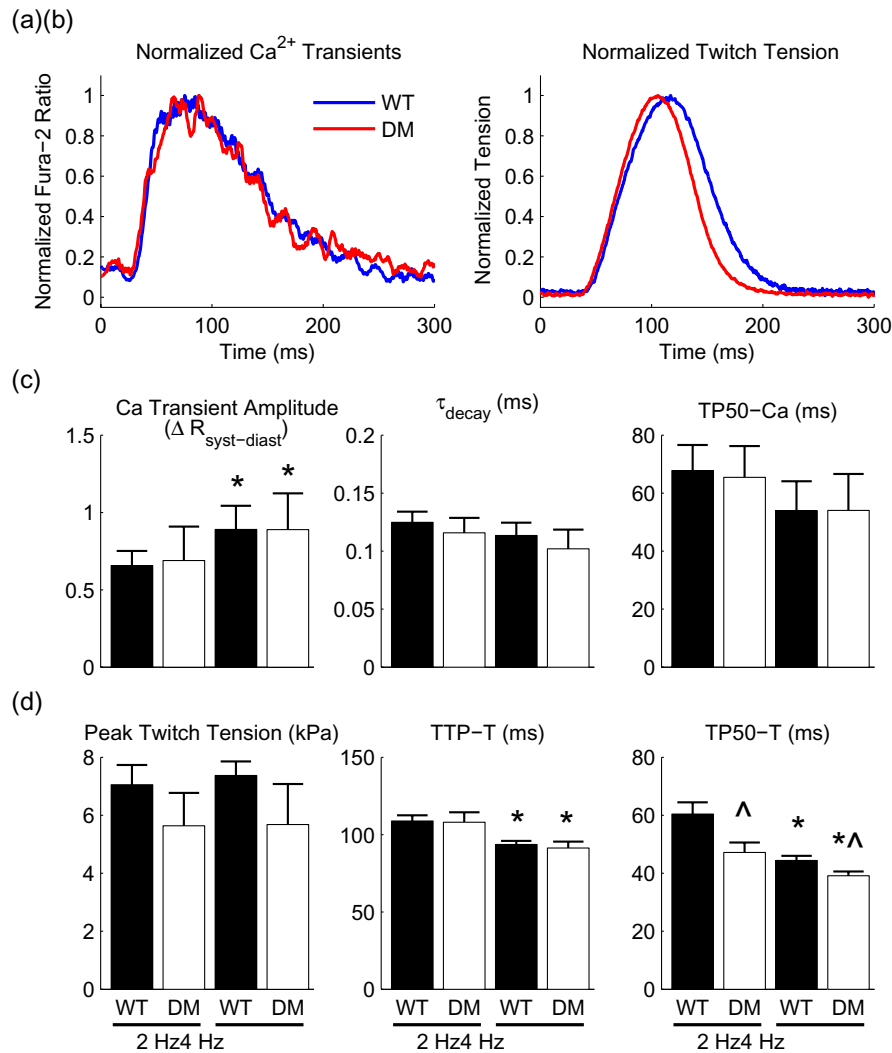


Figure 5.6: Effects of genotype on Ca²⁺-contraction dynamics at 25°C. Representative Ca²⁺ transients (a) and isometric twitch tension (b) measured simultaneously in right ventricular papillary muscles isolated from WT and DM mice. Traces were recorded following steady-state pacing at 4 Hz and have been normalized to emphasize time course features. Characteristics of (c) Ca²⁺ transients and (d) twitch tension at two pacing frequencies. Values are means ± S.E.M. ($n = 6$ WT muscles, $n = 4$ DM muscles). Abbreviations: $\Delta R_{syst-diast}$, change in Fura-2 fluorescence ratio from diastolic to peak systolic value; τ_{decay} , time constant of Ca²⁺ transient decay; TP50-Ca, time from peak to 50% Ca²⁺ transient decay; TTP-T, time from stimulus to peak tension; TP50-T, time from peak to 50% tension decay. * $P < 0.05$ vs. same group at 2 Hz. ^ $P < 0.05$ vs. WT at the same pacing frequency.

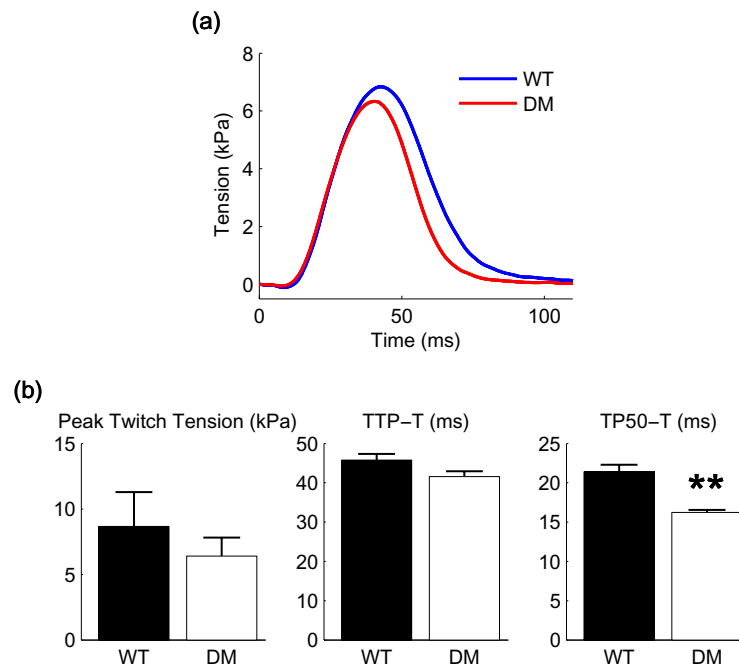


Figure 5.7: Effects of genotype on twitch dynamics at 37°C. (a) Representative isometric twitch tension measured in right ventricular papillary muscles isolated from WT and DM mice. Traces were recorded following steady-state pacing at 5 Hz. (b) Mean characteristics of twitch tension timecourses. Muscles isolated from DM mice exhibited a highly significant reduction in time from peak to 50% relaxation. Values are means \pm S.E.M. ($n = 7$ WT muscles, $n = 6$ DM muscles). Abbreviations: TTP-T, time from stimulus to peak tension; TP50-T, time from peak to 50% tension decay. ** $P < 0.001$ vs. WT.

been associated with phosphorylation of RLC and TnI [22], we reasoned that the differences in 2 Hz and 4 Hz twitch responses could be explained by changes to parameters specifically relating to phosphorylation of these two proteins. Thus, k_{Ca}^- (reflecting TnI phosphorylation [23]), and RLC-P weighting coefficients were iteratively adjusted until the model reproduced WT twitch responses at both frequencies (Figure 5.8, *a* and *b*). Table 5.1 lists the default parameters determined from this process, and Table 5.2 gives phosphorylation-dependent parameter changes required for either frequency.

In DM mice lacking an effective phosphorylation site on RLC, the only reasonable parameter to adjust was k_{Ca}^- . After setting $Q_{RLCP} = 0$, k_{Ca}^- was adjusted until simulated twitches yielded values of TP50 agreeing with mean measured values. Other observed twitch properties, including a flat force-frequency relation were predicted by this simple, one parameter fit (Figure 5.8 *c* and *d*). At 2 Hz, the value of k_{Ca}^- (Table 5.2) was 22% higher for DM mice, but at 4 Hz this parameter differed by only 4% between WT and DM fits.

The necessity and consequence of each parameter change is dramatically evident when responses are simulated in their absence. When a 4 Hz Ca^{2+} transient is used with the 2 Hz WT parameter set, the resulting peak twitch tension is increased by nearly 50%, and TP50 is increased by more than 10%. Neither change depicting RLC or TnI phosphorylation was sufficient to produce observed responses on its own; correct WT 4 Hz response required increases in both Q_{RLCP} and k_{Ca}^- , and correct DM responses at both frequencies required elimination of Q_{RLCP} and increased k_{Ca}^- (Figure 5.9).

5.3.6 Measurements and modeled effects of RLC phosphorylation on ventricular torsion

Time course of LV torsion was measured over the systolic interval (Figure 5.10). Repeated measures ANOVA showed that torsion time course between WT and mutant mice were significantly different ($p < 0.05$). Maximum torsion values for WT and mutant mice were 49 ± 2 and 36 ± 5 degrees cm^{-1} , respectively. This difference was also found to be significant ($p < 0.05$).

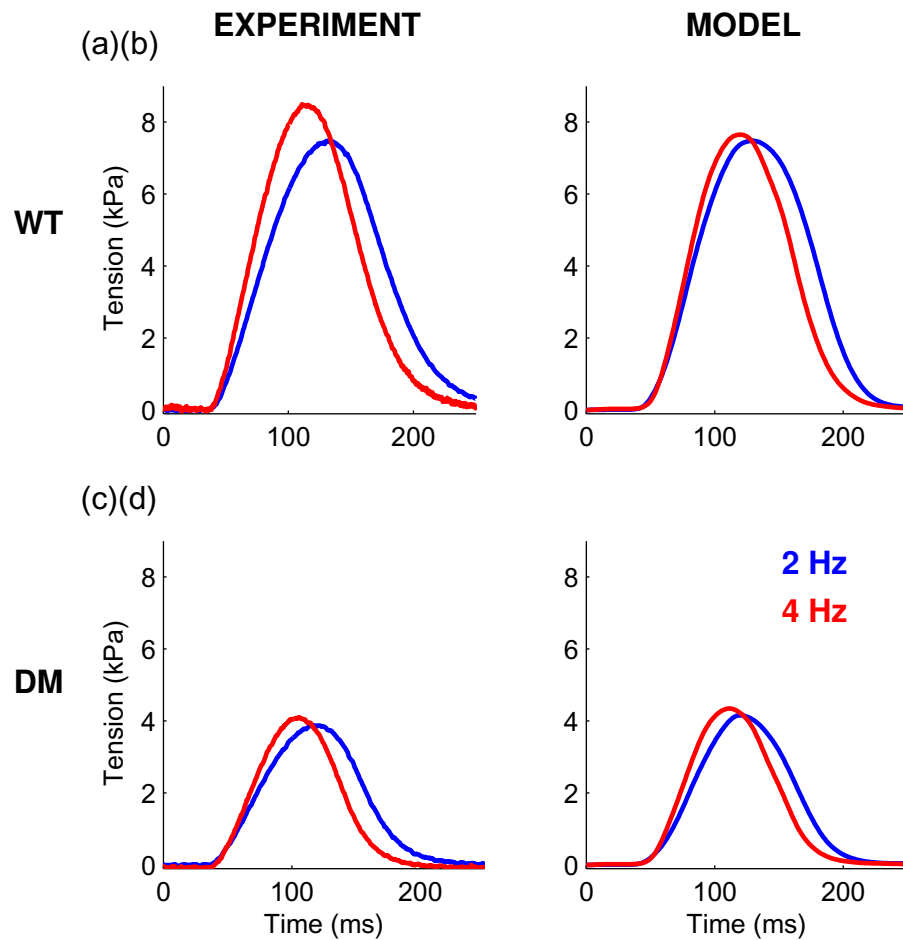


Figure 5.8: Model reproduction of the effects of pacing frequency and genotype on Ca^{2+} -contraction dynamics. In each panel, responses at 2 Hz and 4 Hz pacing rates are shown as blue and red traces, respectively. Representative records from WT (a) and DM (c) muscles show that increased pacing frequency accelerates relaxation rate without substantial change in peak twitch tension. Simulations (b and d) were performed by driving the myofilament model with Ca^{2+} -transients measured at the respective pacing frequencies (see Figure 5.9a). Qualitative matching of the model to measured tension responses required reduction of myofilament Ca^{2+} sensitivity in both WT and DM mice at 4 Hz, consistent with frequency-induced phosphorylation of TnI. In WT mice, matching also required parameter changes reflecting hypothesized effects of elevated RLC phosphorylation at both frequencies.

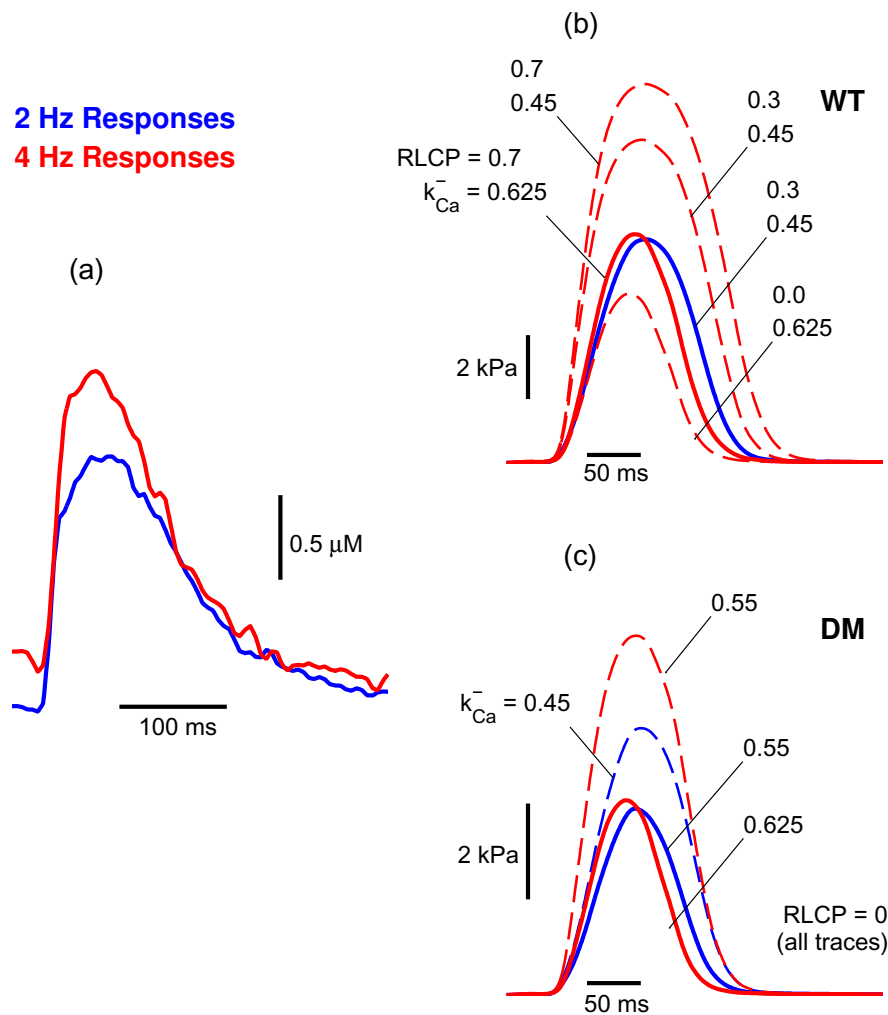


Figure 5.9: Exploration of model parameter changes required to reproduce genotype and frequency dependence of twitch responses. (a) Representative WT transients at 2 (blue trace) and 4 Hz (red trace) were used to elicit tension responses for all simulations, as no significant difference was observed between WT and DM Ca²⁺-transients. Tension traces in (b) and (c) are color coded to indicate the Ca²⁺-transient in (a) that served as input. Solid traces in (b) and (c) indicate final matched responses to measured data, while dashed lines show various intermediates. (b) Simultaneous increases in the rate of Ca²⁺ dissociation from troponin C ($k_{\text{Ca}^-}^-$) and the parameter RLCP (representing RLC phosphorylation, see text) were required to reproduce frequency dependent changes seen in WT. (c) RLCP was set to zero for DM simulations, but this change only partially accounted for the observed reductions relaxation time. These differences were reconciled by increasing $k_{\text{Ca}^-}^-$ to 0.55 ms⁻¹ for 2 Hz, and further to 0.65 ms⁻¹ for the 4 Hz response.

Table 5.2: Alterations to default Markov myofilament model parameters required to reproduce measurements of isometric twitch tension at 25°C. Condition denotes genotype and pacing frequency. See text for description of parameters.

Condition	Q_{RLCP}	k_{Ca}^- (ms^{-1})
WT, 2 Hz	0.3	0.45
WT, 4 Hz	0.7	0.625
DM, 2 Hz	0.0	0.55
DM, 4 Hz	0.0	0.625

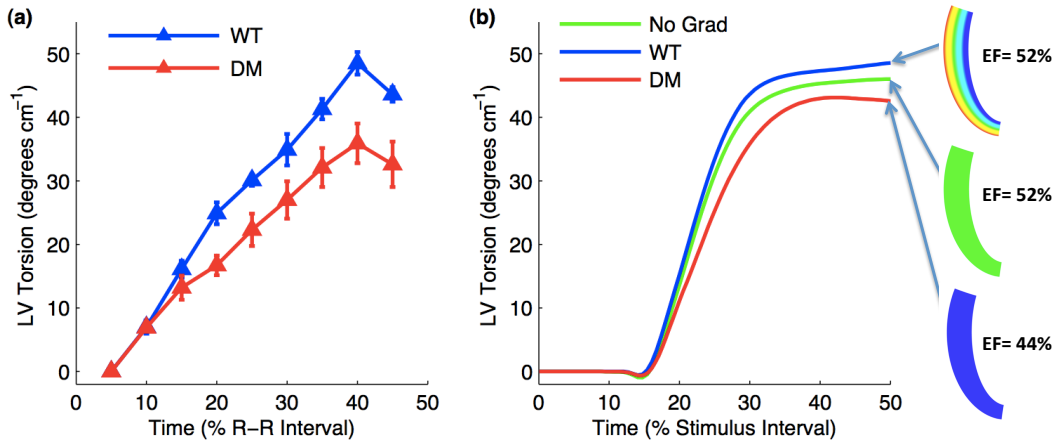


Figure 5.10: Measured and simulated effects of RLC phosphorylation on LV torsion. The time course of LV torsion during systole as measured by MR tagging (a) was significantly different between WT (blue symbols) and DM (red symbols) mice ($P < 0.05$, $n = 3$ for each group). Data points are means \pm S.E.M. LV torsion time courses predicted using a computational model (b) showed decreased torsion throughout systole when RLC phosphorylation was eliminated (DM, red trace) compared with presence of a transmural gradient of phosphorylation (WT, blue trace). A third simulation having the same average phosphorylation level as the WT simulation but without a spatial gradient (No Grad, green curve) predicted reduced torsion but identical ejection fraction (EF) compared with TM Grad. Insets to (b) depict the spatial distribution of RLC phosphorylation in a longitudinal cross-section of the LV free wall corresponding to the three simulations.

A computational model of LV function was used to predict the dependence of torsion on regulatory light chain phosphorylation. Phosphorylation was assumed to increase myofilament Ca^{2+} sensitivity and isometric force in accordance with published data [2, 3]. In the model representing WT mice, a spatial gradient of phosphorylation was assumed, levels in the epicardium being greater than those in the endocardium [10, 24]. DM mice were represented by reducing phosphorylation levels to zero throughout the myocardium. Time courses of LV torsion from the two simulations were similar to those measured, with the DM simulation exhibiting lower torsion values throughout systole (Figure 5.10). Maximum torsion values for WT and DM models were 49.5 and 43 degrees cm^{-1} , respectively. Removal of phosphorylation also reduced the simulated ejection fraction (EF) from 52% to 44%, indicating substantial loss in overall contractility. When the transmural gradient was replaced with uniform 40% phosphorylated regulatory light chain, EF was unchanged but maximum torsion dropped to 46 degrees cm^{-1} (Figure 5.10). A simulation using an apex-base gradient in phosphorylation [11] produced EF and torsion time course that was essentially identical to the uniform 40% phosphorylation case (data not shown). These results suggest that both altered contractility and absence of a transmural phosphorylation gradient contribute to the reduction in maximal torsion observed in DM mice.

5.4 Discussion

The objective of this study was to gain new insight into the function of RLC phosphorylation and its underlying molecular mechanisms, specifically in the context of intact myocardium. A novel gene-targeted mouse line in which RLC phosphorylation sites had been removed was used in conjunction with computational analysis to form and test new hypotheses. The results support two main conclusions. First, that in the mouse myocardium RLC phosphorylation alters Ca^{2+} -contraction dynamics in a manner consistent with both increased myosin diffusion and enhanced converter domain stiffness. Second, that non-invasively measured changes to ventricular wall motion are explained at least in part by

loss of a ventricular gradient in RLC phosphorylation. Computational analyses played a critical role in reaching these conclusions by providing means to control for secondary responses (such as TnI phosphorylation) that otherwise would have obscured underlying effects that were the focus of this study.

5.4.1 RLC phosphorylation appears to affect both disposition and kinetics of myosin

The longest-standing hypothesis for the molecular action of RLC phosphorylation in striated muscle has been that of increased diffusion of myosin heads away from the thick filament backbone [4]. This is thought to increase the probability of actin-myosin interactions and thereby raise muscle tension and sensitivity of Ca^{2+} . This hypothesis agrees well with observations in skinned skeletal muscle fibers which not only show enhanced force and Ca^{2+} sensitivity, but also an apparent increase in myosin kinetics, seen by increases in k_{tr} at submaximal activation levels [25]. This hypothesis has also been applied to cardiac muscle, where RLC phosphorylation is roughly characterized as increasing contractile force [2, 3, 26]. However, recent work with individual skeletal muscle myosins *in vitro* showed that phosphorylation of RLC substantially altered the duty cycle, actin sliding velocity, and myosin ADP affinity [21]. The authors of that study interpreted those results on the basis of increased stiffness of the converter domain of myosin, a region containing alpha helices stabilized by the light chains. It has also been shown that single mutations to RLC are able to alter the unitary step size of myosin (the distance moved in a single powerstroke) substantially (~ 2 fold) [27].

In the model of myofilament activation used here, both hypothesized mechanisms were required to reproduce data in skinned rat cardiac muscle (Figure 5.5). This suggests a somewhat paradoxical mode of action in which phosphorylated myosins attach more readily to the thin filament but undergo the powerstroke with greater difficulty. Thus, although increased numbers of myosin are bound to the thin filament at high phosphorylation, fewer occupy a force-producing state under isometric conditions. The net effect is to increase Ca^{2+} sensitivity of the filaments with only modest increase in maximum Ca^{2+} activated tension. Existence

of the pre-powerstroke state therefore appears vital to quantitative reproduction of observed RLC phosphorylation effects on the myocardium.

We found evidence that these same mechanisms applied to dynamic responses of intact cardiac muscle. Ca^{2+} -force dynamics measured in DM and WT mice at two pacing frequencies were well described by the model containing hypothesized RLC phosphorylation mechanisms (Figure 5.8). An examination of model parameters required to fit these measured responses (Table 5.2) suggests that at 25°C and 2 Hz pacing the consequences of non-phosphorylatable RLC in DM mice were obscured by the presence of reduced Ca^{2+} sensitivity of the troponin complex. However, the Ca^{2+} dissociation rate constants were nearly identical between WT and DM at 4 Hz pacing - suggesting that differences in twitch dynamics under these conditions (Figure 5.6*b*) are almost entirely due to direct loss of phosphorylation sites on RLC.

5.4.2 RLC phosphorylation directly affects ventricular wall motion

Davis *et al.* advanced the hypothesis that the twisting or torsion observed in the left ventricle during ejection is due to a transmural gradient of RLC phosphorylation [5]. In that study, spatial gradients in RLC phosphorylation were demonstrated in mouse hearts, with elevated levels of phosphorylation on the epicardium. Given the increased force associated with phosphorylation and the opposing orientations of endocardial and epicardial myofiber helix angles in the LV, they concluded that the epicardial twist observed in beating hearts was due to the higher RLC phosphorylation in that region.

Significantly reduced LV torsion measured in DM mice supports that hypothesis (Figure 5.10*a*), but we considered the possibility that altered wall motion could be due to secondary, indirect adaptations of the myocardium incident to loss of phosphorylation sites. A multi-scale model of LV mechanics run with and without a gradient in RLC phosphorylation provided qualitative justification for ascribing at least part of the torsion defect to direct loss of phosphorylatable RLC. It should be noted that ventricular torsion in the direction of epicardial fibers does

not require any spatial gradient in contractile properties and is predicted simply on the basis of the longer effective moment arm on the epicardium, as shown in this study (Figure 5.10*b*) and others [28]. The model properly accounts for these kinematic effects and places bounds on the extent to which RLC phosphorylation is likely to affect wall motion.

5.4.3 Limitations and future work

The analysis of Ca^{2+} -contraction dynamics presented here was performed under isometric conditions. A substantial portion of the literature regarding RLC phosphorylation is devoted to its effects on the stretch activation response. That body of work, in addition to findings in the present study suggest that an extension of our analysis to non-isometric conditions would be highly worthwhile. We have proposed that phosphorylation causes accumulation of attached myosin crossbridges in a pre-powerstroke state. This pool of crossbridges would alter the stiffness of the myocardium and its mechanical properties, possibly helping explain observed consequences of RLC phosphorylation on the stretch activated response of cardiac muscle [3].

5.4.4 Conclusions

RLC phosphorylation in cardiac muscle has generally been viewed as a mechanism for the regulation of overall contractile force and Ca^{2+} sensitivity [2, 3, 26]. Interestingly, the differences we observed in intact papillary muscles lacking phosphorylatable RLC were not ones of peak twitch tension, but rather in the time course of relaxation. This difference was highly significant at multiple pacing frequencies and temperatures (Figures 5.6 and 5.7). It also persisted after accounting for differences in TnI phosphorylation. The computational model illustrates how phosphorylation-induced changes in crossbridge function are capable of prolonging the twitch independent of peak isometric tension, namely through formation of a pool of attached, pre-powerstroke crossbridges. These effects, when coupled to a transmural gradient in phosphorylation level, contribute measurably

to wall motion of the ejecting left ventricle.

Acknowledgements

Chapter 5 contains the dissertation author's contributions to a manuscript in preparation at the time of writing entitled *Ventricular Myosin Light Chain 2 Phosphorylation S14A/S15A Mutant Knock-in Mice Display Novel Defects in Myocardial Torsion and Dilated Cardiomyopathy*. Sheikh F., Ouyang K., Campbell S.G., Chuang J., McCulloch A.D., and Chen J.

References

- [1] Sweeney, H.L., Bowman, B.F., and Stull, J.T., 1993. Myosin light chain phosphorylation in vertebrate striated muscle: regulation and function. *Am J Physiol*, 264:C1085–95.
- [2] Olsson, M., Patel, J., Fitzsimons, D., Walker, J., and Moss, R., 2004. Basal myosin light chain phosphorylation is a determinant of Ca²⁺ sensitivity of force and activation dependence of the kinetics of myocardial force development. *American Journal of Physiology- Heart and Circulatory Physiology*, 287:H2712.
- [3] Stelzer, J.E., Patel, J.R., and Moss, R.L., 2006. Acceleration of stretch activation in murine myocardium due to phosphorylation of myosin regulatory light chain. *The Journal of General Physiology*, 128:261–72.
- [4] Levine, R.J., Kensler, R.W., Yang, Z., Stull, J.T., and Sweeney, H.L., 1996. Myosin light chain phosphorylation affects the structure of rabbit skeletal muscle thick filaments. *Biophysical Journal*, 71:898–907.
- [5] Davis, J.S., Hassanzadeh, S., Winitzky, S., Lin, H., Satorius, C., Vemuri, R., Aletras, A.H., Wen, H., and Epstein, N.D., 2001. The overall pattern of cardiac contraction depends on a spatial gradient of myosin regulatory light chain phosphorylation. *Cell*, 107:631–41.
- [6] Szczesna, D., Ghosh, D., Li, Q., Gomes, A.V., Guzman, G., Arana, C., Zhi, G., Stull, J.T., and Potter, J.D., 2001. Familial hypertrophic cardiomyopathy mutations in the regulatory light chains of myosin affect their structure, Ca²⁺ binding, and phosphorylation. *J Biol Chem*, 276:7086–92.

- [7] Dias, F.A.L., Walker, L.A., Arteaga, G.M., Walker, J.S., Vijayan, K., Peña, J.R., Ke, Y., Fogaca, R.T.H., Sanbe, A., Robbins, J., and Wolska, B.M., 2006. The effect of myosin regulatory light chain phosphorylation on the frequency-dependent regulation of cardiac function. *J Mol Cell Cardiol*, 41:330–9.
- [8] Sanbe, A., Fewell, J.G., Gulick, J., Osinska, H., Lorenz, J., Hall, D.G., Murray, L.A., Kimball, T.R., Witt, S.A., and Robbins, J., 1999. Abnormal cardiac structure and function in mice expressing nonphosphorylatable cardiac regulatory myosin light chain 2. *J Biol Chem*, 274:21085–94.
- [9] Scruggs, S.B., Hinken, A.C., Thawornkaiwong, A., Robbins, J., Walker, L.A., de Tombe, P.P., Geenen, D.L., Buttrick, P.M., and Solaro, R.J., 2009. Ablation of ventricular myosin regulatory light chain phosphorylation in mice causes cardiac dysfunction in situ and affects neighboring myofilament protein phosphorylation. *J Biol Chem*, 284:5097–106.
- [10] Hidalgo, C., Wu, Y., Peng, J., Siems, W.F., Campbell, K.B., and Granzier, H., 2006. Effect of diastolic pressure on MLC2v phosphorylation in the rat left ventricle. *Arch Biochem Biophys*, 456:216–23.
- [11] Rajashree, R., Blunt, B.C., and Hofmann, P.A., 2005. Modulation of myosin phosphatase targeting subunit and protein phosphatase 1 in the heart. *Am J Physiol Heart Circ Physiol*, 289:H1736–43.
- [12] Chen, J., Kubalak, S.W., Minamisawa, S., Price, R.L., Becker, K.D., Hickey, R., Ross, J., and Chien, K.R., 1998. Selective requirement of myosin light chain 2v in embryonic heart function. *J Biol Chem*, 273:1252–6.
- [13] O’Gorman, S., Dagenais, N.A., Qian, M., and Marchuk, Y., 1997. Protamine-Cre recombinase transgenes efficiently recombine target sequences in the male germ line of mice, but not in embryonic stem cells. *Proc Natl Acad Sci USA*, 94:14602–7.
- [14] Rice, J.J., Wang, F., Bers, D.M., and de Tombe, P.P., 2008. Approximate model of cooperative activation and crossbridge cycling in cardiac muscle using ordinary differential equations. *Biophysical Journal*, 95:2368–90.
- [15] Axel, L. and Dougherty, L., 1989. MR imaging of motion with spatial modulation of magnetization. *Radiology*, 171:841–5.
- [16] Zhong, J., Liu, W., and Yu, X., 2008. Characterization of three-dimensional myocardial deformation in the mouse heart: an MR tagging study. *J Magn Reson Imaging*, 27:1263–70.
- [17] Strijkers, G.J., Bouts, A., Blankesteyn, W.M., Peeters, T.H.J.M., Vilanova, A., Prooijen, M.C.V., Sanders, H.M.H.F., Heijman, E., and Nicolay, K., 2009.

Diffusion tensor imaging of left ventricular remodeling in response to myocardial infarction in the mouse. *NMR Biomed*, 22:182–190.

- [18] Segers, P., Georgakopoulos, D., Afanasyeva, M., Champion, H.C., Judge, D.P., Millar, H.D., Verdonck, P., Kass, D.A., Stergiopoulos, N., and Westerhof, N., 2005. Conductance catheter-based assessment of arterial input impedance, arterial function, and ventricular-vascular interaction in mice. *Am J Physiol Heart Circ Physiol*, 288:H1157–64.
- [19] Morley, G.E., Vaidya, D., Samie, F.H., Lo, C., Delmar, M., and Jalife, J., 1999. Characterization of conduction in the ventricles of normal and heterozygous Cx43 knockout mice using optical mapping. *J Cardiovasc Electrophysiol*, 10:1361–75.
- [20] Gao, W.D., Perez, N.G., and Marban, E., 1998. Calcium cycling and contractile activation in intact mouse cardiac muscle. *J Physiol (Lond)*, 507 (Pt 1):175–84.
- [21] Greenberg, M.J., Mealy, T.R., Watt, J.D., Jones, M., Szczesna-Cordary, D., and Moore, J.R., 2009. The molecular effects of skeletal muscle myosin regulatory light chain phosphorylation. *American journal of physiology Regulatory, integrative and comparative physiology*, 297:R265–74.
- [22] Varian, K.D. and Janssen, P.M.L., 2007. Frequency-dependent acceleration of relaxation involves decreased myofilament calcium sensitivity. *Am J Physiol Heart Circ Physiol*, 292:H2212–9.
- [23] Tong, C.W., Gaffin, R.D., Zawieja, D.C., and Muthuchamy, M., 2004. Roles of phosphorylation of myosin binding protein-C and troponin I in mouse cardiac muscle twitch dynamics. *J Physiol (Lond)*, 558:927–41.
- [24] Davis, J.S., Satorius, C.L., and Epstein, N.D., 2002. Kinetic effects of myosin regulatory light chain phosphorylation on skeletal muscle contraction. *Biophysical Journal*, 83:359–70.
- [25] Metzger, J.M., Greaser, M.L., and Moss, R.L., 1989. Variations in cross-bridge attachment rate and tension with phosphorylation of myosin in mammalian skinned skeletal muscle fibers. Implications for twitch potentiation in intact muscle. *The Journal of General Physiology*, 93:855–83.
- [26] Andersen, G.Ø., Qvigstad, E., Schiander, I., Aass, H., Osnes, J.B., and Skomedal, T., 2002. Alpha(1)-AR-induced positive inotropic response in heart is dependent on myosin light chain phosphorylation. *Am J Physiol Heart Circ Physiol*, 283:H1471–80.

- [27] Sherwood, J.J., Waller, G.S., Warshaw, D.M., and Lowey, S., 2004. A point mutation in the regulatory light chain reduces the step size of skeletal muscle myosin. *Proc Natl Acad Sci USA*, 101:10973–8.
- [28] Taber, L.A., Yang, M., and Podszus, W.W., 1996. Mechanics of ventricular torsion. *J Biomech*, 29:745–52.

Chapter 6

Conclusions

It is increasingly evident that regional differences among ventricular muscle cells are important for normal heart function. This is suggested by studies showing that loss of certain heterogeneities accompanies the development of heart disease [1, 2]. At the same time, clinical work has revealed a strong connection between abnormal patterns of ventricular wall motion and harmful remodeling of the myocardium [3–6]. This raises the possibility that changes in physiologic patterns of cell-level properties mediate ventricular remodeling through their potential effects on myocardial deformation. However, in a disease such as dilated cardiomyopathy (DCM) that can take years to develop [7], these events often appear coincident, making this hypothesis difficult to test. In spite of challenges, the work presented in this dissertation supports the conclusion that regionally-varying properties of molecular system components (such as regulatory light chain phosphorylation) have a direct causal link to DCM.

6.1 Heterogeneous electromechanical properties affect patterns of transmural strain

It is not intuitively clear whether or not the amount of transmural variation in myocyte behavior observed in isolated cells is sufficient to alter tissue strain in the intact myocardium. After creating a model that reproduced individual

cell behaviors (Chapter 2), it was possible to address this question. Simulations of ventricular electromechanics presented in Chapter 3 which used the cell-level model with heterogeneous properties showed that heterogeneities were in fact of sufficient magnitude to alter fiber strains during early ejection. This information is useful because it not only points out that this type of influence is quantitatively possible, but highlights specific portions of the cardiac cycle that may be sensitive to cellular heterogeneities. In other words, this work demonstrates that myocardial deformation is sensitive to physiologically-relevant transmural gradients in myocyte function.

6.2 Left ventricular torsion defects precede myocardial remodeling in non-phosphorylatable MLC2v mice

Several clinical studies have documented significant reductions in LV torsion among patients diagnosed with DCM [3–6] as well as hypertrophic cardiomyopathy [8]. Similarly, young patients suffering from Duchenne muscular dystrophy (DMD) were found to have significantly lower circumferential strains (but identical torsion) compared with healthy controls - even though no deficits in global cardiac function were found [9]. This may be an example of strain defects preceding development of DCM since many DMD patients ultimately suffer develop dilated hearts.

In Chapter 5, mice were studied in which the endogenous gene encoding MLC2v had been replaced by one in which phosphorylatable serine residues at positions 14 and 15 were mutated to alanines (double mutant or DM mice). DM mice displayed a dilated cardiac phenotype and were prone to premature death. MR tagging was used to evaluate left ventricular (LV) torsion in six week-old DM mice, an age at which cardiac morphology was unaltered. A small but significant reduction in LV torsion was seen among DM mice when compared to age-matched controls. Because the torsion phenotype was detected prior to dilation of the ventricles, these findings support the idea that defects in LV wall motion are capable

of driving deleterious remodeling of the myocardium.

6.3 Defects in torsion and twitch dynamics are mechanistically linked to MLC2v mutations

Altered torsion in DM mice is most likely due to changes in myocyte twitch dynamics mediated by MLC2v phosphorylation. A biophysically-detailed model of myofilament activation predicted that MLC2v phosphorylation acted via two distinct mechanisms, increased myosin head mobility within myofilaments and increased myosin converter domain stiffness. These mechanisms were subsequently shown to account for different twitch dynamics measured in papillary muscles isolated from DM and control hearts. In a final step connecting tissue-level properties to organ function, a finite element model of LV mechanics was capable of reproducing measured torsion differences between control and DM when the putative effects of phosphorylation (and their absence in DM mice) were represented.

The link between mutated phosphorylation sites on MLC2v and altered ventricular torsion is particularly interesting because it is present before symptoms of DCM can be observed in DM mice. This leads to the conclusion that phosphorylation-mediated changes in ventricular mechanics are driving myocardial remodeling. The mechanistic detail achieved here through simultaneous use of a gene-targeted mutant mouse and biophysically-detailed computational models offers novel insights into the progression of DCM, and will likely serve as the starting point for other relevant studies.

References

- [1] Bouvagnet, P., Mairhofer, H., Leger, J.O., Puech, P., and Leger, J.J., 1989. Distribution pattern of alpha and beta myosin in normal and diseased human ventricular myocardium. *Basic Res Cardiol*, 84:91–102.
- [2] Carnes, C.A., Geisbuhler, T.P., and Reiser, P.J., 2004. Age-dependent changes

in contraction and regional myocardial myosin heavy chain isoform expression in rats. *J Appl Physiol*, 97:446–53.

- [3] Jin, S.M., Noh, C.I., Bae, E.J., Choi, J.Y., and Yun, Y.S., 2007. Decreased left ventricular torsion and untwisting in children with dilated cardiomyopathy. *J Korean Med Sci*, 22:633–40.
- [4] Kanzaki, H., Nakatani, S., Yamada, N., Urayama, S.I., Miyatake, K., and Kitakaze, M., 2006. Impaired systolic torsion in dilated cardiomyopathy: reversal of apical rotation at mid-systole characterized with magnetic resonance tagging method. *Basic Res Cardiol*, 101:465–70.
- [5] Liu, X. and Li, Z., 2010. Assessment of Cardiac Twist in Dilated Cardiomyopathy Using Velocity Vector Imaging. *Echocardiography (Mount Kisco, NY)*.
- [6] Setser, R.M., Kasper, J.M., Lieber, M.L., Starling, R.C., McCarthy, P.M., and White, R.D., 2003. Persistent abnormal left ventricular systolic torsion in dilated cardiomyopathy after partial left ventriculectomy. *J Thorac Cardiovasc Surg*, 126:48–55.
- [7] Dellefave, L. and McNally, E.M., 2010. The genetics of dilated cardiomyopathy. *Current opinion in cardiology*.
- [8] Chang, S.A., Kim, H.K., Kim, D.H., Kim, J.C., Kim, Y.J., Kim, H.C., Sohn, D.W., Oh, B.H., and Park, Y.B., 2010. Left ventricular twist mechanics in patients with apical hypertrophic cardiomyopathy: assessment with 2D speckle tracking echocardiography. *Heart*, 96:49–55.
- [9] Ashford, M.W., Liu, W., Lin, S.J., Abraszewski, P., Caruthers, S.D., Connolly, A.M., Yu, X., and Wickline, S.A., 2005. Occult cardiac contractile dysfunction in dystrophin-deficient children revealed by cardiac magnetic resonance strain imaging. *Circulation*, 112:2462–7.

Appendix A

Additional Details Relating to the Cellular Electromechanics Model

This appendix details modifications to published model parameters and equations relating to work presented in Chapter 2. All equations and parameters not mentioned here are identical to those reported in the original publications [1–3]. In some cases, equations were modified which are not contained specifically in these most recent reports and instead reference still earlier sources. In those instances, we have attempted to cite the earliest source in order to maintain a clear connection to past work.

A.1 Coupling of EP/ Ca^{2+} -handling and myofilament models

The Greenstein canine myocyte EP/ Ca^{2+} -handling model [2] as modified by Flaim and co-workers [1] was coupled to the Rice myofilament model [3] via the quantity $[\text{Ca}^{2+}]_i$. Tension and length-dependent feedback from the myofilaments was incorporated by replacing static buffering of Ca^{2+} by troponin C (TnC) as used in the original EP/ Ca^{2+} -handling model with the dynamic buffering scheme formulated by Rice et al. [3]. We replaced the right-hand side of equation A.84 in

Table A.1: Combined model of cellular electromechanics: parameters altered from originals

Parameter	Source	Original Value	Modified Value	Units
NumCaRU	(1)	50000	75000	-
n_{perm}	(3)	15	7.5	-
perm ₅₀	(3)	0.5	0.55	-
xbmodsp	(3)	1.0 (rat)	0.2 (rabbit)	-
mass	(3)	5.00E-05	2.00E-05	norm. force s ² μm ⁻¹

[4] with that of equation A50 in [3] to give the following:

$$\frac{d[LTRPNCa]}{dt} = [LTRPN]_{tot} \times \frac{d}{dt} Trop_{Apparent}(x) \quad (\text{A.1})$$

With these modifications completed, the combined models are now referred to as the fully-coupled model. Changes in parameter values for the fully-coupled model from those used originally are summarized in Table A.1.

A.2 Representing Ca²⁺ buffering by fluo-3

Buffering of intracellular Ca²⁺ by fluo-3 dye was represented by adding an equation to the existing model. Buffering was assumed to follow standard kinetics, meaning that the rate of change of Ca²⁺ bound to fluo-3 can be straightforwardly written as:

$$\begin{aligned} & \frac{d[Ca^{2+}]_{fluo}(t)}{dt} \\ & = k_{on}^{fluo}[Ca^{2+}]_i(t) ([fluo]_{tot} - [Ca^{2+}]_{fluo}(t)) - k_{off}^{fluo}[Ca^{2+}]_{fluo}(t) \end{aligned} \quad (\text{A.2})$$

where $[Ca^{2+}]_{fluo}$ is the concentration of Ca²⁺ bound to the indicator, $[Ca^{2+}]_i$ is the concentration of free cytosolic Ca²⁺, $[fluo]_{tot}$ is the total concentration of the indicator, and k_{on}^{fluo} and k_{off}^{fluo} are kinetic rate constants. Constants used throughout this study for fluo-3 buffering are listed in Table A.2 below. Fluo-3 kinetic parameters were taken from the work of Naraghi [5], who measured these values

Table A.2: Fluo-3 kinetic parameters, from Naraghi (1997)

Parameter	Definition	Value
k_{off}^{fluo}	Rate of Ca^{2+} dissociation from fluo-3	0.369 ms^{-1}
k_{on}^{fluo}	Binding rate of Ca^{2+} to fluo-3	$0.71 \mu\text{M}^{-1} \text{ s}^{-1}$

at 22°C.

The Ca^{2+} flux associated with buffering by fluo-3, J_{fluo} , was set equal to Equation A.2 and added to equation A.87 from [4] as follows:

$$\begin{aligned} & \frac{d[Ca^{2+}]_i}{dt} \\ &= \beta_i \left\{ J_{xfer} - J_{up} - J_{trpn} - J_{fluo} - (I_{Ca,b} - 2I_{NaCa} + I_{p(Ca)}) \frac{A_{cap}C_{sc}}{V_{myo}F} \right\} \end{aligned} \quad (\text{A.3})$$

A.3 Flux-clamp simulation protocol

Motivation for the flux-clamp is described in Chapter 2, while the details of its implementation are presented here. In order to drive the myofilament model with a generic Ca^{2+} flux rather than a fixed Ca^{2+} transient, a simplified version of Equation A.3 was added to the myofilament model of Rice *et al.* [3]. All Ca^{2+} fluxes except those corresponding to buffering by fluo-3, buffering by the low-affinity regulatory sites of TnC, and Ca^{2+} uptake by SERCA were lumped into a single, generic flux term J_{clamp} . Equation A.3 now becomes

$$\frac{d[Ca^{2+}]_i}{dt} = \beta_i (J_{clamp} - J_{up} - J_{trpn} - J_{fluo})$$

Ca^{2+} uptake by SERCA is approximated using the formulation of Shannon *et al.* [6] with parameters as defined by Winslow *et al.* (Table 4 in ref. [4]). As the myofilament model does not calculate the concentration of Ca^{2+} in the SR, $[Ca^{2+}]_{SR}$ is assumed have a constant value of 0.55 mM (this value corresponds to an average SR load produced by the electromechanics model using ENDO parameters and a BCL of 2000 ms). The quantity J_{trpn} is set equal to Equation A.1. Lastly, β_i represents the scaling coefficient of the rapid buffering approximation for calmodulin,

with identical parameters and formulation to that used by Winslow *et al.* [4].

Representative time courses of fluo-3/Ca²⁺ fluorescence for epi-, mid-, and endocardial cells were digitized from [7] and normalised. Each point was then converted to approximate $[Ca^{2+}]_{fluo}$ using the following formula:

$$[Ca^{2+}]_{fluo} = ([Ca^{2+}]_{fluo}^{\max} - [Ca^{2+}]_{fluo}^{\min}) y + [Ca^{2+}]_{fluo}^{\min}$$

where

$$[Ca^{2+}]_{fluo}^{\max} = \frac{[Ca^{2+}]_i^{\max} [fluo]_{tot}}{\frac{k_{off}^{fluo}}{k_{on}^{fluo}} + [Ca^{2+}]_i^{\max}}$$

and

$$[Ca^{2+}]_{fluo}^{\min} = \frac{[Ca^{2+}]_i^{\min} [fluo]_{tot}}{\frac{k_{off}^{fluo}}{k_{on}^{fluo}} + [Ca^{2+}]_i^{\min}}$$

The quantities k_{on}^{fluo} and k_{off}^{fluo} are those reported in Table A.2. $[Ca^{2+}]_i^{\max}$ was assumed to be the mean Ca²⁺ transient magnitude reported for each respective cell type in [7], while $[Ca^{2+}]_i^{\min}$ was assumed to be 0.1 μ M.

The generic Ca²⁺ flux, J_{clamp} , was initialized as a piece-wise linear function in time and adjusted via non-linear least-squares solver (`lsqnonlin`, MATLAB) until the modelled time course of $[Ca^{2+}]_{fluo}$ closely fit that extracted from the literature for the appropriate cell type. After fitting, the concentration of fluo-3 was set to zero, and J_{clamp} was used to elicit a cell shortening event. Myofilament model parameters were adjusted such that after fitting J_{clamp} to the midmyocardial cell Ca²⁺ transient and removing fluo-3, the model predicted unloaded shortening similar to measurements from (7). Final model parameters are reported in Table A.3 in the column marked BASE.

A.4 Model-based testing of hypothesized epicardial cell myofilament alterations

Several potential mechanisms were proposed to explain altered Ca²⁺- contraction displayed by epicardial cells. These hypotheses were tested by altering

myofilament model parameters in suitable ways and repeating determination of J_{clamp} via the flux-clamp protocol. Table A.3 contains parameter sets used in each case, labelled according to their abbreviations described in Chapter 2.

References

- [1] Flaim, S.N., Giles, W.R., and McCulloch, A.D., 2006. Contributions of sustained INa and IKv43 to transmural heterogeneity of early repolarization and arrhythmogenesis in canine left ventricular myocytes. *Am J Physiol Heart Circ Physiol*, 291:H2617–29.
- [2] Greenstein, J., Hinch, R., and Winslow, R., 2006. Mechanisms of excitation-contraction coupling in an integrative model of the cardiac ventricular myocyte. *Biophys J*, 90:77–91.
- [3] Rice, J., Wang, F., Bers, D., and TOMBE, P.D., 2008. Approximate model of cooperative activation and crossbridge cycling in cardiac muscle using ordinary differential equations. *Biophysical Journal*, 95:2368–90.
- [4] Winslow, R.L., Rice, J., Jafri, S., Marbán, E., and O'Rourke, B., 1999. Mechanisms of altered excitation-contraction coupling in canine tachycardia-induced heart failure, II: model studies. *Circulation Research*, 84:571–86.
- [5] Naraghi, M., 1997. T-jump study of calcium binding kinetics of calcium chelators. *Cell Calcium*, 22:255–68.
- [6] Shannon, T.R., Ginsburg, K.S., and Bers, D.M., 1998. Reverse mode of the sarcoplasmic reticulum Ca pump limits sarcoplasmic reticulum Ca uptake in permeabilized and voltage-clamped myocytes. *Ann N Y Acad Sci*, 853:350–2.
- [7] Cordeiro, J., Greene, L., Heilmann, C., Antzelevitch, D., and Antzelevitch, C., 2004. Transmural heterogeneity of calcium activity and mechanical function in the canine left ventricle. *Am J Physiol Heart Circ Physiol*, 286:H1471–9.

Table A.3: Myofilament model parameters used in flux-clamp simulations. Values not displayed are identical to those of BASE.

Parameter Name	Original Value	BASE	V1	TITIN	MyBPC	SENS	COOP	TITIN+COOP	Units
n_{perm}	15	9	-	-	-	8	11	11	unitless
$perm_{50}$	0.5	0.85	-	-	-	0.75	0.775	0.775	unitless
$xbmodsp$	1	0.2	1	-	-	-	-	-	unitless
k_{on}	0.05	0.1	-	-	-	-	-	-	$\mu M^{-1} s^{-1}$
$PCon_{titin}$	0.002	0.002	-	0.006	-	-	-	0.006	norm. force
$PExp_{titin}$	10	10	-	30	-	-	-	30	unitless
Temp	310	312	-	-	-	-	-	-	K
f_{app}	0.5	0.5	-	-	1	-	-	-	ms^{-1}

Appendix B

Additional Details Relating to the Ventricular Electromechanics Model

This appendix contains additional information relating to work presented in Chapter 3. Firstly, fiber orientation data originally collected for use in the study of Mazhari et al. (2001, *Circulation*, 104:336-341) are reported. These data were used in the assignment of myocardial fiber orientations within models. A piecewise linear function was fit to the set of all experimentally-measured fiber angles (Figure B.1) and the resulting parameterization was used in the finite element meshes of the various simulations performed. In two cases (the simulations STEEPFIB and SHALLOWFIB), fiber orientations were perturbed by changing model fiber angles to single lines fit to the individual dog data showing the largest and smallest overall transmural ranges of fiber angle (Figure B.2).

This appendix also contains fiber strain time courses measured in six anesthetized dogs (Figure B.3) as described in §3.2.8. These data illustrate the amount of variability in transmural strain distributions during systole among animals.

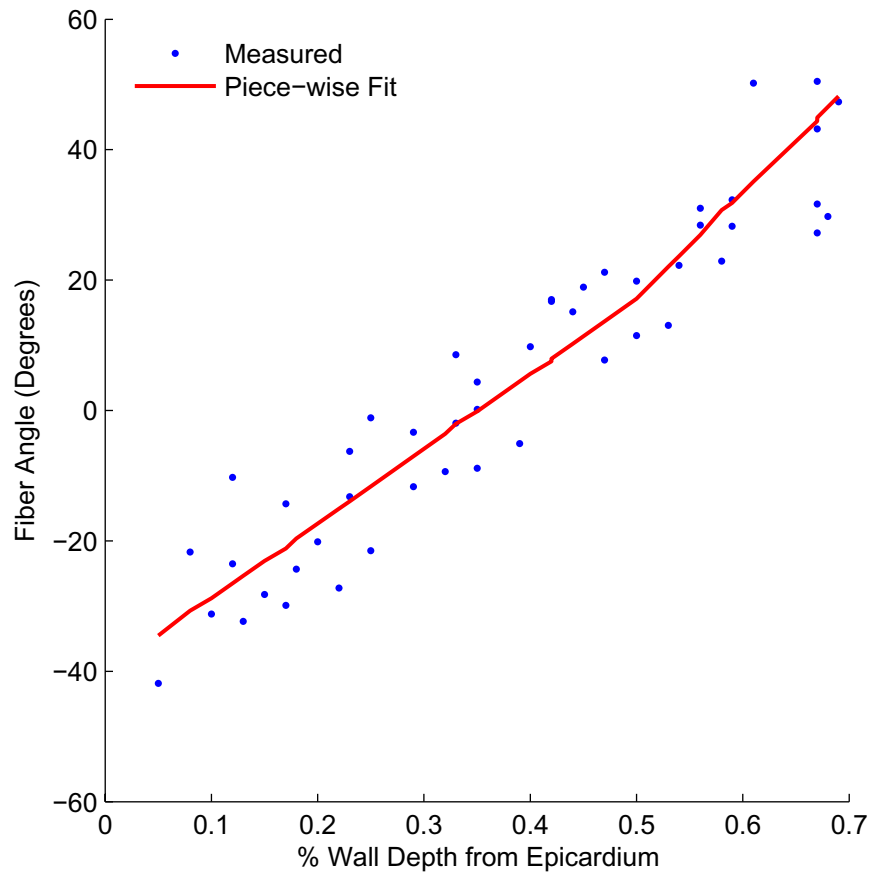


Figure B.1: Default fiber angle distribution for ventricular models used in Chapter 3. Raw data points were obtained as a part of the study of Mazhari *et al.* (2001, *Circulation*, 104:336-341), but not explicitly reported in the original publication. The red line shows a piece-wise linear fit to measured angles that was subsequently used in the finite-element models to define fiber direction.

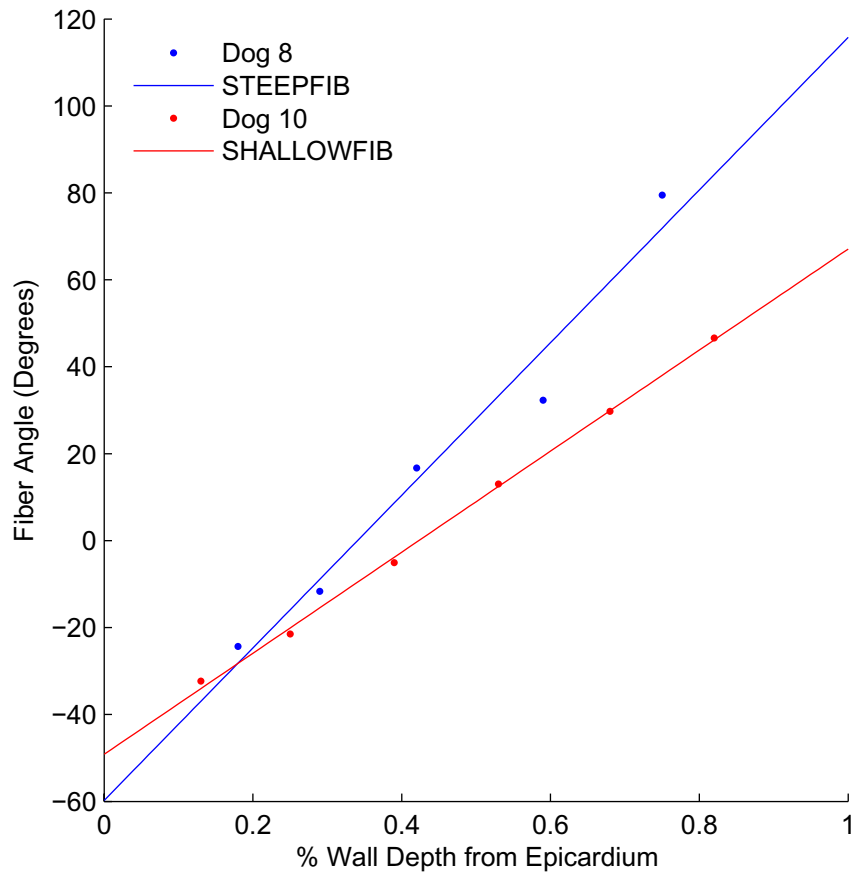


Figure B.2: Extremes in measured transmural fiber angle gradients. Measurements from individual dogs showing minimum (Dog 10) and maximum (Dog 8) transmural gradients in fiber angle were used in Chapter 3 for the simulations SHALLOWFIB and STEEPFIB, respectively. Raw data points once again originate from the study of Mazhari *et al.* (2001, *Circulation*, 104:336-341). Solid lines are linear fits to the data, used to interpolate values in the finite element meshes.

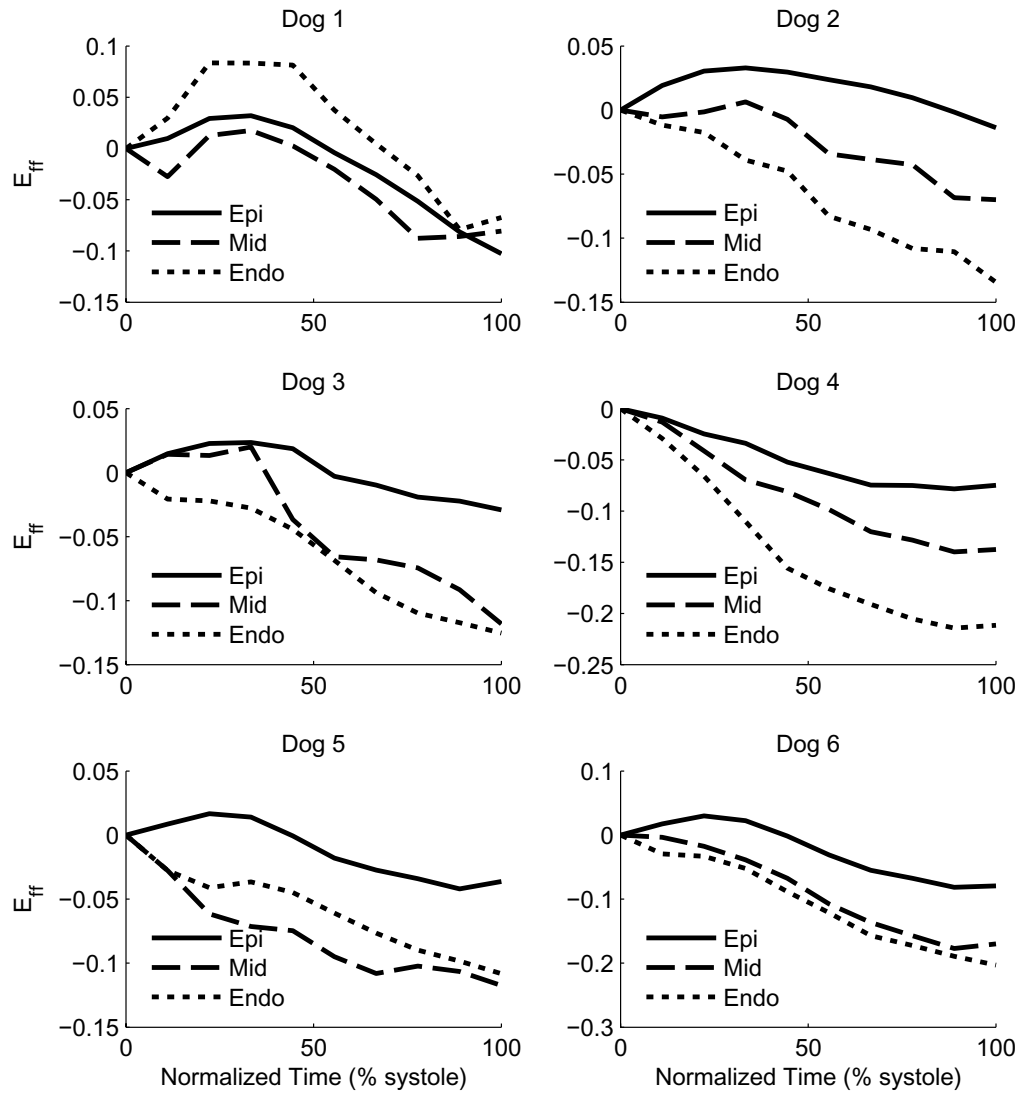


Figure B.3: Time courses of transmurial fiber strain measured in six anesthetized dogs. In each case, time has been normalized to the total duration of the systolic interval. Each trace corresponds to a different myocardial wall depth (epi-, mid-, or endocardium) as labeled.

Appendix C

Detailed Markov Myofilament Model Development and Additional Results

C.1 Introduction

This appendix contains details of model construction, description of simulation protocols, and some additional results. In §4.2 a model of individual regulatory unit (RU) function is presented in which certain transitions are dependent on the status of nearest-neighbors. Figure C.1, *a* and *b* depict the RU model in greater detail. Figure C.2 shows the relationship between tropomyosin (Tm) shifting and cooperative coefficients, and may be helpful in understanding model formulation.

Here the two methods used to compute simulations of a system of interacting RUs are presented, one continuous-time and the other stochastic.

C.2 Model of quasi-explicit (QE) near-neighbor interactions

An efficient, continuous-time model of a system of interacting RUs was sought. It was assumed that a given spatial arrangement of RUs in various Tm

states constitutes a discrete energetic state of the entire thin filament. The Ca^{2+} bound state of an individual RU is not directly communicated to nearest-neighbors. Since all possible configurations of a 26-RU thin filament would constitute 3^{26} states, a shorter segment of N adjacent RUs joined to form a ring, similar to the approach of Dobrunz *et al.* [1]. Since thin filament configurations degenerate when placed into rings this substantially reduced the number of total thin filament states. Forming rings in this manner requires every RU to be identical to all other RUs, including its disposition to myosin binding partners on the thick filament. Thus, all RUs are in a region of single overlap with thick filaments (isometric muscle conditions). The collection of all unique thin filament states and their associated transitions for a ring of N RUs is referred to hereafter as the *thin filament* (TF) model. The TF model for $N = 3$ is shown in Figure C.1c.

C.2.1 TF state generation

Generating all possible thin filament states and transitions between them for given N was accomplished using a recursive algorithm implemented in the Python scripting language. During execution, each of the 3^N naïve TF states is generated. A state is described using a string of N characters representing the Tm state of each individual RU. For example, if $N = 3$, a TF state in which two RUs are in the B state and one is in the C state would be represented by the string CBB. Note by that using the ring simplification the naïve states BCB, BBC, and CBB are equivalent. The naïve state is looped into a ring and compared to previously-generated states to determine if it is unique. If unique, the state is retained in the list of unique states. Each generation event also produces a candidate transition, from the previous state to the one just generated. The candidate transition is also examined to determine its uniqueness. If the transition has not yet been encountered, it is retained as a new, unique transition. If another transition between equivalent states has already been registered, the *degeneracy* of that transition is incremented. An example of degeneracy may be seen in the $B \rightarrow C$ transition between TF states BBB and CBB. The degeneracy of this transition is 3, because any of the three RUs in the state BBB can transition to form a state equivalent to CBB. In contrast,

there is no degeneracy in the reverse transition ($C \rightarrow B$) in this case. For each unique transition, the corresponding nearest-neighbor configuration (η) and type of transition ($B \leftrightarrow C$ or $C \leftrightarrow M$) are also recorded for use in formulating model equations. Note that

$$\eta = XY \tag{C.1}$$

where X and Y are the Tm states (B, C, or M) of either neighbor to the transitioning unit.

In summary, the algorithm systematically generates all possible states and transitions, eliminating redundant states while tallying the degeneracy and type of each transition. The results of state generation for $N = 3$ to 11, including the number of unique states and transitions, are summarized in Table C.1.

C.2.2 QE model equations

Using information gathered during state generation, an expression for the net rate of state change between two TF states related through a $B \leftrightarrow C$ transition can be written as:

$$J_{BC} = m_j k_{B+}(\eta_j) \phi P_i^{TF} - n_j k_{B-}(\eta_j) P_{i+1}^{TF}. \tag{C.2}$$

Here, i and j are indices of TF states and transitions, respectively. The quantities m and n correspond to the degeneracy of forward and reverse components of the transition j , respectively, and represent probabilities associated with occupancy of the i th and $(i+1)$ th TF states. ϕ in Eqn. C.2 is needed from the assumption that the $B \leftrightarrow C$ transition is regulated by allosteric interaction with the troponin complex (Assumption 2, Chapter 4). Because a TF transition j is a consequence of a single RU undergoing a $B \leftrightarrow C$ transition, ϕ may be defined as the probability that the blocked RU in question is free of inhibition by TnI. Let U denote a state of the troponin complex that does not inhibit the BC transition. For a population of individual RUs, ϕ is the fraction of all RUs in the blocked state that are not

inhibited by the Tn complex:

$$\phi = P\{U|B\} = \frac{P\{U\&B\}}{P\{B\}}. \quad (\text{C.3})$$

ϕ can describe the population of RUs only because of the assumption that Ca^{2+} binding is not affected by nearest-neighbor status. ϕ is the principal input (independent variable) for the TF model.

The net rate of change between two TF states related through a $C \leftrightarrow M$ transition can be written as

$$J_{CM} = 3m_j f(\eta_j) P_i^{eRU} - \rho n_j g(\eta_j) P_{i+1}^{eRU}. \quad (\text{C.4})$$

The TF model can be represented compactly as the system of coupled ordinary differential equations

$$\dot{\mathbf{P}}^{TF} = \mathbf{A}(\phi) \mathbf{P}^{TF} \quad (\text{C.5})$$

where \mathbf{P}^{TF} is a vector containing probabilities associated with occupancy of each TF state, $\dot{\mathbf{P}}^{TF}$ is a vector containing their respective rates of change, and $\mathbf{A}(\phi)$ is a coefficient matrix describing transitions among TF states, described below.

C.2.3 Combining individual RU and TF models

Individual RU and TF models were coupled to describe Ca^{2+} -based activation of the myofilaments with interacting RUs. Coupling is accomplished by assigning the two schemes to describe the same population of RUs. Because both represent the three states of Tm, the occupancy of these must agree between models. On this basis, the two models can exchange information. The TF model supplies the aggregate probabilities associated with B, C, and M states to the individual RU model. The individual RU model supplies the aggregate probability that an RU is in a blocked and Ca^{2+} -free state (B0), from which ϕ can be calculated and used as input to the TF model.

C.2.4 Calculation of aggregate Tm state occupancy from the TF model

From each TF state description the values α_i and β_i are determined. α_i is the fraction of RUs in the i th TF state not occupying the blocked state, and β_i is the fraction of RUs in the i th TF state occupying the open state. These quantities can be used to calculate the aggregate Tm state occupancy for the entire population of RUs:

$$P\{B\} = (1 - \alpha_i)\mathbf{P}_i^{\text{TF}} \quad (\text{C.6})$$

$$P\{M\} = \alpha_i\mathbf{P}_i^{\text{TF}} \quad (\text{C.7})$$

Note the implied summation over i . Given that total probability must sum to one, the aggregate probability of C state occupancy is simply

$$P\{C\} = 1 - P\{B\} - P\{M\}. \quad (\text{C.8})$$

C.2.5 Assembly of the TF model coefficient matrix

The coefficient matrix \mathbf{A} (Eqn. C.5) is constructed using vectors m , n , η , i^{pre} , and i^{post} , all of length J , the total number of transitions. These vectors are constructed automatically during state generation and can be found in the EqnData/ directory of the source code. \mathbf{A} is a sum of sparse matrices, each of which has four entries:

$$\mathbf{A}_{rr}^j = -m_j k_+(\eta_j) \quad (\text{C.9})$$

$$\mathbf{A}_{sr}^j = m_j k_+(\eta_j) \quad (\text{C.10})$$

$$\mathbf{A}_{ss}^j = -n_j k_-(\eta_j) \quad (\text{C.11})$$

$$\mathbf{A}_{rs}^j = n_j k_-(\eta_j) \quad (\text{C.12})$$

where $r = i_j^{pre}$, $s = i_j^{post}$, k_+ is the neighbor-dependent forward rate constant (k_{B+} or f , depending on the type of transition), and k_- is the neighbor-dependent reverse

rate constant (k_{B-} or g). Implementation of the matrix assembly can be seen in the file `geteRUParams.m`.

C.2.6 Equations describing coupled individual RU and TF models

The coupled model is described by a system of coupled differential and algebraic equations as follows. At any time t , the occupancy of the individual RU state B1 may be computed by

$$P\{B1\} = P\{B\} - P\{B0\}. \quad (\text{C.13})$$

The rate at which the occupancy of the individual RU state B0 changes is given by

$$\frac{dP\{B0\}}{dt} = k_{-Ca}P\{B1\} - k_{+Ca}[Ca^{2+}](t)P\{B0\}. \quad (\text{C.14})$$

ϕ is calculated as

$$\phi = \frac{P\{B\} - P\{B0\}}{P\{B\}}. \quad (\text{C.15})$$

This value of ϕ and the vector of initial conditions \mathbf{P}_i^{TF} are then used as inputs to the system of ODEs described by Eqn. C.5.

C.2.7 Computation of initial conditions and steady-state model solutions

At steady state, the rate of change of $P\{B0\}$ is zero, and Eqn. C.14 may be solved for $P\{B1\}$ to yield

$$P\{B1\} = \frac{k_{+Ca}[Ca^{2+}]}{k_{-Ca}}P\{B0\} \quad (\text{C.16})$$

Using this result, along with Eqn. C.15, ϕ at steady-state and constant $[Ca^{2+}]$ may be expressed as

$$\phi_{SS} = \frac{k_{-Ca}}{k_{-Ca} + k_{+Ca}[Ca^{2+}]} \quad (\text{C.17})$$

Given this constant value of ϕ , the dynamic TF system of equations (Eqn. C.5) becomes the linear system

$$\mathbf{A}(\phi_{ss}) \mathbf{P}^{TF} = 0. \quad (\text{C.18})$$

As a linear system, \mathbf{P}^{TF} is equivalent to the eigenvector of $\mathbf{A}(\phi_{ss})$ whose corresponding eigenvalue is zero. Steady-state solutions of \mathbf{P}^{TF} for given values of $[\text{Ca}^{2+}]$ or ϕ can be rapidly obtained using standard techniques (*eigs*, MATLAB, The MathWorks, Natick, MA). Once \mathbf{P}^{TF} is determined, a value for $P\{B0\}$ at steady state and constant $[\text{Ca}^{2+}]$ is obtained through simultaneous solution of Eqs. C.13 and C.16. This method was used to obtain steady state model solutions as well as generate initial conditions for time-evolved solutions.

C.2.8 Calculation of myofilament force and total permissive binding sites

Force produced by the myofilaments is assumed to be proportional to the fraction of RUs in the M state as this corresponds to strongly-bound crossbridges:

$$F \propto P\{M\}. \quad (\text{C.19})$$

Description of force in this way again requires the assumption that the system in question is at constant sarcomere length. Another quantity of interest is the fraction of total RUs which are permissive of strong XB binding, regardless of whether or not an XB is actually attached. The fraction of ‘active’ RUs is simply the sum of C and M state probabilities,

$$A_{tot} = P\{C\} + P\{M\}. \quad (\text{C.20})$$

C.2.9 Simulation of rapid slack/re-stretch maneuver in the QE model

The rate of tension redevelopment, k_{tr} , is the time constant of the rise in force after a rapid slack-restretch is applied to constantly activated muscle.

When the motor movement during the re-stretch event is critically-damped, force redevelops to steady-state from a non-zero, residual force (F_{resid}) [2].

Simulated values of k_{tr} and F_{resid} were obtained by modeling slack-restretch as a transient lowering of the duty cycle, defined as

$$\delta = \frac{f^{ref}}{f^{ref} + g^{ref}}. \quad (\text{C.21})$$

In each slack/restretch simulation, steady-state force F_{SS} was first calculated at a given concentration of activating Ca^{2+} . Then, duty cycle was reduced temporarily to a lower value (δ_{rs}) to reflect mechanical detachment of XBs and a new equilibrium solution was computed. Using that solution for initial conditions, δ was restored to its normal value and the model equations were evolved in time until steady state was achieved. Myofilament force was calculated at each time point, and k_{tr} was calculated using the formula:

$$k_{tr} = -\frac{\ln(1/2)}{t_{1/2}} \quad (\text{C.22})$$

where $t_{1/2}$ is the time from re-stretch required for force to reach $F_{resid} + 0.5(F_{SS} - F_{resid})$. Unless otherwise indicated, it was assumed that essentially all XBs were dissociated by the k_{tr} maneuver, setting $\delta_{rs} = 1\text{e-}8$.

C.2.10 Alternative model: 3 Independent XBs per RU

An alternative form of the QE model was constructed to account for three independent XBs binding per RU (Figure C.3). This was done to represent an upper bound of the possible number of XBs in the intact myofilament lattice that are of the correct disposition for binding to a given RU [3]. The M state in the original RU model was split into three: M1, M2, and M3, representing one, two, and three bound crossbridges, respectively. Attachment of the first XB ($C \leftrightarrow M1$ transition) was assumed to depend on nearest-neighbor Tm states just as in the original RU model. Attachment of second and third XBs was assumed to be independent of nearest-neighbors, the first XB maximally displacing Tm and

effectively masking any effect of more distant binding events. Coefficients were added to forward and reverse rates to account for the presence of more than one XB; for instance the rate of the $C \rightarrow M1$ transition is multiplied by three to reflect the fact that three XBs are attempting to bind, and so on (see Figure C.3).

It was further assumed that RUs could not differentiate between one and more than one XB bound to neighboring RUs, allowing the total number of TF states to remain the same. The only change required to the TF model was to Eqn. C.4:

$$J_{CM} = 3m_j f(\eta_j) P_i^{eRU} - \rho n_j g(\eta_j) P_{i+1}^{eRU}. \quad (\text{C.23})$$

The coefficient 3 on the first term reflects the presence of 3 cycling XBs, and ρ represents the portion of the transitioning M-state RU in TF state $i+1$ with only one XB attached. The quantity ρ is analogous to ϕ in that it describes the portion of each TF state capable of making the relevant transition. For dynamic calculations, ρ is computed as

$$\rho = \frac{P\{M\}_{TF} - (P\{M2\} + P\{M3\})}{P\{M\}_{TF}} \quad (\text{C.24})$$

where $P\{M2\}$ and $P\{M3\}$ are occupancies of M2 and M3 individual RU model states, respectively. Two differential equations are added to the individual RU model as well:

$$\frac{dP\{M2\}}{dt} = 2f^{MM}P\{M1\} + 3g^{MM}P\{M3\} - (f^{MM} + 2g^{MM})P\{M2\} \quad (\text{C.25})$$

$$\frac{dP\{M3\}}{dt} = f^{MM}P\{M2\} - 3g^{MM}P\{M3\} \quad (\text{C.26})$$

The following expression is used to determine occupancy of the M1 state by conservation:

$$P\{M1\} = P\{M\}_{TF} - (P\{M2\} + P\{M3\}) \quad (\text{C.27})$$

Steady-state solutions are determined as in the original formulation, with the additional step of calculating ρ , as follows. Because ρ is a ratio of state occupancies, it may be found by assuming an arbitrary value for $P\{M1\}$, setting the left-hand

sides of Eqns. C.25 and C.26 to zero, and solving for $P\{M2\}$ and $P\{M3\}$. Then,

$$\rho = \frac{P\{M1\}}{P\{M1\} + P\{M2\} + P\{M3\}}. \quad (\text{C.28})$$

C.2.11 Simulation of fluorescence polarization measurements

Fluorescence polarization (FP) has been used to measure Ca^{2+} - and crossbridge-dependent structural changes to the troponin complex [4, 5]. In these experiments, skinned muscle preparations containing rhodamine-labeled TnC are exposed to varying $[\text{Ca}^{2+}]$ and other conditions while monitoring contractile force and the average fluorescent probe angle using FP. Changes in probe angle have been interpreted based on three conformational states of TnC: an inactive state, a Ca^{2+} -bound state, and a force-producing state. Bell *et al.* [4] suggested that the Ca^{2+} -bound and force-producing states corresponded to angle changes of opposite sign centered around an orientation belonging to the inactive state. While the present model lacks molecular-level detail needed to explicitly predict average probe angle based on structural considerations, the three TnC conformations are represented in the model; Ca^{2+} -free, Ca^{2+} -bound, and fully-activated TnC conformations correspond with B0, B1, and C/M states of the individual RU model, respectively (Figure C.1a). Average angle change was assumed to be the sum of TnC conformation occupancies weighted by their corresponding angle change:

$$\Delta\theta_{AVG} = \Delta\theta_{B0}P\{B0\} + \Delta\theta_{B1}P\{B1\} + \Delta\theta_{C,M}P\{C, M\} \quad (\text{C.29})$$

For simplicity, it was assumed that equal and opposite unit changes in angle are associated with states B1 and C/M ($\Delta\theta_{B1} = -1$, $\Delta\theta_{C,M} = +1$), while the B0 angle is neutral ($\Delta\theta_{B0} = 0$).

C.3 Monte Carlo (MC) simulations of interacting RUs

A brute-force Monte Carlo scheme was also used to compute simulations of systems of coupled RUs. In these simulations, the state of each of N RUs was explicitly tracked over multiple fixed time steps of width Δt . During each time step, the state of each RU was updated in turn based on comparing a random number between 0 and 1 (R , generated using *rand* command in MATLAB) with forward and reverse transition probabilities (p_+ and p_- , respectively). If $R > p_+$, the state of the RU is advanced rightward (referring to Figure C.1a). Similarly, if $R > (1 - p_-)$, the state of the RU is shifted leftward. The transition probabilities are of the generic form

$$p = k(XY) \Delta t \quad (\text{C.30})$$

where $k(XY)$ is the (possibly) nearest-neighbor dependent rate constant associated with the transition in question. Rate constants are identical to those described in Chapter 4 and shown in Figure 4.1. Values of X and Y are determined for each RU at the beginning of each time step, that is, they do not change as successive RUs are updated. RUs on either end of the simulated thin filament were either assigned one ‘phantom’ neighbor fixed in the B state or assigned the other terminal RU as a second neighbor (periodic boundary conditions) to reflect conditions in the ODE implementation.

Values of Δt were determined such that the most rapid transition rate for the given parameter set produced a transition 60% of the time on average. In order to obtain meaningful results from these stochastic simulations, it was necessary to average >1000 repetitions of each time course simulation.

C.3.1 Simulation Protocol

The same protocol was used for all MC simulations. All RUs were initialized to reside in the B0 state at time $t = 0$. Ca^{2+} concentration was set to the desired value, and the system was evolved in time as described above until reaching 2500

ms elapsed time. At that point, a rapid slack/restretch maneuver was simulated by breaking all XBs (changing all M state RUs to the C state) instantaneously and preventing XB attachment for an additional 10 ms. XB binding was then reinstated and recovery was simulated for another 2490 ms. These simulation intervals were sufficient to determine steady-state Ca^{2+} activated force and k_{tr} for all pCa values and parameter sets encountered in the present study.

C.3.2 Simulated action of NEM-S1

N-ethylmaleamide treated S1 myosin fragments (NEM-S1) are soluble, non force-producing, and have a high affinity for actin filaments even in the presence of ATP. Steady-state force-pCa and k_{tr} -pCa relations were simulated in the presence of NEM-S1 using MC simulations. Action of NEM-S1 was modeled by assuming that when bound within an RU, NEM-S1 holds Tm permanently in the M state and that endogenous XB may still cycle to produce force within an NEM-S1-containing RU. Thus, an NEM-S1 containing RU appears to neighbors to be permanently in the M states as far as neighbors (and their rate constants) are concerned. Similarly, XBs within the NEM-S1 containing RU bind and dissociate at rates f^{MM} and g^{MM} consistent with the idea that NEM-S1 maximally displaces Tm within the RU and masks any effects of neighboring RU status.

All NEM-S1 simulations were made with full length, $N = 26$ thin filaments using non-periodic, fixed boundary conditions. At the beginning of each NEM-S1 time course simulation, fragments were bound at random throughout the filament with a frequency of 10%. This probability of NEM-S1 binding was used as it generated a steady-state force at pCa 9.0 roughly equal to that reported in experiments [6].

C.3.3 Simulated action of non-functional TnC

The MC method was also used to simulate the effects of a mutant, non- Ca^{2+} binding form of TnC (xTnC) [7]. These simulations were also carried out on full-length filaments ($N = 26$, non-periodic boundary conditions). It was assumed

that xTnC-containing RUs were not capable of leaving the B0 state, and were therefore permanently deactivated. These RUs were chosen at random prior to each time course simulation, with a frequency of 25, 50, or 75% depending on the treatment group.

C.4 Supplemental Results

C.4.1 Effects of solution method, number of RUs, and boundary conditions on solutions

In order to determine the effects of forming RUs into rings, steady-state force and k_{tr} -pCa relations generated using the QE method were compared with others generated using the MC method (Figure C.4). First, the MC method was used to simulate nine looped RUs in order to mimic conditions used in the QE model. The two methods produced essentially identical force-pCa and k_{tr} -pCa relations, subject to stochastic noise at low levels of activation when force-producing events are fewer in number. Next, the MC method was used to simulate a full-length, 26-RU thin filament with fixed boundary conditions. These conditions simultaneously show the effects of simulating all 26 RUs and removing the periodic boundary conditions (Figure C.4). Compared with the nine RU, looped case, pCa_{50} of the force-pCa curve was right-shifted slightly (from pCa 5.9 to 5.84). The Hill coefficient of steady-state force was slightly reduced (from 2.6 to 2.33), and the Hill coefficient fit to force greater than half maximal was substantially reduced (from 2.1 to 1.65). The k_{tr} -pCa relations for both cases were essentially identical, once again deviating most significantly at low activation due to noise.

These results indicate that boundary conditions contribute to asymmetry of the force-pCa curve in a physiologic manner (reducing Hill coefficient at high activation [8]). The other differences are small compared with experimentally observed variation in these quantities, suggesting that the assumptions used to obtain the much more efficient QE method are reasonable.

C.4.2 Expanded Sensitivity Analysis results

Three cooperative coefficient combinations were performed beyond those shown in the Chapter 4. These are (1) Removal of γ_B cooperativity from the default set (Parameter Set 2, Table 4.1), (2) Removal of μ_M cooperativity from the default set (Parameter Set 2, Table 4.1), and (3) Equal energetic contribution from each coefficient in the presence of three XBs per RU. These additions may be seen in Figure C.5, rows 2, 3, and 9, respectively.

Simulations were also performed in which the equilibrium constant was increased to achieve a pCa_{50} of 6.3 to examine the interaction of the various cooperative coefficient combinations with increased activation (Figure C.6). All 36 simulation conditions were repeated twice, once with the parameter r set to 1.0, and again with $r = 0.0$. This shows the consequences of applying cooperative interactions either entirely to XB attachment ($r = 1.0$) or detachment ($r = 0.0$). Parameters characterizing force-pCa and k_{tr} -pCa relations are given in Tables C.4-C.13 and C.17-C.21 at the end of this document. Fitted parameters used in each simulation are given in Table C.14-C.16 and C.22-C.24.

The main outcomes of the sensitivity analysis are that (1) γ_B is the most potent of the three cooperative coefficients in terms of Hill coefficient of force and Ca^{2+} dependence of k_{tr} , (2) γ_M contributes preferentially to increasing Hill coefficient of force and decreasing k_{tr} at low levels of activation, (3) A greater level of γ_B relative to the other coefficients produced responses most closely resembling physiologic responses, (4) Allowing three XBs to bind independently while maintaining the same apparent XB duty cycle did not significantly alter responses (in the presence of equal amounts of each type of cooperativity), and (5) Causing cooperative interactions to affect the attachment of XBs generally produced more physiologic responses than having interactions affect detachment.

C.4.3 k_{tr} is roughly proportional to the fraction of total activation not depending on XBs

k_{tr} and A_{Ca}/A_{tot} (see Chapter 4) approached a linear relation having slope

$$(A_{Ca}/A_{tot})^{\max}/k_{tr}^{\max}$$

or 0.095 sec. (Parameter Set 2, shown in Figure C.7 in this document). This suggests that k_{tr} at any activation level reflects both intrinsic XB cycling rate as well as the balance between XB and Ca^{2+} -recruited force.

C.4.4 Additional results from xTnC simulations

In simulations with 25, 50, and 75% replacement of functioning TnC with xTnC, the maximal Ca^{2+} force was greatly reduced, even beyond that reported in experiments (Figure C.8a). Time courses of force redevelopment, as reported in Chapter 4, were also changed by presence of xTnC. Some time course responses are shown in Figure C.8, *b* and *c*.

C.4.5 Model responses to time-varying Ca^{2+} input

Using Parameter Set 4 (Table 4.1) the model reproduced steady-state force-pCa curves obtained during pharmacologically-slowed twitches [1] in intact rat trabeculae at 22 degrees C (Figure C.9). Without changing equilibrium constants, it was then possible to adjust kinetic rates such that twitch force in response to a measured Ca^{2+} transient (Figure C.10a) agreed closely with measured twitch force ($R^2 = 0.846$, 5.6% RMS error, Figure C.10b) also from rat trabecula at 22 deg C and under constant sarcomere length [9].

Driving the model with Ca^{2+} transients measured in the study of Dobrunz *et al.* [1] (Figure C.11) in intact rat trabecula treated with ryanodine and CPA in 3.0, 4.5, and 6.0 mM $[Ca^{2+}]$ solutions qualitatively recapitulated time courses of recorded twitches (Figure 4.8a). Ca^{2+} transient magnitude had little effect on the time to peak but strongly affected the rate of relaxation (Table C.2). Elapsed

time from peak twitch force to 50% decay predicted by the model also agreed well with measured values.

Properties of the time course of activation (A_{tot}) in response to an idealized Ca^{2+} transient are summarized in Table C.3, and correspond with simulations shown in Figure 4.8.

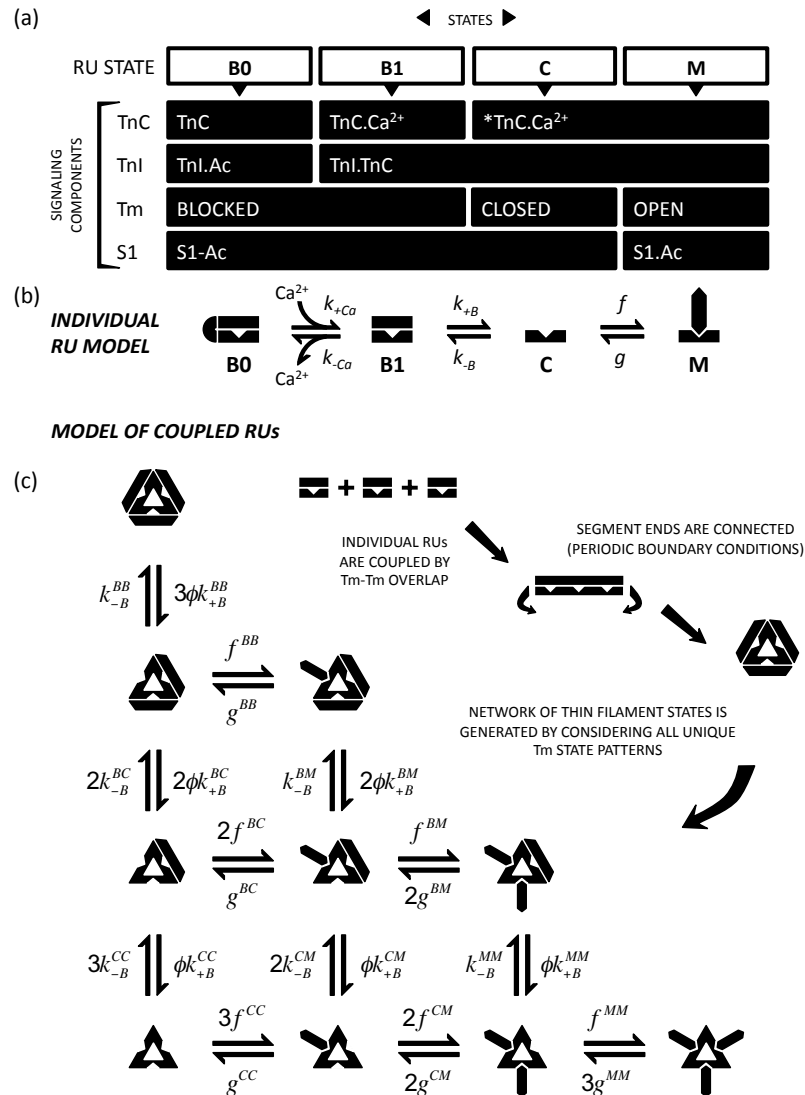


Figure C.1: Individual regulatory-unit (RU) and thin filament (TF) models. (a) The individual RU model has four states corresponding to conformation of troponin C (TnC), troponin I (TnI), tropomyosin (Tm), and myosin (S1) and their status with respect to Ca²⁺ or actin (Ac). (b) Individual RU model showing transition rates connecting states. (c) The TF model approximates activation of the thin filament by considering several individual RUs, coupled by Tm-Tm interactions. Looping short segments of RUs allows elimination of redundant states through symmetry. Individual RU and TF models are coupled via ϕ , the probability that a blocked RU is free of inhibition by TnI. This diagram shows a system of 3 coupled RUs; A system of 9 coupled RUs was used in simulations.

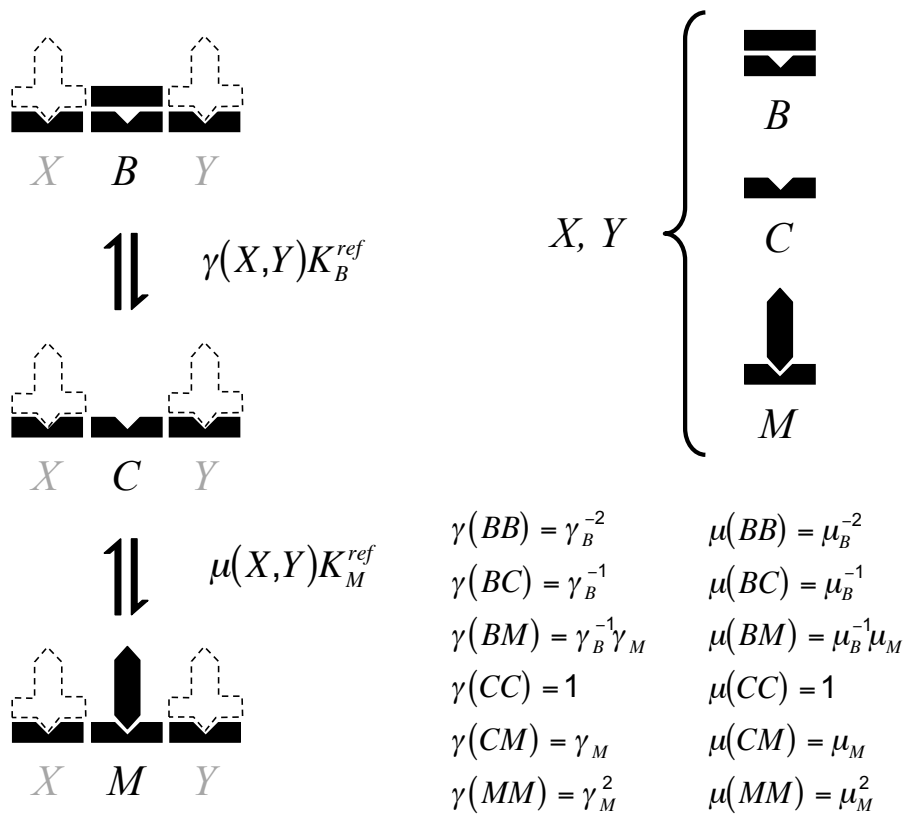


Figure C.2: Diagram showing how cooperative coefficients γ_B , γ_M , and μ_M relate to nearest-neighbor status, modifying the reference equilibrium constants K_B^{ref} and K_M^{ref} .

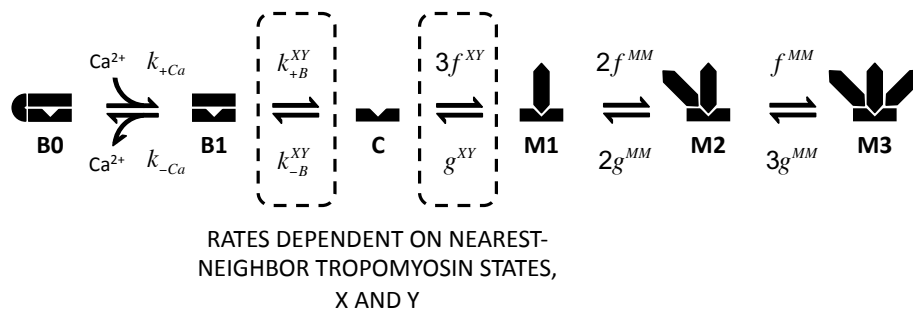


Figure C.3: This diagram shows the alternative form of the individual RU model allowing for multiple crossbridges per regulatory unit.

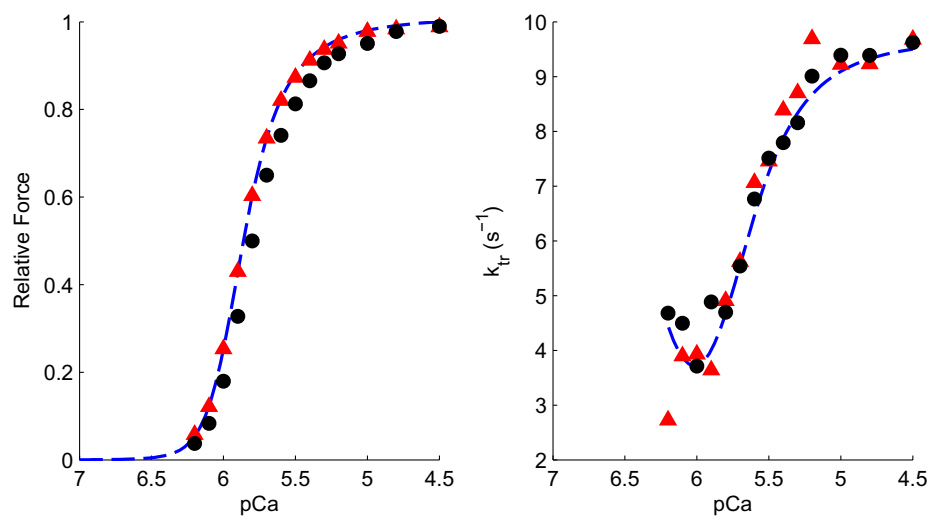


Figure C.4: Comparison of the quazi-explicit (QE) and Monte Carlo (MC) model solution methods. In each panel, QE results using 9 RUs arranged in rings are represented as blue, dashed traces; MC results using 9 RUs arranged in rings are shown as red triangles; and MC results using full-length thin filaments (26 RUs) and non-periodic boundary conditions are shown as black circles.

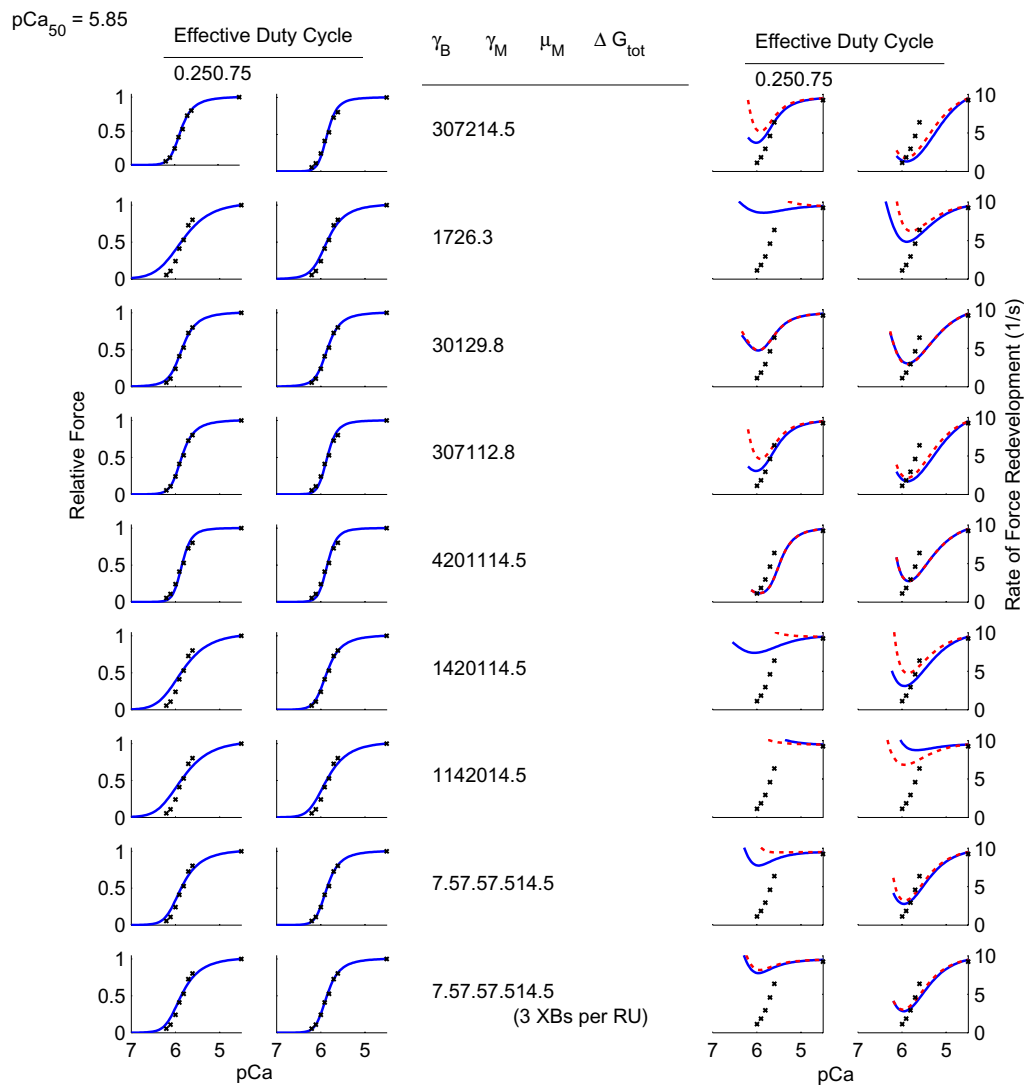


Figure C.5: Expanded sensitivity analysis, showing different effects of cooperative coefficients γ_B , γ_M , and μ_M on Ca^{2+} sensitivities of force and the rate of force redevelopment (k_{tr}). Corresponding values of γ_B , γ_M , and μ_M are given for each row of results along with ΔG_{tot} , the sum of absolute energy changes (kJ/mol) described by the given combination of cooperative coefficients. For each set of cooperative coefficients, the equilibrium constant K_B^{ref} and crossbridge kinetic rates f^{ref} and g^{ref} were adjusted simultaneously until half activation of force was pCa 5.85, effective crossbridge duty cycle was either 0.25 or 0.75, and k_{tr} at pCa 4.5 was 9.5 s⁻¹. Experimentally measured values from Fitzsimons et al. (2001) are repeated in each panel as a common reference (x's), blue lines are responses for $r = 1.0$, dashed red lines are for $r = 0.0$.

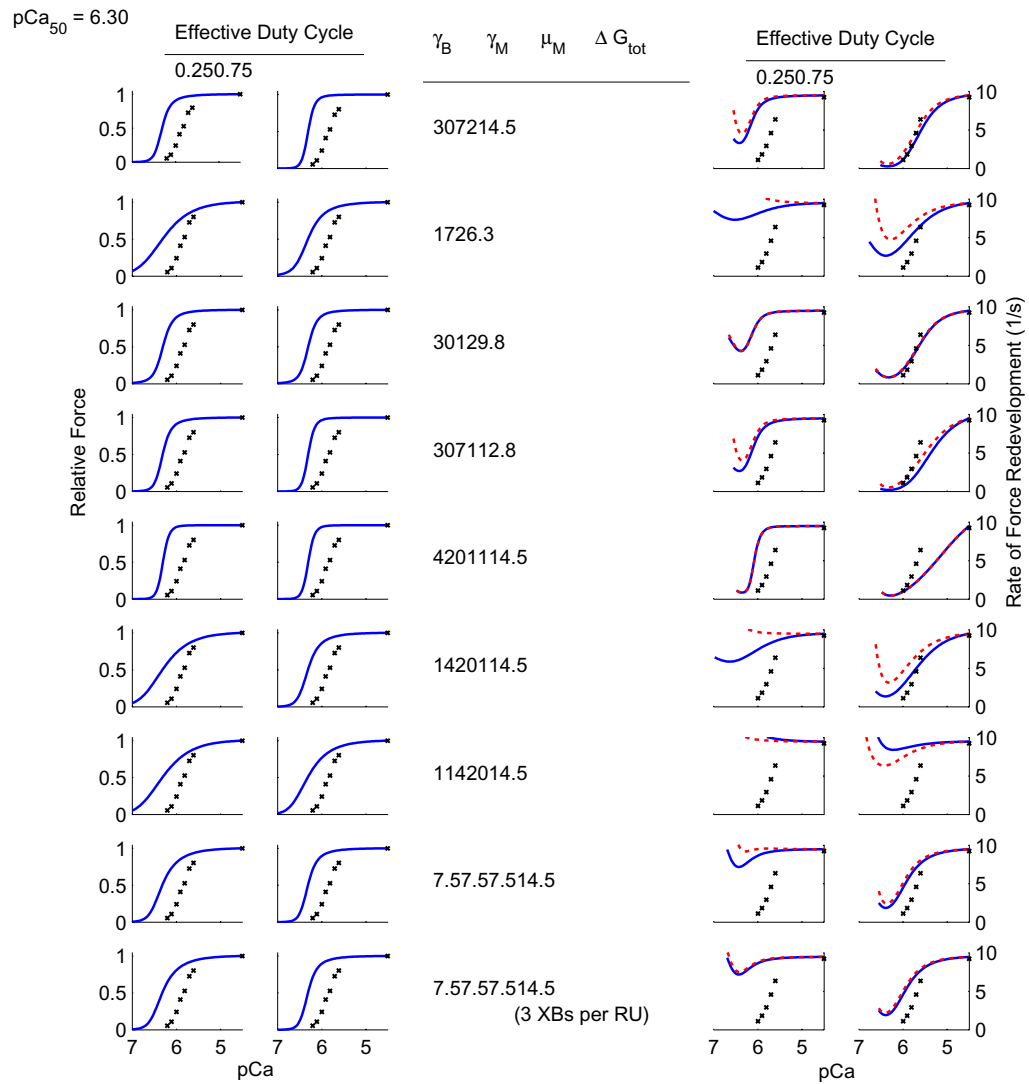


Figure C.6: Expanded sensitivity analysis, with same description as Figure C.5 except that here the equilibrium constant K_B^{ref} was adjusted in each case until half activation of force was pCa 6.3.

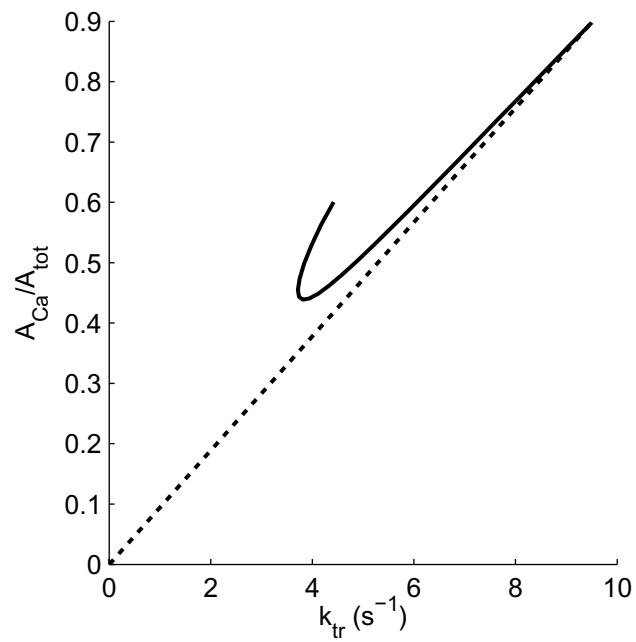


Figure C.7: The fraction of activation due to Ca^{2+} (A_{Ca}/A_{tot} , see §4.3.8 for description) as a function of k_{tr} . The relation approaches the line having slope $(A_{Ca}/A_{tot})^{max}/k_{tr}^{max}$ (dashed line). This suggests that k_{tr} is an indication of the relative contribution of crossbridges to activation, as well as crossbridge kinetics.

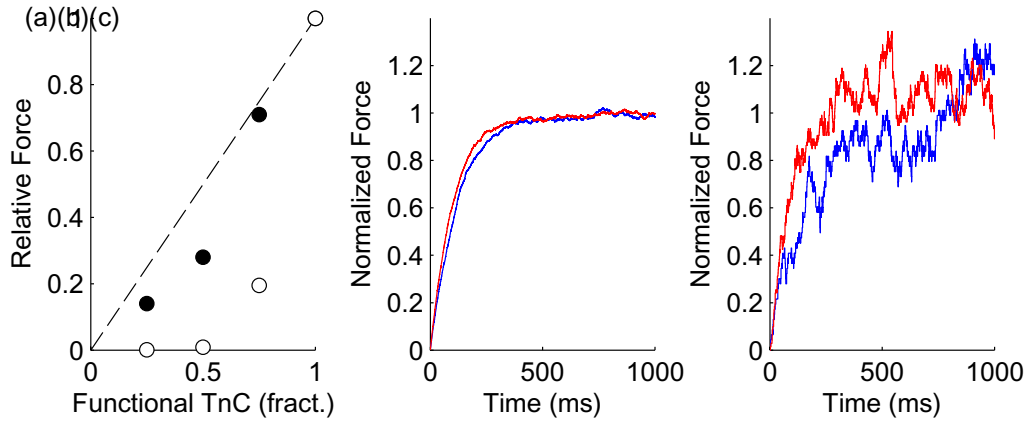


Figure C.8: Effects of non-functional TnC (xTnC) on maximally-activated steady-state force and the rate for force redevelopment (k_{tr}). (a) Maximally-activated force (pCa 4.0) of myofilaments at varying levels of functional TnC. Filled circles are mean values digitized from Gillis et al. (2007), open circles are from Monte Carlo simulations described in the text. The dashed line shows the 1:1 relation that would be expected if there were no interactions between nearest-neighbor RUs. (b) Time course plots of force redevelopment following breaking of crossbridges simulated using the Monte Carlo method, 0% xTnC. At pCa 4.0 (red trace) k_{tr} was 9.7 s^{-1} ; at pCa 5.3 (blue trace) k_{tr} was 0.82 s^{-1} . (c) Same as (b), but with 50% xTnC. Values of k_{tr} were 12.1 and 5.0 s^{-1} for pCa 4.0 and 5.3, respectively. The additional noise in these traces is a result of the low number of crossbridge binding events under these conditions.

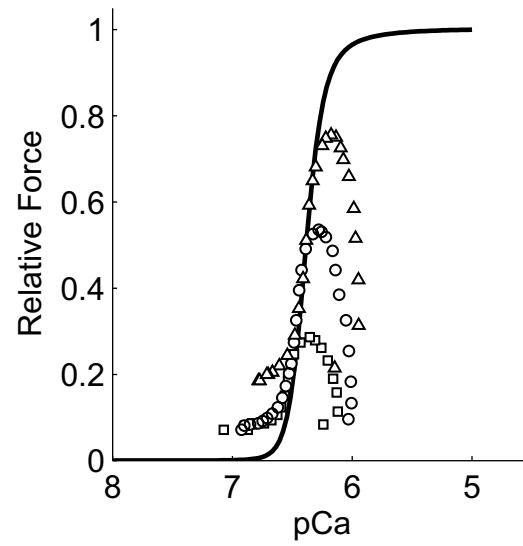


Figure C.9: The steady-state model response (solid line) fit to pharmacologically-slowed twitches, digitized from Dobrunz et al. (1995), Parameter Set 4

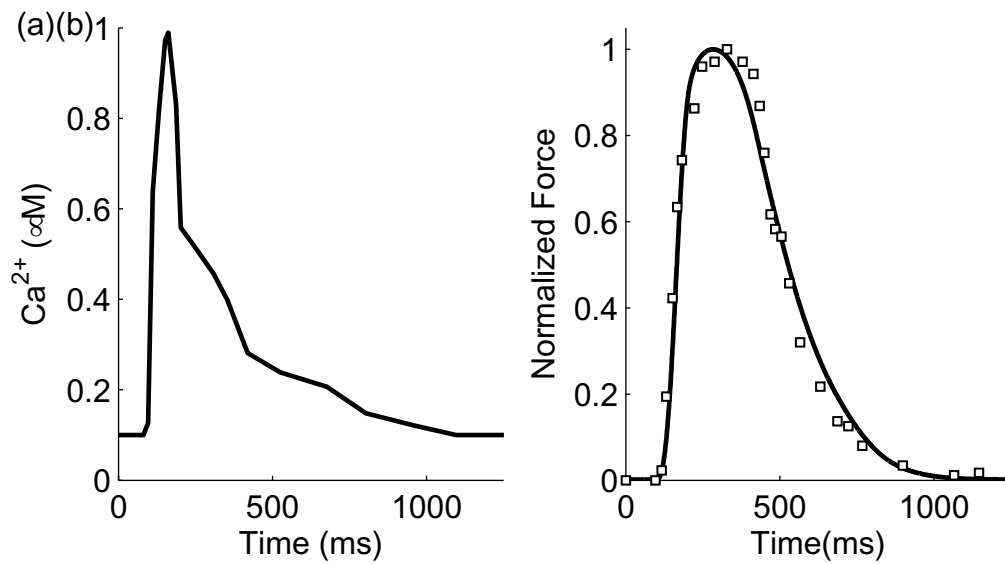


Figure C.10:]

Kinetic rates were scaled without altering equilibrium constants (Parameter Set 4) such that a measured Ca^{2+} transient (a) elicited a twitch force response from the model that agreed with measured twitch force in the same muscle (b). Data were digitized from Janssen & de Tombe (1997)

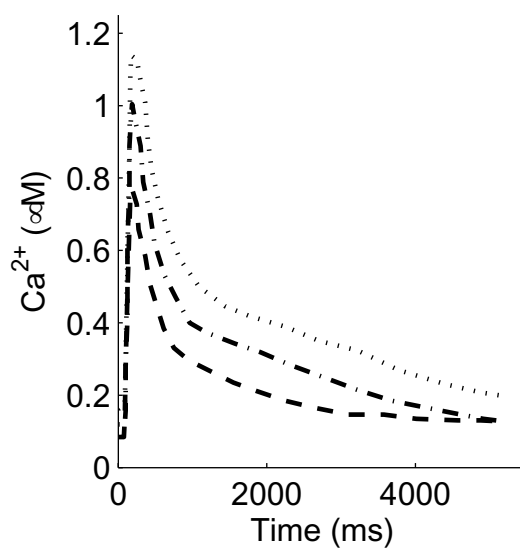


Figure C.11: Ca^{2+} transients used to drive twitch force time courses shown in Figure 4.8a, digitized from Dobrunz et al. (1995).

Table C.1: Results of thin filament state generation using periodic or ring boundary conditions. N refers to the number of regulatory units in each ring.

N	Naïve states (3^N)	Unique states	Unique transitions
3	27	10	12
4	81	21	36
5	243	39	90
6	729	92	270
7	2187	198	756
8	6561	498	2268
9	19683	1219	6636
10	59049	3210	19926
11	177147	8418	59292

Table C.2: Summary of twitch response properties under varying extracellular calcium concentration ($[Ca^{2+}]_o$). TTP, time to peak twitch force (ms); TPD₅₀, time from peak twitch force to 50% decay (ms), experimental values obtained from digitizing records in Dobrunz, et al. 1995.

3.0 μM $[Ca^{2+}]_o$		4.5 μM $[Ca^{2+}]_o$		6.0 μM $[Ca^{2+}]_o$	
TTP	TPD ₅₀	TTP	TPD ₅₀	TTP	TPD ₅₀
525.2	503.4	637.4	1040.7	650.0	1383.9
402	482	387	917	375	1859

Table C.3: Summary of effects of tropomyosin-tropomyosin (Tm-Tm) coupling and XB binding on twitch activation time course. A_{tot} , fraction of active regulatory units; TTP, time to peak A_{tot} ; TPD₅₀, time from peak to 50% decay of A_{tot} .

Condition	Diastolic A_{tot}	Peak A_{tot}	TTP (ms)	TPD ₅₀ (ms)
Control (Param. Set 2)	0.0	0.8	162	156.9
No Tm-Tm Coupling	0.1	0.5	98	130.5
No crossbridges	0.0	0.4	108	63.6

Table C.4: Sensitivity Analysis - Hill Coefficient of steady-state force (n_H), $r = 1.0$

pCa_{50}	5.85	6.30	5.85	6.30
δ_{eff}	0.25	0.25	0.75	0.75
$\gamma_B > \gamma_M > \mu_M$	3.07	4.11	3.85	5.61
γ_B removed	1.44	1.41	2.21	2.34
γ_M removed	2.58	3.54	2.85	3.95
μ_M removed	3.08	4.16	3.88	5.70
γ_B only	4.01	5.99	4.01	5.99
γ_M only	1.57	1.51	2.76	3.13
μ_M only	1.52	1.44	1.99	1.89
$\gamma_B = \gamma_M = \mu_M$	2.17	2.44	3.07	3.89
$\gamma_B = \gamma_M = \mu_M$, 3 XBs	2.17	2.44	3.07	3.89

Table C.5: Sensitivity Analysis - Hill Coefficient of steady-state force less than half maximal (n_1), $r = 1.0$

pCa_{50}	5.85	6.30	5.85	6.30
δ_{eff}	0.25	0.25	0.75	0.75
$\gamma_B > \gamma_M > \mu_M$	3.64	4.86	4.46	6.14
γ_B removed	1.59	1.61	2.48	2.72
γ_M removed	2.76	3.62	3.07	4.04
μ_M removed	3.61	4.83	4.46	6.14
γ_B only	4.53	6.28	4.53	6.28
γ_M only	1.80	1.80	3.28	3.79
μ_M only	1.76	1.73	2.39	2.37
$\gamma_B = \gamma_M = \mu_M$	2.65	3.16	3.71	4.76
$\gamma_B = \gamma_M = \mu_M$, 3 XBs	2.65	3.16	3.71	4.76

Table C.6: Sensitivity Analysis - Hill Coefficient of steady-state force greater than half maximal (n_2), $r = 1.0$

pCa_{50}	5.85	6.30	5.85	6.30
δ_{eff}	0.25	0.25	0.75	0.75
$\gamma_B > \gamma_M > \mu_M$	2.35	3.15	3.16	4.99
γ_B removed	1.24	1.22	1.79	1.86
γ_M removed	2.19	3.07	2.40	3.46
μ_M removed	2.39	3.27	3.22	5.15
γ_B only	3.41	5.62	3.41	5.62
γ_M only	1.30	1.27	2.11	2.35
μ_M only	1.24	1.20	1.53	1.47
$\gamma_B = \gamma_M = \mu_M$	1.61	1.73	2.33	2.91
$\gamma_B = \gamma_M = \mu_M$, 3 XBs	1.61	1.73	2.33	2.91

Table C.7: Sensitivity Analysis - Change in lower vs. upper Hill Coefficient of steady-state force (Δn_{1-2}), $r = 1.0$

pCa_{50}	5.85	6.30	5.85	6.30
δ_{eff}	0.25	0.25	0.75	0.75
$\gamma_B > \gamma_M > \mu_M$	1.30	1.71	1.29	1.15
γ_B removed	0.35	0.39	0.69	0.85
γ_M removed	0.57	0.55	0.67	0.58
μ_M removed	1.22	1.55	1.24	0.99
γ_B only	1.13	0.65	1.13	0.65
γ_M only	0.50	0.53	1.17	1.44
μ_M only	0.52	0.53	0.86	0.90
$\gamma_B = \gamma_M = \mu_M$	1.03	1.43	1.39	1.85
$\gamma_B = \gamma_M = \mu_M$, 3 XBs	1.03	1.43	1.39	1.85

Table C.8: Sensitivity Analysis - Minimum k_{tr} (s^{-1}), $r = 1.0$

pCa_{50}	5.85	6.30	5.85	6.30
δ_{eff}	0.25	0.25	0.75	0.75
$\gamma_B > \gamma_M > \mu_M$	3.72	3.30	1.29	0.27
γ_B removed	8.62	7.34	4.85	2.66
γ_M removed	4.71	4.26	3.03	0.83
μ_M removed	3.05	2.65	1.69	0.20
γ_B only	1.14	0.85	2.71	0.46
γ_M only	7.40	5.88	3.08	1.36
μ_M only	9.50	9.50	8.76	8.43
$\gamma_B = \gamma_M = \mu_M$	7.75	7.19	2.75	1.86
$\gamma_B = \gamma_M = \mu_M$, 3 XBs	7.77	7.21	2.80	1.92

Table C.9: Sensitivity Analysis - pCa of minimum k_{tr} , $r = 1.0$

pCa_{50}	5.85	6.30	5.85	6.30
δ_{eff}	0.25	0.25	0.75	0.75
$\gamma_B > \gamma_M > \mu_M$	6.02	6.41	5.91	6.34
γ_B removed	5.84	6.52	5.88	6.37
γ_M removed	5.98	6.37	5.88	6.34
μ_M removed	6.02	6.41	5.88	6.34
γ_B only	5.95	6.34	5.84	6.30
γ_M only	6.06	6.62	5.95	6.41
μ_M only	4.50	4.50	5.67	6.23
$\gamma_B = \gamma_M = \mu_M$	5.95	6.44	5.95	6.37
$\gamma_B = \gamma_M = \mu_M$, 3 XBs	5.95	6.44	5.95	6.41

Table C.10: Sensitivity Analysis - pCa of mid-range k_{tr} , $r = 1.0$

pCa_{50}	5.85	6.30	5.85	6.30
δ_{eff}	0.25	0.25	0.75	0.75
$\gamma_B > \gamma_M > \mu_M$	5.58	6.11	5.20	5.60
γ_B removed	5.30	5.87	5.32	5.69
γ_M removed	5.55	6.10	5.26	5.61
μ_M removed	5.54	6.08	5.21	5.39
γ_B only	5.46	6.08	5.28	5.25
γ_M only	5.44	5.92	5.33	5.64
μ_M only	n/a	n/a	5.20	5.72
$\gamma_B = \gamma_M = \mu_M$	5.55	6.10	5.38	5.88
$\gamma_B = \gamma_M = \mu_M$, 3 XBs	5.55	6.10	5.39	5.89

Table C.11: Sensitivity Analysis - Difference in pCa_{50} of steady-state force and k_{tr} , $r = 1.0$

pCa_{50}	5.85	6.30	5.85	6.30
δ_{eff}	0.25	0.25	0.75	0.75
$\gamma_B > \gamma_M > \mu_M$	0.27	0.20	0.65	0.71
γ_B removed	0.56	0.44	0.54	0.62
γ_M removed	0.31	0.20	0.60	0.69
μ_M removed	0.32	0.23	0.64	0.92
γ_B only	0.39	0.23	0.56	1.06
γ_M only	0.43	0.39	0.52	0.66
μ_M only	n/a	n/a	0.66	0.59
$\gamma_B = \gamma_M = \mu_M$	0.31	0.21	0.47	0.43
$\gamma_B = \gamma_M = \mu_M$, 3 XBs	0.31	0.21	0.47	0.42

Table C.12: Sensitivity Analysis - pCa of half-maximal steady-state force, $r = 1.0$

pCa_{50}	5.85	6.30	5.85	6.30
δ_{eff}	0.25	0.25	0.75	0.75
$\gamma_B > \gamma_M > \mu_M$	5.85	6.31	5.85	6.31
γ_B removed	5.87	6.31	5.86	6.31
γ_M removed	5.85	6.30	5.85	6.30
μ_M removed	5.85	6.31	5.85	6.31
γ_B only	5.85	6.30	5.85	6.30
γ_M only	5.87	6.32	5.86	6.31
μ_M only	5.87	6.32	5.86	6.31
$\gamma_B = \gamma_M = \mu_M$	5.86	6.31	5.85	6.31
$\gamma_B = \gamma_M = \mu_M, 3$ XBs	5.86	6.31	5.85	6.31

Table C.13: Sensitivity Analysis - Maximum k_{tr} (s^{-1}), $r = 1.0$

pCa_{50}	5.85	6.30	5.85	6.30
δ_{eff}	0.25	0.25	0.75	0.75
$\gamma_B > \gamma_M > \mu_M$	9.50	9.50	9.50	9.50
γ_B removed	9.50	9.50	9.50	9.50
γ_M removed	9.50	9.50	9.50	9.50
μ_M removed	9.50	9.50	9.50	9.50
γ_B only	9.50	9.50	9.50	9.50
γ_M only	9.50	9.50	9.50	9.50
μ_M only	9.50	9.50	9.50	9.50
$\gamma_B = \gamma_M = \mu_M$	9.50	9.50	9.50	9.50
$\gamma_B = \gamma_M = \mu_M$, 3 XBs	9.50	9.50	9.50	9.50

Table C.14: Sensitivity Analysis - Fitted values of K_B , $r = 1.0$.

pCa_{50}	5.85	6.30	5.85	6.30
δ_{eff}	0.25	0.25	0.75	0.75
$\gamma_B > \gamma_M > \mu_M$	45.87	88.88	19.46	38.02
γ_B removed	1.61	5.39	0.45	1.43
γ_M removed	43.31	83.79	17.22	36.67
μ_M removed	43.20	83.83	13.57	26.59
γ_B only	593.89	1114.19	193.09	370.06
γ_M only	1.57	5.05	0.38	0.99
μ_M only	7.37	22.94	3.31	11.36
$\gamma_B = \gamma_M = \mu_M$	14.51	30.85	7.99	16.85
$\gamma_B = \gamma_M = \mu_M$, 3 XBs	14.51	30.84	7.99	16.85

Table C.15: Sensitivity Analysis - Fitted values of the crossbridge duty cycle (δ), $r = 1.0$.

pCa_{50}	5.85	6.30	5.85	6.30
δ_{eff}	0.25	0.25	0.75	0.75
$\gamma_B > \gamma_M > \mu_M$	0.20	0.19	0.54	0.53
γ_B removed	0.31	0.23	0.69	0.59
γ_M removed	0.20	0.19	0.57	0.54
μ_M removed	0.27	0.26	0.76	0.75
γ_B only	0.25	0.25	0.76	0.75
γ_M only	0.43	0.31	0.83	0.78
μ_M only	0.00	0.00	0.00	0.00
$\gamma_B = \gamma_M = \mu_M$	0.09	0.08	0.19	0.18
$\gamma_B = \gamma_M = \mu_M, 3$ XBs	0.02	0.01	0.02	0.02

Table C.16: Sensitivity Analysis - Fitted values of g (s^{-1}), $r = 1.0$.

pCa_{50}	5.85	6.30	5.85	6.30
δ_{eff}	0.25	0.25	0.75	0.75
$\gamma_B > \gamma_M > \mu_M$	0.01	0.01	0.03	0.01
γ_B removed	0.02	0.01	0.03	0.01
γ_M removed	0.01	0.01	0.03	0.01
μ_M removed	0.01	0.01	0.05	0.01
γ_B only	0.01	0.01	0.43	0.03
γ_M only	0.01	0.01	0.03	0.01
μ_M only	0.87	0.87	0.99	0.97
$\gamma_B = \gamma_M = \mu_M$	0.03	0.02	0.04	0.02
$\gamma_B = \gamma_M = \mu_M, 3$ XBs	0.07	0.06	0.15	0.09

Table C.17: Sensitivity Analysis - Minimum k_{tr} (s^{-1}), $r = 0.0$

pCa_{50}	5.85	6.30	5.85	6.30
δ_{eff}	0.25	0.25	0.75	0.75
$\gamma_B > \gamma_M > \mu_M$	5.18	4.53	1.74	0.59
γ_B removed	9.50	9.50	6.24	4.76
γ_M removed	4.74	4.26	2.91	0.85
μ_M removed	4.61	4.02	2.15	0.52
γ_B only	1.14	0.85	2.71	0.46
γ_M only	9.50	9.50	4.73	3.15
μ_M only	9.50	9.50	6.85	6.36
$\gamma_B = \gamma_M = \mu_M$	9.47	9.23	3.19	2.40
$\gamma_B = \gamma_M = \mu_M$, 3 XBs	8.18	7.52	3.02	2.21

Table C.18: Sensitivity Analysis - pCa of minimum k_{tr} , $r = 0.0$

pCa_{50}	5.85	6.30	5.85	6.30
δ_{eff}	0.25	0.25	0.75	0.75
$\gamma_B > \gamma_M > \mu_M$	5.91	6.37	5.91	6.34
γ_B removed	4.50	4.50	5.81	6.27
γ_M removed	5.95	6.37	5.88	6.34
μ_M removed	5.91	6.34	5.88	6.34
γ_B only	5.95	6.34	5.84	6.30
γ_M only	4.50	4.50	5.88	6.30
μ_M only	4.50	4.50	5.95	6.44
$\gamma_B = \gamma_M = \mu_M$	5.49	6.27	5.95	6.37
$\gamma_B = \gamma_M = \mu_M$, 3 XBs	5.95	6.41	5.98	6.41

Table C.19: Sensitivity Analysis - pCa of mid-range k_{tr} , $r = 0.0$

pCa_{50}	5.85	6.30	5.85	6.30
δ_{eff}	0.25	0.25	0.75	0.75
$\gamma_B > \gamma_M > \mu_M$	5.56	6.11	5.28	5.68
γ_B removed	n/a	n/a	5.29	5.73
γ_M removed	5.54	6.10	5.27	5.63
μ_M removed	5.53	6.09	5.28	5.50
γ_B only	5.46	6.08	5.28	5.25
γ_M only	n/a	n/a	5.35	5.75
μ_M only	n/a	n/a	5.39	5.85
$\gamma_B = \gamma_M = \mu_M$	5.22	6.14	5.41	5.91
$\gamma_B = \gamma_M = \mu_M$, 3 XBs	5.55	6.11	5.42	5.92

Table C.20: Sensitivity Analysis - Difference in pCa_{50} of steady-state force and k_{tr} , $r = 0.0$

pCa_{50}	5.85	6.30	5.85	6.30
δ_{eff}	0.25	0.25	0.75	0.75
$\gamma_B > \gamma_M > \mu_M$	0.29	0.20	0.57	0.63
γ_B removed	n/a	n/a	0.57	0.57
γ_M removed	0.31	0.21	0.59	0.68
μ_M removed	0.33	0.22	0.57	0.80
γ_B only	0.39	0.23	0.56	1.06
γ_M only	n/a	n/a	0.50	0.55
μ_M only	n/a	n/a	0.47	0.46
$\gamma_B = \gamma_M = \mu_M$	0.64	0.17	0.45	0.39
$\gamma_B = \gamma_M = \mu_M$, 3 XBs	0.32	0.20	0.43	0.39

Table C.21: Sensitivity Analysis - Maximum k_{tr} (s^{-1}), $r = 0.0$

pCa_{50}	5.85	6.30	5.85	6.30
δ_{eff}	0.25	0.25	0.75	0.75
$\gamma_B > \gamma_M > \mu_M$	9.50	9.50	9.50	9.50
γ_B removed	9.50	9.50	9.50	9.50
γ_M removed	9.50	9.50	9.50	9.50
μ_M removed	9.50	9.50	9.50	9.50
γ_B only	9.50	9.50	9.50	9.50
γ_M only	9.50	9.50	9.50	9.50
μ_M only	9.50	9.50	9.50	9.50
$\gamma_B = \gamma_M = \mu_M$	9.50	9.50	9.50	9.50
$\gamma_B = \gamma_M = \mu_M$, 3 XBs	9.50	9.50	9.50	9.50

Table C.22: Sensitivity Analysis - Fitted values of K_B , $r = 0.0$.

pCa_{50}	5.85	6.30	5.85	6.30
δ_{eff}	0.25	0.25	0.75	0.75
$\gamma_B > \gamma_M > \mu_M$	45.87	88.88	19.46	38.02
γ_B removed	1.61	5.39	0.45	1.43
γ_M removed	43.31	83.79	17.22	36.67
μ_M removed	43.20	83.83	13.57	26.59
γ_B only	593.89	1114.19	193.09	370.06
γ_M only	1.57	5.05	0.38	0.99
μ_M only	7.37	22.94	3.31	11.36
$\gamma_B = \gamma_M = \mu_M$	14.51	30.85	7.99	16.85
$\gamma_B = \gamma_M = \mu_M$, 3 XBs	14.51	30.84	7.99	16.85

Table C.23: Sensitivity Analysis - Fitted values of the crossbridge duty cycle (δ), $r = 0.0$.

pCa_{50}	5.85	6.30	5.85	6.30
δ_{eff}	0.25	0.25	0.75	0.75
$\gamma_B > \gamma_M > \mu_M$	0.20	0.19	0.54	0.53
γ_B removed	0.31	0.23	0.69	0.59
γ_M removed	0.20	0.19	0.57	0.54
μ_M removed	0.27	0.26	0.76	0.75
γ_B only	0.25	0.25	0.76	0.75
γ_M only	0.43	0.31	0.83	0.78
μ_M only	0.00	0.00	0.00	0.00
$\gamma_B = \gamma_M = \mu_M$	0.09	0.08	0.19	0.18
$\gamma_B = \gamma_M = \mu_M, 3$ XBs	0.02	0.01	0.02	0.02

Table C.24: Sensitivity Analysis - Fitted values of g (s^{-1}), $r = 0.0$.

pCa_{50}	5.85	6.30	5.85	6.30
δ_{eff}	0.25	0.25	0.75	0.75
$\gamma_B > \gamma_M > \mu_M$	0.01	0.01	0.03	0.01
γ_B removed	0.01	0.01	0.01	0.01
γ_M removed	0.01	0.01	0.03	0.01
μ_M removed	0.01	0.01	0.02	0.00
γ_B only	0.01	0.01	0.43	0.03
γ_M only	0.01	0.01	0.01	0.00
μ_M only	430.22	431.68	327.12	321.33
$\gamma_B = \gamma_M = \mu_M$	0.08	0.07	0.13	0.09
$\gamma_B = \gamma_M = \mu_M$, 3 XBs	0.80	0.68	1.38	0.89

References

- [1] Dobrunz, L.E., Backx, P.H., and Yue, D.T., 1995. Steady-state $[Ca^{2+}]_i$ -force relationship in intact twitching cardiac muscle: direct evidence for modulation by isoproterenol and EMD 53998. *Biophys J*, 69:189–201.
- [2] Campbell, K.S. and Holbrook, A.M., 2007. The rate of tension recovery in cardiac muscle correlates with the relative residual tension prevailing after restretch. *Am J Physiol Heart Circ Physiol*, 292:H2020–2.
- [3] Tregear, R.T., Reedy, M.C., Goldman, Y.E., Taylor, K.A., Winkler, H., Franzini-Armstrong, C., Sasaki, H., Lucaveche, C., and Reedy, M.K., 2004. Cross-bridge number, position, and angle in target zones of cryofixed isometrically active insect flight muscle. *Biophys J*, 86:3009–19.
- [4] Bell, M.G., Lankford, E.B., Gonye, G.E., Ellis-Davies, G.C.R., Martyn, D.A., Regnier, M., and Barsotti, R.J., 2006. Kinetics of cardiac thin-filament activation probed by fluorescence polarization of rhodamine-labeled troponin C in skinned guinea pig trabeculae. *Biophys J*, 90:531–43.
- [5] Sun, Y.B., Lou, F., and Irving, M., 2009. Calcium- and myosin-dependent changes in troponin structure during activation of heart muscle. *J Physiol (Lond)*, 587:155–63.
- [6] Fitzsimons, D.P., Patel, J.R., and Moss, R.L., 2001. Cross-bridge interaction kinetics in rat myocardium are accelerated by strong binding of myosin to the thin filament. *J Physiol (Lond)*, 530:263–72.
- [7] Gillis, T.E., Martyn, D.A., Rivera, A.J., and Regnier, M., 2007. Investigation of thin filament near-neighbour regulatory unit interactions during force development in skinned cardiac and skeletal muscle. *J Physiol (Lond)*, 580:561–76.

- [8] Dobesh, D.P., Konhilas, J.P., and de Tombe, P.P., 2002. Cooperative activation in cardiac muscle: impact of sarcomere length. *Am J Physiol Heart Circ Physiol*, 282:H1055–62.
- [9] Janssen, P.M. and Tombe, P.P.D., 1997. Uncontrolled sarcomere shortening increases intracellular Ca^{2+} transient in rat cardiac trabeculae. *Am J Physiol*, 272:H1892–7.